The effect of flux emergence from the solar surface to the corona

David Llewellyn Shelton

Mullard Space Science Laboratory
Department of Space and Climate Physics
University College London

A thesis submitted to University College London
for the degree of Master of Philosophy

September 1, 2014

I, David Llewellyn Shelton, confirm that the work done in this thesis is my own. Where information has been derived from other sources, I can confirm that I have indicated this in the thesis.

Contents

List of Figures

List of Tables

Abstract

The aim of this work is to investigate the role of flux emergence in creating the atmospheric phenomena we see. We will look at two emerging flux regions of different sizes and how the atmosphere responds to the different emerging flux regions. We also will look at the role played by the serpentine field creating responses in the atmosphere.

In this work, we will use multi-wavelength observations from the Michelson Doppler Imager (MDI), the Transition Region And Coronal Explorer (TRACE), the Solar Optical Telescope (SOT), the EUV Imaging Spectrometer (EIS), the Atmospheric Imaging Assembly (AIA) and the Helioseismic and Magnetic Imager (HMI) to investigate our objectives.

In chapter 1, we introduce the Sun, the role of magnetic flux emergence and how we can measure the different solar phenomena.

In chapter 2, we introduce the instruments we used in this work. These instruments use the techniques we described in chapter 1 to measure the phenomena we see in the Sun's atmosphere and on its surface.

In chapter 3, we compare two emerging flux regions, one large EFR lasting several days and a small EFR lasting less than a day. We found that in the large EFR, new loops form in the serpentine region 5 hours after the flux emergence begins. We also find outflow enhancements of approximately 50 km s^{-1}. These appear to be caused by reconnection on one side of the EFR and compression on the other side of the EFR. These start between 5 and 8 hours and 8 and 12 hours after the flux emergence begins. In the smaller EFR, we saw jets forming in the chromosphere and corona over the serpentine field and the large-scale EFR magnetic field. We also see brightenings forming in the upper photosphere, chromosphere and the corona after the flux emergence begins as a response to magnetic flux cancellation. We also find upflow enhancements of approximately 10 km s^{-1} on the north side of the EFR. Finally, we see new coronal loops forming up to 100″ from the EFR.

We see differences in how each emerging flux region affects the local solar atmosphere. This appears to be dependent on the average flux density of the emerging flux region. We also see coronal jets forming over the serpentine field for the first time.

Acknowledgements

There are too many thank yous to make, but I'll give it a go. I'd like to thank my family for their continuing support. My heartfelt thanks go to my friends both outside of MSSL and at MSSL. Your support, your kindness and the many discussions and laughs we have had together have been fantastic and I look forward to continuing it all. A special thanks has to go to the everyone in G01, both new and old. Deb, Ailsa, Ehsan, Jack, Peng-Fei, Dina, Jian and Steph, it's been great and I wouldn't have got to this point without you guys. You've kept me sane.....sort of.

To the rest of the solar group: the clan of Daves, Lidia, thanks for you support and advice. To Sarah and Len, thanks for the support, advice and giving me your opinions on my work.

Finally, my thanks go to my supervisors. Lucie, thanks for all the support you've given me and our science chats and outreach conversations have been fantastic. Louise, thanks for giving me the opportunity to work on such a great and important astrophysical object. Your guidance, support, advice and science conversations have been great. Thanks as well for involving me in the organisation for the conference for George and Tetsuya in 2012. It was a great experience and I got to meet people from the wider solar community. Thanks for being so patient with me, even when my questions have been stupid. It's been a great 3 and a half years and thanks to everyone who's been part of my life.

Chapter 1

Introduction

1.1 The Sun

The Sun is a G2V (yellow dwarf) star and is found on the main sequence area of the Hertsprung-Russell diagram. The Sun was born approximately 5 billion years ago and is half-way through its life (as shown by radiometric dating of meteorites). The Sun is mostly comprised of Hydrogen (70% by mass) and Helium (28% by mass) and converts Hydrogen into Helium via nuclear fusion. The mass of the Sun is approximately 2.0×10^{30} kg and makes up approximately 99.8% of the solar system's mass. The solar radius (from core to surface) is approximately 6.95×10^{8}m and the temperature of the Sun ranges from 5800 K at the surface to 15 million K in the core. The Sun's atmospheric temperature ranges from 4,100 K at the temperature minimum layer (approximately 500 km above the photosphere) to 20 million K in the corona. The Sun is kept in its spherical shape by the balance (called hydrostatic equilibrium) between gravity (trying to shrink it) and plasma pressure (that is trying to expand it).

The Sun has been studied by humans since the dawn of our civilisation and our ancestors worshipped it like a deity. To date, the Sun is the most studied star in the universe and is studied using various ground and space-based observatories.

1.2 The layers of the Sun

There are seven main layers of the Sun from the core to the corona as shown in fig. 1.1.

1.2.1 The core

The core lies at the centre of the Sun and extends to approximately $\frac{1}{4}$ of the Sun's radius (García et al. 2007) and has a density is approximately 1.50 $\times 10^{5}$ kg m^{-3} (Basu et al. 2009). For fusion to occur, protons must be close enough to overcome

the Coloumb force which then allows strong force to act and fuses the protons together. For the protons to overcome the Coloumb force, the temperature of the plasma must be high enough and the plasma dense enough (therefore the protons require high kinetic energies to overcome the Coloumb force). They must also use the quantum mechnical effect known as tunnelling to overcome the Coloumb force. The probability of quantum tunnelling occurring is very low, but the shear number of protons with high kinetic energies in the core allows tunnelling to take place. Hydrogen fuses together in the core via the proton-proton chain:

$$p + p \rightarrow^2 D + e^+ + \nu_e \tag{1.1}$$

where p is a proton, D is deuterium and ν_e is an electron neutrino. This is the first stage in producing Helium. The second stage fuses a third proton with deuterium to form Helium-3 and a gamma ray:

$$p +^2 D \rightarrow^3 He + \gamma \tag{1.2}$$

Finally, a stable helium nucleus is formed by fusing two helium-3 nuclei.

$$^3He +^3 He \rightarrow^4 He + p + p \tag{1.3}$$

This results in a stable helium nucleus and two protons to start the process again. During this process, energy is released via Einstein's relation between mass and energy (Bethe and Critchfield 1938) and the total energy release per reaction is approximately 4.3×10^{-12}J (with small amount of energy removed from the system via neutrinos).

1.2.2 The Radiative Zone

The radiative zone lies between 0.25 R_{sun} to 0.71 R_{sun} and has temperatures ranging between 7 million K to 2 million K (from base of radiative zone to the top). The density also drops from 2×10^4 kg m^{-3} to 2 $\times 10^2$ kg m^{-3}. To transport the energy created in the core to the outer parts of the Sun, an efficient method is required. In this case, the most efficient method is via radiation. So energy transport takes place by the transfer of photons between ions (radiative transfer). Photons take approximately 3,000 years (random walk travel time), to travel from the core to the solar surface because they are Thomson scattered by free electrons. As the temperature of the radiative zone decreases, atoms are able to hold on to their orbiting electrons and therefore, more radiation is absorbed and increases the opacity of the gas in the radiative zone.

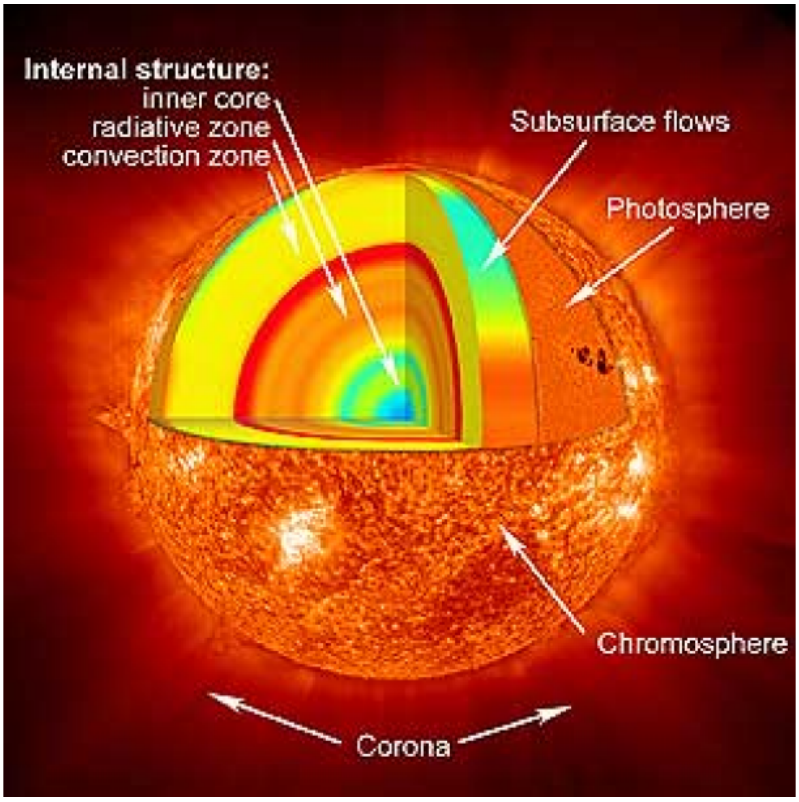

Figure 1.1: Image representing the different layers of the Sun. This image was created by http://www.nasa.gov/images/content/171926main_heliolayers_label_lg.jpg.

1.2.3 The Convection Zone

The convection zone is the Sun's outer-most internal layer and is approximately 200,000 km in height. The plasma in this layer is not dense or hot enough to transfer the thermal energy of the solar interior through radiation. This is because as the temperature decreases, the opacity increases and makes it more difficult for radiation to escape. This causes the heat to become trapped and the gas becomes unstable. It is this instability that causes convection. The base of the convection zone has a temperature somewhere between 1 and 2 million K, while at the top of the convection zone the temperature is approximately 6,000 K. At approximately 1 million K, the temperature gradient dominates over the adiabatic gradient (this is the rate at which temperature would decrease if a 'packet' of gas rises without exchanging heat with its local environment) and convection occurs. The cool gas then falls back to the base of the convection zone in a convective motion. These convective cells transfer gas and magnetic field around the convective zone. The average density of the convection zone is 2×10^2 kg m^{-3}, which is similar to the density found at the top of the radiative zone.

1.2.4 The Photosphere

The photosphere is the visible surface of the Sun because the opacity drops and photons are able to escape with a much larger mean free path (compared to the radiative zone). The photosphere only has a thickness of approximately 300 kilometres. As the upper part of the photosphere is cooler (4,500 K) than the lower photosphere (6,000 K), an image of the Sun is brighter in the center than at the limb and this is called limb darkening. The photosphere has a particle density of 10^{23} m^{-3}.

The photosphere is opaque to ultraviolet and infrared wavelengths. This is in part due to free electrons being able to combine with neutral hydogen to form H^- and the abundance of these negative hydrogen ions is sufficient to be the main source of the photosphere's high opacity.

The most prominent feature on the photosphere are sunspots. Sunspots are darker regions that have lower temperatures than the rest of the photosphere and have strong magnetic fields (up to 1500 G). Globally, the thermal pressure in the photosphere is much greater than the magnetic pressure. Sunspots cover less than 1% of the visible Sun. The rest of the surface is made up of granules that are of the order of 1 Mm in size, although there are smaller granules. They only last between 10 and 20 minutes and are separated by dark, cooler intergranular lanes. Evidence for convective motions can be seen as granulation where granules have upward velocities of approximately 2 km s^{-1}. Intergranular lanes have downward motions.

1.2.5 The Chromosphere

The lowest temperature of the Sun is at the top of the photosphere (4,000 K). Above the photosphere is the chromosphere which is on average, 2,500 km above the photosphere. The temperature starts to increases with height and at the top of the chromosphere the temperature is approximately 20,000 K. The chromosphere is observed in the optically thick Hα line (photoelectrically controlled) and Ca II H and K (collisionally controlled) (Harra and Mason 2004).

In the chromosphere, sunspots are surrounded by patches of bright emission called plages and are associated with magnetic field concentrations. Dense, cool plasma filaments that are suspended above the solar surface by the magnetic field are referred to as prominences when observed at the solar limb.

Another feature of the chromosphere are spicules and these are thin elongated, jet-like structures. There are two types of spicules:type I (fibrils) which last for 3 to 10 minutes and type II spicules (or chromospheric jets) that last for between 10 to 100 seconds (de Pontieu et al. 2007). Chromospheric jets have higher velocities than fibrils and may play a part in coronal heating (De Pontieu et al. 2009). We

will describe the chromosphere's response to emerging flux in section 1.4.2.

1.2.6 The Transition Region

The transition region is found between the chromosphere and the corona. It is the boundary layer between the big temperature increase from 20,000 K in the chromosphere to 2 million K in the corona and also a big change in plasma-β (see section 1.3.3.3).

There are also several other big transitions in this region:

1. Below the transition region, gravity, gas pressure and fluid dynamics dominate the shape of the Sun's features, while other dynamic forces and magnetic forces dominate above this layer.

2. Below the transition region, most of the helium is not ionized, while above the layer, the helium is fully ionized.

3. Material below the transition region is opaque to certain absorption spectral lines in the infrared, visible light and near ultraviolet. Above the transition region are emission lines in the extreme ultraviolet and X-ray wavelengths.

The thickness of the transition region varies across the solar atmosphere and in some places may be vertical (Golub and Pasachoff 1997). The transition region is primarily observed in ultraviolet wavelengths and the emission is dominated by Mg II, C IV, OIV and V and SI IV ions. Hydrogen is ionized at the high temperatures found in the transition region.

1.2.7 The Corona

The corona sits as the top layer of the Sun and is the hottest layer of the solar atmosphere. The corona extends to more than one solar radius above the photosphere and has an average density of 1 $\times 10^{-12}$ kg m^{-3}. The temperature exceeds 1 million K and the corona is observed in extreme ultraviolet, X-ray wavelengths and four white-light components: K(kontinuerlich), F (Fraunhofer), E (Emission) and T (thermal).

The K-corona is caused by scattered light (from Thomson scattering) from the photosphere by free electrons of the plasma in the corona. Classic coronal structures such as streamers and Coronal Mass Ejections (CMEs) are found in the K corona. The F-corona (also known as the dust corona), includes the dark absorption lines of the photospheric Fraunhofer spectrum and is created from sunlight scattering off dust. Fraunhofer lines are not present in the K-corona due to the high coronal temperatures. This dust emits thermal emission in the infrared and this causes the T-corona. The E-corona is formed from highly ionised atoms with isolated spectral lines.

One of the big science questions associated with the corona is why is it so hot?

There is general agreement that the energy required to heat the corona is generated by turbulence in the convective zone (Golub and Pasachoff 1997; Klimchuk 2006; Schrijver and Siscoe 2009). This turbulence can cause the footpoints of magnetic fieldlines to be buffeted which can cause field stresses or wave generation and depends on the turbulence time scales relative to the Alfvèn travel times. (Klimchuk 2006).

Heating mechanisms can be divided into two main highly debated categories: direct current (heating is via current sheets, reconnection dissipation and magnetic field stresses) or alternating current (heating is via waves and dissipation is by shock dissipation, damping, resonance heating and magnetohydrodynamic (MHD) turbulence) (Golub and Pasachoff 1997; Klimchuk 2006; Schrijver and Siscoe 2009;Mandrini et al. 2000). Direct current velocity field timescales are longer than the Alfvén transit time while the alternating current velocity field timescales are shorter. We will describe the corona's response to emerging flux in section 1.4.3.

1.3 Solar Magnetism

The Sun's magnetic field drives the activity we see. In this section, we will describe the formation of the magnetic field, the 11 year (on average) magnetic cycle, how we measure the Sun's magnetic field, and finally the emergence of magnetic flux through the convection zone to the photosphere.

1.3.1 The role of the Solar Dynamo

When a plasma is forced to move through a magnetic field, the electrons in the plasma experience a force and generate an electric current. As the current flows through the plasma, an additional magnetic field is generated. This process describes a simple dynamo. The amplification of the global magnetic field is thought to be located between the radiative and convection zones in a region called the tachocline. Since the solar equator rotates faster than the poles (differential rotation), some of the kinetic energy in the Sun is transformed into magnetic energy. This dynamo process can maintain a magnetic field against ohmic dissipation.

1.3.2 The Solar Magnetic Cycle

The solar cycle is on average an 11 year cycle between solar maximum and the next solar maximum. However, the duration has been observed to vary between 8 and 15 years. There are three laws that relate orientation and emergence patterns of sunspot groups during the solar cycle: Hale's law (Hale and Nicholson 1925) that states that bipolar active regions that are aligned roughly in the east-west direction on opposite hemispheres have opposite leading magnetic polarities; the

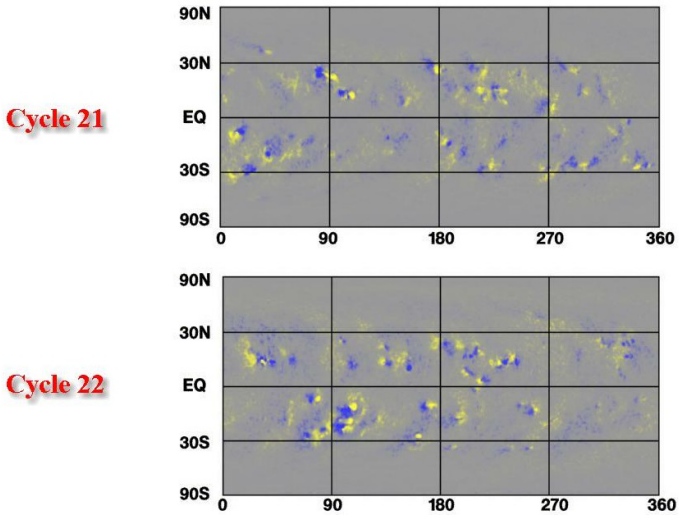

Figure 1.2: Graphical representation of Hale's law which shows the change in polarity of same hemisphere bipoles between cycles. http://solarscience.msfc.nasa.gov/images/haleslaw.jpg. The active region polarities are represented by blue and yellow. Yellow represents positive polarity and blue represents negative polarity.

butterfly diagram (Carrington 1860) states that the latitudes of flux emergence show a dependence on the solar cycle and finally, Joy's law (Hale et al. 1919) recognises that there is a systematic deviation from the east-west alignment of bipolar active regions with the leading spot being closer to the equator on both solar hemispheres. The trailing spot in an active region is more fragmented than the leading spot. This is due to an eastward tilt in emerging flux tubes (Hale et al. 1919). The tilt is due to the Coriolis force (Fisher et al. 1995) and also large-scale vortices in the convective zone deforming the rising flux tube (López Fuentes et al. 2003). Figures 1.2, 1.3 and 1.4 show the three laws.

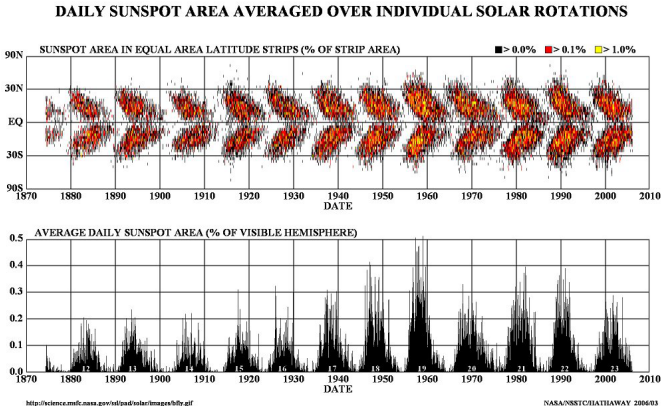

Figure 1.3: Graphical representation of the butterfly diagram (spörer's law) which describes the change in polarity of the poles caused by the drift of the fragmented trailing edge of active regions and the average sunspot area over 12 cycles. http://www.spacedaily.com/images-lg/solar-science-sunspot-shutdown-2011-lg.jpg.

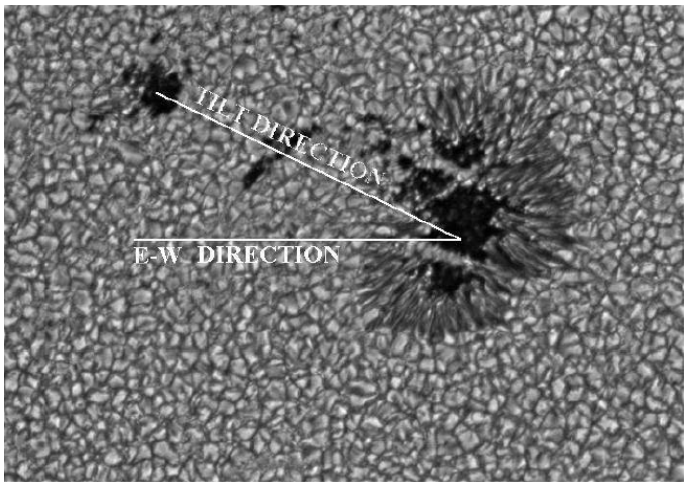

Figure 1.4: Graphical representation of Joy's law which shows how the leading edge of an active region is closer to the equator than the trailing edge, the trailing edge is more fragmented than the leading edge and that there is a clear tilt between the leading spot and the trailing spot http://bison.ph.bham.ac.uk/~wjc/Teaching/joys_law.jpg.

1.3.3 Measuring the Sun's magnetic field

The Gauss is the unit of magnetic flux density. One Maxwell (Mx) is defined as one Gauss across a surface of one square centimetre (and is the unit for magnetic flux) that is perpendicular to the magnetic field and is expressed as:

$$F_M = \int_s \underline{\mathrm{B}}.d\underline{\mathrm{S}} \tag{1.4}$$

where F_M is the magnetic flux in Maxwells and dS is a vector normal to the surface S.

1.3.3.1 Photospheric magnetic field measurements

The magnetic field in the photosphere can be measured by the Zeeman splitting of certain photospheric Fraunhofer lines (as shown in figure 1.5). Zeeman splitting occurs when the small magnetic fields generated by electrons orbiting atoms or ions interact with an external magnetic field. The electron's orbital angular momentum couples to the external magnetic field. This then produces an energy shift in the atomic states and this shift in energy is proportional to the strength of the external magnetic field. The resulting components of the spectral line have a wavelength displacement (two σ components) that are either side of the unshifted spectral line (π component). The wavelength displacement of the spectral lines is given by:

$$\triangle\lambda = \frac{\pi e \lambda^2 g B}{M_e c} = 4.7 \times 10^{-13} \lambda^2 g B \tag{1.5}$$

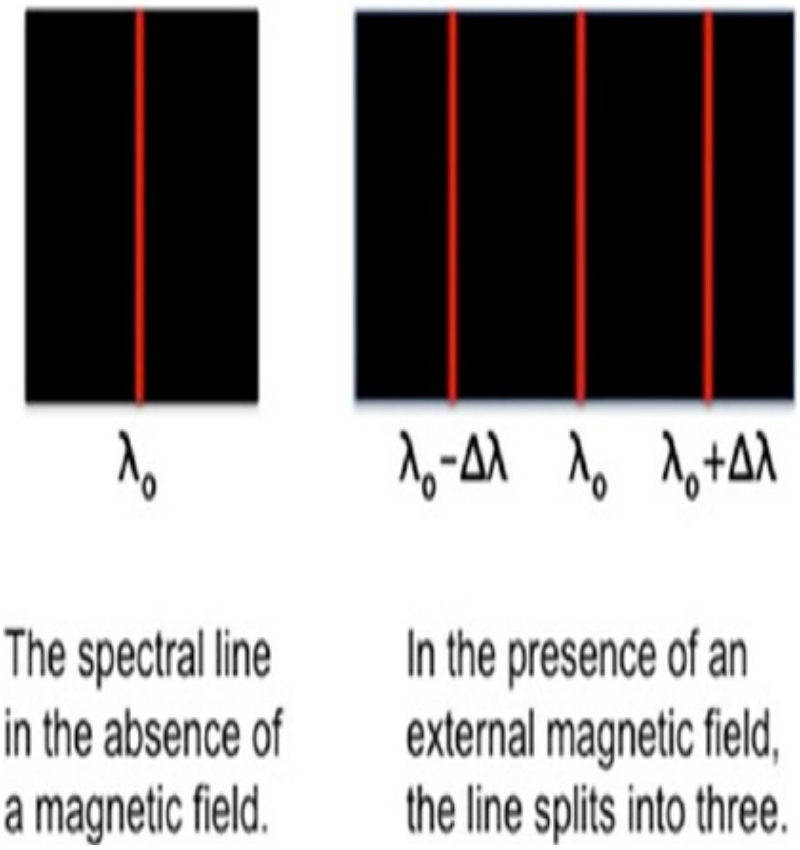

Figure 1.5: shows how Zeeman splitting occurs in a magnetic field. Image courtesy of http://astronomy.swin.edu.au/cms/cpg15x/albums/scaled_cache/zeeman-pic-640x480.jpg.

where e is the charge on an electron, M_e is the electron mass, c is the speed of light in a vacuum, λ is the wavelength in Å, B is the magnetic field strength in Gauss and g is the Landé factor which is given by:

$$g = 1 + \frac{J(J+1) + S(S+1) - L(L+1)}{2J(J+1)} \tag{1.6}$$

where J is the total angular momentum, S is the total spin momentum and L is the total orbital angular momentum. For the Zeeman splitting to be detected, either the magnetic field strength or the Landé factor needs to be large.

A line-of-sight magnetogram detects the wavelength displacements (which are circularly polarised) and are represented by white (where magnetic field lines are pointing towards the observer) and black (where magnetic field lines are pointing away from the observer) patches. Vector magnetograms detect the original spectral line plus the wavelength displacements (which are linearly polarised). The white patches (called positive polarities) are where magnetic field lines are pointed towards the line of sight and the black patches (called negative polarities) are where the magnetic field lines are pointed away from the line of sight. The area between polarities is called the 'magnetic inversion line'. From Joy's law (figure 1.4) we know that leading polarities are angled closer to the equator and in the case of the last cycle, the negative polarity was the leading polarity in the northern hemisphere.

These polarities have the strongest magnetic fields.

1.3.3.2 Coronal magnetic field measurements

Due to the high temperatures in the corona, thermal broadening obscures the Zeeman splitting and makes measuring the coronal magnetic field very hard. Information of coronal magnetic field can be found by measuring the emission of electrons spiralling along the magnetic field lines at radio frequencies (gyrosynchrotron emission), however the long wavelength means a poor spatial resolution. Another method was introduced by Tomczyk et al. (2008) by using the λ^2 displacement to map out the coronal magnetic field at the limb using infrared forbidden emission lines. One assumption is that the field is force-free and this assumption is for plasma-$\beta \ll 1$ (see eq. 1.3.3.3) and this is the case for the corona.

We can understand the morphology of the field by finding an expression for the magnetostatic form of the momentum equation:

$$0 = -\nabla \underline{P} + \underline{j} \times \underline{B} + \rho g \tag{1.7}$$

where $\nabla \underline{P}$ is the pressure gradient, the second term is the Lorentz force and the third term is due to gravity. Using Ampére's law and substituting in the magnetic pressure equation we get:

$$\underline{j} \times \underline{B} = -\nabla \frac{B^2}{2\mu_0} + \frac{(\underline{B}\nabla)\underline{B}}{\mu_0} = 0 \tag{1.8}$$

where $\underline{j} \times \underline{B}$ is the Lorentz force per unit volume, $\nabla \frac{B^2}{2\mu_0}$ is the magnetic pressure gradient and $\frac{(\underline{B}\nabla)\underline{B}}{\mu_0}$ is the magnetic tension force.

This leads to:

$$\underline{j} \times \underline{B} = \frac{1}{\mu_0}(\nabla \times \underline{B}) \times \underline{B} = 0 \tag{1.9}$$

When the field is force-free the current density j is parallel to B. By taking the divergence of the force-free equation where α is defined as a scalar function of position, we find an expression that shows that α is constant along a field line:

$$\underline{B} \cdot \nabla \alpha = 0 \tag{1.10}$$

The α term also describes the amount of twist in the magnetic field.

1.3.3.3 Plasma-β

Plasma-β describes the ratio between the gas pressure of a plasma and the magnetic pressure (see equation 1.11). When $\beta \gg 1$, the gas pressure dominates over the magnetic pressure and this is found in the photosphere, outer corona and the solar

interior. However in the corona, $\beta \ll 1$ which means that the plasma pressure influence is virtually negliable and the magnetic field is essentially force free. The equation for β is given as:

$$\beta \equiv \frac{p_g}{p_m} \equiv \frac{nk_BT}{\frac{B^2}{2\mu_0}} \tag{1.11}$$

where p_g is the gas pressure, p_m is the magnetic pressure, n is the particle number density, k_B is the Boltzmann constant, T is the temperature of the plasma, B is the magnetic field strength and μ_0 is the magnetic permeability in a vacuum.

1.3.4 Magnetic Reconnection

Magnetic reconnection is the process in which magnetic field lines change connectivity. The magnetic field of the corona is under stress constantly from photospheric and chromospheric dynamics (such as flux emergence, differential rotation and convective motions). These connectivity changes result in transformation of energy from free magnetic energy to kinetic energy. Reconnection is thought to be one of the drivers of coronal heating. The observational evidence for reconnection in the Sun includes outflows, jets and brightenings.

1.3.4.1 The "frozen-in" theorem

The frozen-in theorem states that in a perfectly conducting plasma, the magnetic field lines are "frozen-in" to the plasma (Alfvén 1943). This means that there are no changes to the field by motions along the field lines, but that transverse motions can carry the field with them. To understand how the "frozen-in" theorem works, let us consider the induction equation and the magnetic Reynolds number:

$$\frac{\partial \underline{B}}{\partial t} = \nabla \times (\underline{v} \times \underline{B}) + \eta + \nabla^2 \underline{B} \tag{1.12}$$

$$R_m = \frac{Lv}{\eta} \tag{1.13}$$

where η is the Ohmic magnetic diffusivity $\frac{1}{\mu_0 \sigma}$, B is the magnetic field strength, L is the characteristic length and v is the characteristic velocity. The magnetic Reynolds number is the ratio between the advective motions of the magnetic field and plasma (first term on the right hand side of the induction equation) and the diffusion of the magnetic field through the plasma (second term on the right of the induction equation).

So when $R_m \gg 1$, the advective motions dominate over diffusion and as R_m approaches infinity, the field lines are "frozen in" to the plasma.

By combining the induction equation with Gauss's law and divergence theorem, we can find an expression that shows that the field lines are frozen into the plasma:

$$\frac{d\Phi}{dt} = \frac{d}{dt}\int_c \underline{\mathrm{B}} \cdot d\underline{\mathrm{S}} = 0 \tag{1.14}$$

where Φ is the magnetic flux and $\underline{\mathrm{S}}$ is the closed surface.

1.3.4.2 2D reconnection

To understand 2D reconnection, we need the Lorentz force (eq. 1.15) and Ohm's law (eq. 1.16):

$$F = q(\underline{\mathrm{E}} + (\underline{\mathrm{v}} \times \underline{\mathrm{B}})) \tag{1.15}$$

where q is the electric charge, E is the electric field strength, v is the particle velocity and B is the magnetic field strength,

$$\mathrm{j} = \sigma(\underline{\mathrm{E}} + \underline{\mathrm{v}} \times \underline{\mathrm{B}}) \tag{1.16}$$

where j is the current density,

$$\frac{B_1^2}{2\mu_0} + p_1 = p_{x-point} = \frac{B_2^2}{2\mu_0} + p_2 \tag{1.17}$$

where μ_0 is the magnetic permeability in a vacuum, p_1 is the thermal pressure one side of the x-point, $\mathrm{p}_{x-point}$ is the pressure at the x-point and p_2 is the thermal pressure on the other side of the x-point.

$$E_0 = \frac{v_1}{c}\underline{\mathrm{B}}_1 = \frac{v_1}{c}\underline{\mathrm{B}}_2 = \frac{j_{nl}}{\sigma} \tag{1.18}$$

For magnetic reconnection to occur, the magnetic Reynolds number (eq. 1.13) must be $\ll 1$ and means that electric currents are dissipated. So either the ohmic magnetic diffusivity term in the induction equation (eq. 1.12) η increases or the characteristic length L decreases. This also means that the diffusion component of the induction equation dominates over the advection component and the magnetic field lines are no longer "frozen-in" to the plasma and reconnection can occur.

In 2D reconnection (fig. 1.6), a magnetic null point is required. This is where the magnetic field strength is zero and plasma-$\beta(eq.1.11) \gg 1$. The force balance across the X-point is described by equation 1.17. A diffusion region is created for which the plasma is able to accelerate across at the Alfvén speed (when field lines are oppositely directed). The Lorentz force (eq. 1.15) then creates an electric field in the diffusion region for which a current sheet is associated with the diffusion region (eq. 1.18). Two oppositely directed fieldlines are then able to reconnect (see figure 1.6) and post-reconnection, one loop will be pulled downwards by magnetic tension (as its radius of curvature is less than the radius of curvature required to overcome magnetic tension) and the other loop (which has a higher radius of curvature) is pulled higher into the atmosphere.

Reconnection events can be slow (Sweet-Parker) or fast (Petschek). These two models will be described in the next sections.

Before understanding the Sweet-Parker model (Sweet 1958; Parker 1957;Parker 1963) and the Petschek model (Petschek 1964), we need an expression for the ratio between the Alfvén wave crossing timescale and the resistive diffusion timescale (called the Lundquist Number):

$$S = \frac{v_A l}{\eta} = \mu_0 \sigma v_A l \tag{1.19}$$

where v_A is the Alfvén speed and l is a typical length scale.

$$v_A \equiv \frac{B}{(\mu_0 \rho)^{\frac{1}{2}}} \tag{1.20}$$

High numbers indicate high conducting plasmas and the corona has typical values between 10^8 and 10^{12}.

1.3.4.3 Sweet-Parker reconnection

The Sweet-Parker model describes 2D reconnection that occurs when the length of the diffusion region is much greater than the width. Here the outflow speed v_2 is approximately the Alfvén speed and is related to the inflow speed v_1 via mass conservation:

$$v_1 L = v_2 l \tag{1.21}$$

The reconnection rate (M) for Sweet-Parker reconnection is defined as the ratio between the inflow speed and the outflow speed (which is represented as the Alfvén speed v_A):

$$M = \frac{v_1}{v_A} \tag{1.22}$$

if the inflow speed equals the diffusion speed then:

$$v_1 = \frac{\eta}{l} \tag{1.23}$$

substituting for 1 in eq. 1.22 and eq. 1.23:

$$M = (\frac{\eta}{L v_A})^{\frac{1}{2}} = \frac{1}{S^{\frac{1}{2}}} \tag{1.24}$$

where S is the Lundquist number (eq. 1.19). For the corona, $M \approx 10^{-4} - 10^{-6}$. This means that the Sweet-Parker reconnection rate is too slow to explain magnetic dissipation in fast dynamic events, for example solar flares.

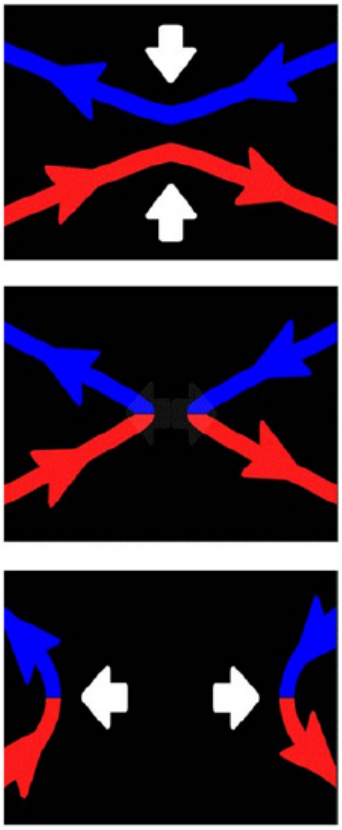

Figure 1.6: Represents the change in fieldline topology in 2D reconnection. Credit goes to the centre for visual computing at the University of California Riverside.

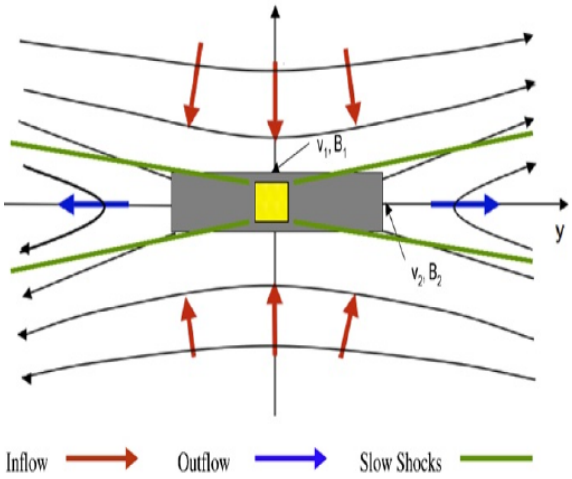

Figure 1.7: 2D reconnection between oppositely directed fieldlines. Red arrows represent inflows and blue arrows represent flows moving away from the diffusion region (grey for Sweet-Parker reconnection and yellow for Petschek reconnection). This image has been adapted from Schindler and Hornig (2000).

1.3.5 Petschek reconnection

The Petschek model describes faster reconnection rates than the Sweet-Parker model. This faster reconnection occurs as the length of the diffusion region is much shorter and the propagation time is much shorter than in the Sweet-Parker model (fig. 1.7). The Petschek reconnection rate is expressed as:

$$M \approx \frac{\pi}{8ln(S)} \tag{1.25}$$

so for the corona, the reconnection rate for the Petschek model is approximately 0.01 - 0.02 and is approximately three orders of magnitude faster than the Sweet-Parker model (Aschwanden 2005).

1.3.6 Magnetic flux emergence

Magnetic flux emergence describes the mechanism that establishes magnetised structures in the solar atmosphere. This flux emergence can be traced on the solar surface. The total flux that emerges onto the solar surface (ϕ) is less than or equal to 10^{24} Mx (Lites et al. 2007) and appears on different scales ($10^{18} \leq \phi \leq 10^{23}$ Mx) forming active regions, ephemeral regions and the inter-network field (van Driel-Gesztelyi and Culhane 2009). Differential rotation at the tachocline amplifies the magnetic field and causes the magnetic field lines to become twisted and contorted which creates flux tubes. These flux tubes have larger magnetic pressures than their environment, but lower plasma density (see eq. 1.26) and because of this, they are able to rise through the convection zone (Zwaan 1985).

$$P_{int} + P_{mag} = P_{ext} \tag{1.26}$$

where P_{int} is the internal gas pressure (which is defined as $\mathrm{P}_{int} = \rho_{int} k T_{int}$), P_{mag} is the magnetic pressure (which is defined as $P_{mag} = \frac{2\mu_0}{B^2}$) and P_{ext} is the external gas pressure (which is defined as $P_{ext} = \rho_{ext} k T_{ext}$), where ρ and T represent density and temperature respectively.

If $\mathrm{T}_{ext} = \mathrm{T}_{int}$, then:

$$\frac{\rho_{int}}{P_{int}} = \frac{\rho_{ext}}{P_{ext}} \tag{1.27}$$

and substituting into equation 1.26:

$$\rho_{ext} - \rho_{int} = \rho_{ext}^{\frac{P_{mag}}{P_{ext}}} \tag{1.28}$$

Buoyancy occurs when the difference between the external plasma density and internal plasma density is greater than 0 (eq. 1.27) and this occurs when the magnetic field strength is approximately 1×10^5 G. The flux tube reaches the photosphere, but does not have the buoyancy to rise into the photosphere. The flux tube stops here

and flux begins to build up. The magnetic field turns from a vertical field to a horizontal one as the fieldlines are "frozen in" to the plasma. An instability called Parker instability (Parker 1966) then occurs where the magnetic field (of the flux tube) piles up under the photosphere and this allows the flux tube to rise through the photosphere and the wider atmosphere (Pariat et al. 2004) as shown in figure 1.8. The Parker instability is a magnetised version of the Rayleigh-Taylor instability. This instability occurs when there is an interaction between two fluids of different densities (in this case, the different density of the flux tube compared to the convection zone). The flux tube is able to rise towards the photosphere at a velocity that depends on the force balance between the buoyancy and the aerodynamic drag (eq. 1.29).

$$\mathrm{v} = (\frac{\pi R}{C_D H})^{\frac{1}{2}} \mathrm{v}_A \tag{1.29}$$

where R is the radius of the flux tube, C_D is the drag coefficient, H is the pressure scale height and v_A is the Alfvèn velocity.

Simulations have also found that a flux tube requires a certain amount of twist to survive the rise through the convection zone. As the magnetic field is flattened under the photosphere, oppositely directed vortices start pulling and tugging on the flux tube. This creates Ω-shaped loops and U-shaped loops which form a serpentine structure that can be seen on the photosphere by looking for a line of small scale positive/negative polarities between the two major polarities of the system. One result of the emergence of active regions are strong hydrogen-alpha brightenings called Ellerman bombs (Ellerman 1917) which share the same physics and energies as microflares. These are represented by the abbreviation "EB'' in figure 1.8. Figure 1.8 describes the rise of the emerging flux tube onto the solar surface and up into the corona and any associated phenomena such as Ellerman bombs and the serpentine field. Ellerman bombs are observed in Hα and Ca II 8542Å lines. They are characterised by deep absorption at the line centre and strong emission in the wings. These events last for approximately 10 minutes, but can reoccur at the same location for up to 30 minutes. These occur following reconnection of small loops that do not have enough strength to overcome the magnetic tension which is trying to pull them below the photosphere. Figure 1.9 shows some key features in an emerging flux region.

Flux emergence is important because the emerging flux region transfers a lot of magnetic energy to the surface. The interaction of the emerging flux with the pre-existing magnetic system can lead to violent solar activity such as flares, eruptions, jets and Coronal Mass Ejections (CMEs). By studying emerging flux regions we can also understand the solar dynamo and how it is used in flux creation.

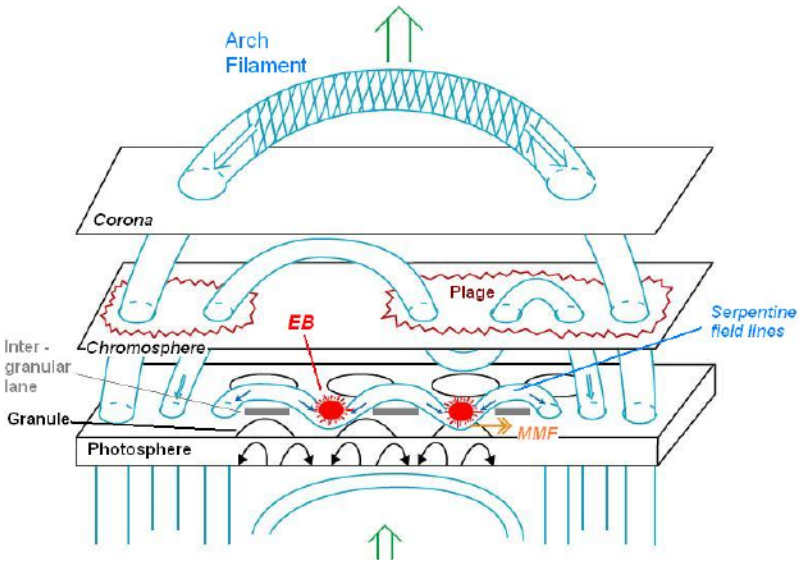

Figure 1.8: Sketch of flux emerging through the photosphere and into the upper atmosphere. Figure was produced by Pariat et al. (2004).

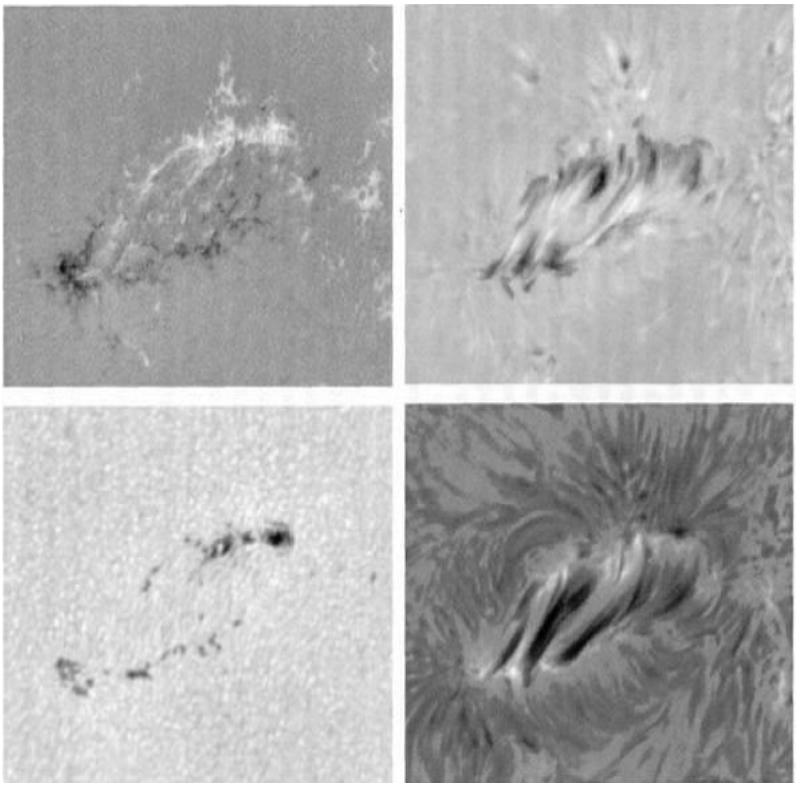

Figure 1.9: Multi-wavelength observations of an emerging flux region. Top,left is the line-of-sight (LOS) magnetogram with white representing positive polarity and black, negative polarity. Top, right is the Dopplergram with white representing material moving towards the observer and black representing material moving away from the observer. Bottom, left is the continuum map. Bottom, right is the Hα image showing an arch filament system. This figure is adapted from Strous et al. (1996).

1.4 Emerging flux

Flux emergence can occur in regions where there is already a pre-existing active region. Here, a flux tube has already risen to the solar surface; however, a second flux tube then rises onto the solar surface. The signature of flux emergence into pre-existing active regions can be seen in the upper layers of the Sun.

1.4.1 Flux emergence in the photosphere

In the photosphere, anomalous alignments and darkenings of intergranular lanes (or fibrils) are detected before the first signs of an emerging flux region. Fibrils are often formed in mixed-polarity regions because horizontal flux tubes often reconnect with small low-lying loops (Wang et al. 2011).

Near newly forming magnetic polarities, there are strong downdrafts which last approximately an hour. Polarities grow by adding flux to the already formed polarity and the resulting umbrae are formed by the coalescence of flux with the same polarity. At birth, separation speeds are around 1 to 2 km s^{-1}, after a few hours the speed decreases to approximately 500 ms^{-1} and over a few days, the average speed is approximately 100 ms^{-1} (Gaizauskas 1993). The centres of opposite polarities are typically separated by 150 Mm (Zwaan 1985; Zwaan 1992; Priest and Forbes 1989; Gaizauskas 1989). As previously mentioned, serpentine field lines are formed by Ω-loops and U-loops. U-loops have been theorised for many years (Parker 1984; Spruit et al. 1987). U-loops are important in explaining the decay of active regions (Zwaan 1992). While the ends of the U-loops are located in the photosphere, the bottom of the loops are located in the convection zone. The first detection of these U-loops was by van Driel-Gesztelyi et al. (2000). Work by Bernasconi et al. (2002) has shown that the magnetic configuration of magnetic bipolar features (MBFs) is oriented opposite to the leading active region polarity and suggests that these features correspond to U-loops. This is also confirmed in Xu et al. (2010).

Several studies that looked at flux emergence into active regions aim to measure the separation speeds between polarities. In Harra et al. (2010), the separation speed between the polarities in the photosphere was found to be 1 kms^{-1} which is comparable to what was found by Otsuji et al. (2007) and Gaizauskas (1993). In the early stages of flux emergence and in terms of local helioseismology, there are localised upflows and downflows, which supports current rising flux rope theories (Kosovichev 2009). However, Kosovichev (2009) does not find evidence for large-scale flows which would indicate large-scale magnetic structure.

The surface of the Sun is covered in small-scale mixed polarity regions that in their entirety are known as the magnetic carpet (Title and Schrijver 1998). The entire carpet is replaced in about 48 hours (see figure 1.10).

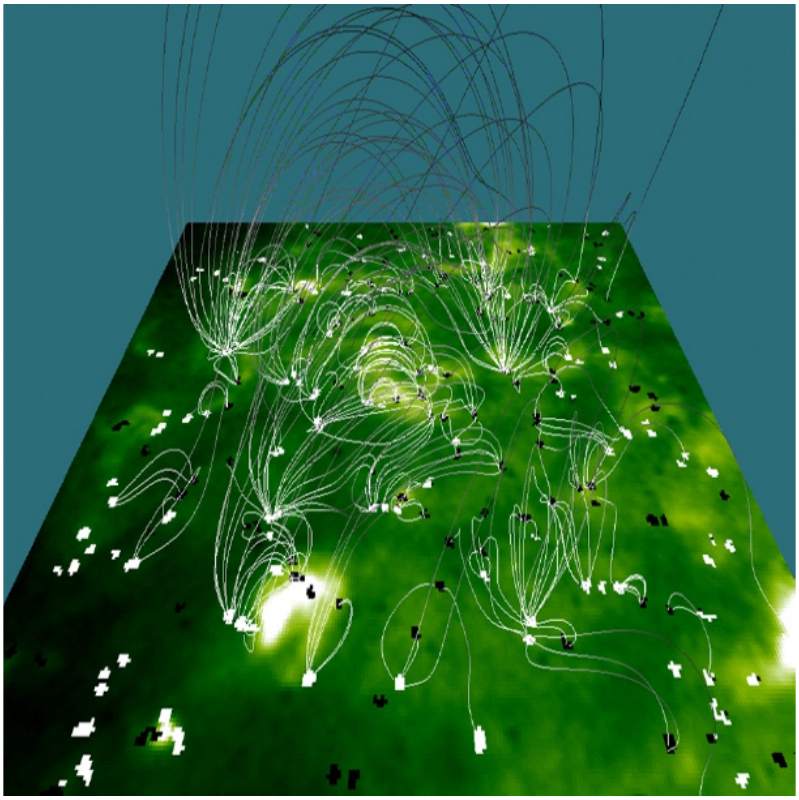

Figure 1.10: This image shows the small-scale mixed polarity regions and the loop structures of the magnetic carpet (Title and Schrijver 1998; Schrijver et al. 1998). Image is from http://umbra.nascom.nasa.gov/ssu/view1.jpg.

1.4.2 Chromospheric response to emerging active regions

As we compare the effect of flux emergence in the photosphere with the response in the chromosphere, we find that the magnetic structure in the photosphere is very complex with many additional structures in the centre of the emerging flux region, while in the chromosphere the magnetic structure is much simpler (compared to the photosphere) and is dominated by low-lying He I loops (Xu et al. 2010). In this section, we describe how the chromosphere responds to active regions and emerging flux.

In Ca II K and Hα lines, active regions consist of bright patches with granular structure called plages or chromospheric faculae (connection with photospheric faculae). Statistical studies show that only 23% of flux emergence reaches the chromosphere (Martínez González and Bellot Rubio 2009). The structure of the chromosphere has been observed to be a wealth of wave and oscillatory phenomena that appear as longitudinal and transverse motions (Okamoto et al. 2007).

There are a number of signatures in the chromosphere for flux emergence:

1. **Arch filament systems** Arch filament systems are a very obvious indicator of emerging flux regions and these arches traverse the magnetic inversion line in newly formed sunspot groups. These systems usually last for two days but can last for up to four days. Individual arch loops have lifetimes of approximately

Type	Length (10^9cm)	Temperature (MK)	Density (10^9 cm^{-3})	Pressure (dyne cm-2)
Bright points	0.1- 1	2	5	3
Active region	1 to 10	3	1 - 10	1 - 10
Giant arches	10 to 100	1 - 2	0.1 - 1	0.1
Flaring loops	1 - 10	>10	>50	>100

Table 1.1: Types of X-ray coronal loops and their parameters. Information from Reale 2010.

20 to 30 minutes and can bring up to 10^{19} Mx of flux to the surface. The arch filament systems have a unique velocity pattern that distinguishes them from other arch systems such as field transition arches (Zwaan 1985; Zwaan 1992; Priest and Forbes 1989; Gaizauskas 1989).

2. **Surge activity** Surge activity that lasts several hours might be the first indicator of flux emergence (Kurokawa 1989; Kurokawa et al. 1992).

3. **Faculae** Faculae in the chromosphere brighten in Hα and CaII K and precede the arch filament stage (Zwaan 1985; Zwaan 1992; Priest and Forbes 1989; Gaizauskas 1989).

4. **Chromospheric brightenings** Chromospheric brightenings may be an indication that two different flux systems undergo magnetic reconnection (Guglielmino et al. 2008).

While understanding the response that the chromosphere has to flux emergence into active regions is important, it has not been as widely studied as the photosphere or the corona. Partly this is due to the difficulty in understanding the chromospheric layer.

1.4.3 Coronal response to emerging active regions

In this section, we describe the coronal responses (coronal loops, outflows and jets) to active regions and emerging flux. In the corona, active regions are observed as Ω-shaped loops which can either connect to opposite polarities in the same active region or to adjacent active regions. In X-ray wavelengths, there are different types of coronal loops (as shown in table 1.1).

1.4.3.1 Coronal Loops

Coronal loops come in two main types: cooler (500,000 K), more resolved loops and hotter (2 million K), more diffuse loops. Ne VII (at 500,000 K) observations show thin spikes diverging outwards from the emerging flux region on distance scales between 10,000 and 100,000 km which have lifetimes of approximately 30 minutes.

However, individual loops (at 2 million K, detected using the Skylab ATM spectroheliogram) evolve on time scales of approximately 6 hours (Zwaan 1985; Zwaan 1992; Priest and Forbes 1989; Gaizauskas 1989; Sheeley 1980).

Filled loops are brighter than the background corona and produce strong EUV and X-ray emission. Schmieder et al. (2004) found that soft X-ray and EUV loops had different footpoints and the soft X-ray loops were longer and higher than the EUV loops. Finally, the EUV loops were mainly heated at their footpoints and anchored in weaker magnetic field (compared to the soft X-ray loops), while the soft X-ray loops were brightened in response to magnetic reconnection. (Winebarger and Warren 2005) found that X-ray loops can precede EUV loops by as much as 3 hours and that they do not cool to form the EUV loops.

1.4.3.2 The creation of outflows as a response to flux emergence

New emerging flux can also play a role in creating outflows and there are different ways in which they can be created. Outflows are described as plasma flowing along "open" fieldlines towards an observer. Most involve reconnection, although some involve different mechanisms, for example compression of parallel field lines (Murray et al. 2010). Previous studies have looked at how new emerging flux can trigger outflows. It has only been in the last several years since the launch of Hinode that outflows have been widely studied. The following are possible mechanisms:

1. **Chromospheric evaporation**
   Particles are accelerated down the loop legs towards the chromosphere, particles impact the chromospheric plasma, which heats this plasma and the plasma expands into the Corona. Chromospheric evaporation is driven by reconnection caused by continuous flux emergence and braiding by photospheric motions (Del Zanna 2008).

2. **Coronal plasma circulation**
   Magnetic field lines confine large-scale plasma flows in the low-β plasma of the corona as it continuously circulates in separate coronal structures. This flow pattern is long lasting on large scales (Marsch et al. 2008). Marsch et al. (2008) suggests that coronal plasma circulation can be interpreted as mass supply to and mass loss from Corona. The origin and driver of the plasma flow lies in magnetoconvention below the photosphere.

3. **Expansion of large-scale reconnecting loops**
   Comparing large-scale magnetic field model and Hinode EIS data shows that strong outflows can occur near expanding large-scale reconnecting loops or "open" field (Harra et al. 2008).

4. **Impulsive heating of AR footpoints**
   Hot plasma outflows observed near the base of the corona were proposed

as direct evidence for impulsive heating by Hara et al. (2008). Hara et al. (2008) suggest that high velocity components of the blue wings of Fe XIV and Fe XV line profiles are consistent with nanoflare heating model of Patsourakos and Klimchuk (2006).

5. **QSLs**
   Quasi-Separatrix layers (QSLs) are areas where there are sudden changes in magnetic connectivity. Fieldlines can continuously slip across each other during reconnection, leading to successive rearrangements of the connections between neighbouring fieldlines along the QSLs (Aulanier et al. 2006). Release of magnetic free energy could occur when the thickness of QSLs is small enough for reconnection to take place. To drive outflows, a QSL between "open" or large-scale field lines and closed field lines is also required (Baker et al. 2009)

6. **Waves**
   Oscillations and waves have been observed in various solar structures: plumes, prominences and loops. Perturbations were found to travel along the plumes at the sound speed suggesting propagating slow magneto-acoustic waves (de Moortel 2009). It is not immediately obvious how AR outflows relate to propagating intensity perturbations, but there are notable similarities for example the location of apparent velocities at AR edges.

7. **Continuous AR expansion**
   Outflows are accelerated along "open" field as the AR expands horizontally. Murray et al. (2010) suggests that all that is needed to drive outflows is a horizontally expanding AR and a nearby compressible magnetic field with a vertical component.

The strongest outflows have been found in the lowest density regions (e.g. Del Zanna 2008, Harra et al. 2012). There seems to be a connection with the velocity of outflows and the temperature above 1 million K, which suggests a link to coronal heating mechanisms. This raises questions such as why are outflows detected at the edges of active regions and why do they persist?

1.4.4 Formation of jets in the solar atmosphere

Jets are formed in the solar atmosphere following reconnection between the magnetic field of the emerging flux region and the pre-existing magnetic field (Heyvaerts et al. 1977). The jets have an inverted Y-shape in the chromosphere (Shibata et al. 2007) and in the corona (Shibata et al. 1992). Jets have been associated with flares (Shibata et al. 1992), type III radio bursts (Chiuderi-Drago et al. 1986), Hα surges (Shibata et al. 1992) and bright points (Doschek et al. 2010). Jets have been detected in the chromosphere (e.g. Morton et al. 2012), in the EUV

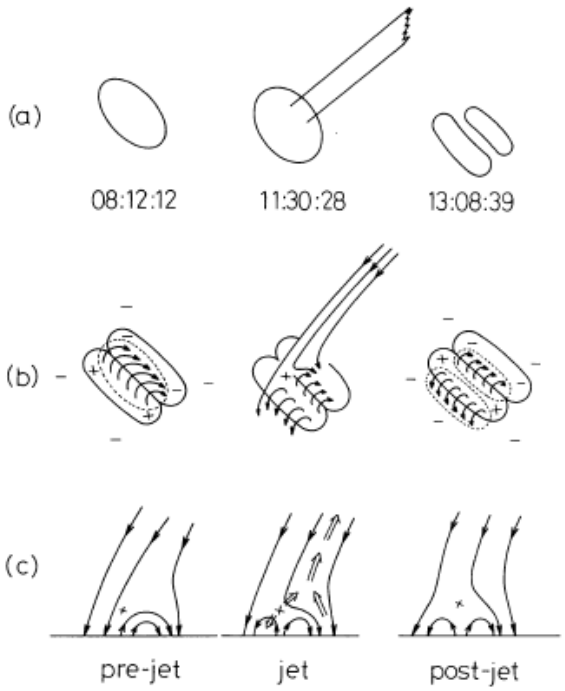

Figure 1.11: cartoon of jet formation from Shibata et al. (1992). (a) shows cartoon of SXT image of active regions and jets before jet, during the jet and after the jet has formed. (b) shows a birds-eye view of the inferred magnetic field before, during and after the jet formed. (c) shows a side view of the magnetic reconnection between the emerging flux and the pre-existing coronal field before, during and after the jet formed.

corona (e.g. Culhane et al. 2007) and the X-ray corona (e.g. Shibata et al. 1992;Moore et al. 2011) as well as in white light (Wang et al. 1998) and ultraviolet (Brueckner and Bartoe 1983).

The first model of X-ray jets was proposed by Shibata et al. (1992)(see figure 1.11). This model suggests that the jets are created by reconnection between emerging closed loops and pre-existing "open" or "open-like" coronal loops (this is called interchange reconnection). Reconnection can heat the plasma to X-ray temeperatures by a process called "Joule dissipation". This process occurs when current is passed through a medium that is electrically resistive and heat is produced. This heated plasma is then transferred to the open field and the newly reconnected closed field. The jet is released along the "open" or "open-like" field lines. Some plasma also travels downwards, producing a hot flare loop or bright point (BP). The model was then taken a step further by Yokoyama and Shibata (1995) to recreate the observed properties of the X-ray jet and the Hα surge. However, the model could not explain the observed densities, and evaporation was omitted because conduction was not included in the model. The model of Miyagoshi and Yokoyama (2003) included conduction and chromospheric evaporation. They found that magnetic energy was converted to thermal energy through slow shocks formed by Petschek-type reconnection. These shocks then transport the thermal energy along magnetic field

Type of jet	Velocity (km s^{-1})	Length (km)	Frequency (hr^{-1})
X-ray	10 - 1000	10,000 - 400,000	10
EUV	30 to 240	up to 20,000	1 - 12
Chromosphere	10 to 100	2,000 to 5,000	12 - 15

Table 1.2: Characteristics of jets in the Chromosphere, in EUV and X-ray. Figures taken from Cirtain et al. (2007); Shimojo et al. (1996); Kamio et al. (2007); Moreno-Insertis et al. (2008); Moreno-Insertis and Galsgaard (2013); Morton (2012); Shibata et al. (2007); Liu et al. (2009)

lines to the chromosphere. Dense plasma then rises from the chromosphere along reconnected field lines producing high density (evaporation) jets and low-density jets.

The 3D MHD model of Moreno-Insertis et al. (2008) was compared with Hinode EIS and XRT observations. The model showed that many of the observed X-ray jet properties can be explained by evaporation flows including the inverted-Y shape seen in the EIS and XRT observations. However, the model cannot explain the helical structure first seen in Shibata et al. (1992). In table 1.4.4, we show the typical characteristics of chromospheric, EUV and X-ray jets.

1.5 The eruptive Sun

It is clear from previous work that flux emergence can lead to violent eruptions of plasma from the Sun into the heliosphere. Solar flares and Coronal Mass Ejections (CMEs) are these violent eruptions and in sections 1.5.1 and 1.5.2, we will briefly discuss the standard models for solar flares and CMEs.

1.5.1 Solar Flares

A solar flare is defined as a massive release of energy from the corona. Approximately 10^{32}J of energy is released from the coronal magnetic field and can accelerate electrons, protons and ions to relativistic velocities (via shocks). Emission from flares is enhanced across the electromagnetic spectrum and can last between a few minutes to a few hours (Benz 2008).

The strength of a flare is based on logarithmic scale that is labelled A, B, C, M and X, with A being the weakest flare (peak X-ray flux is at $< 10^{-7} Wm^{-2}$) and X being the strongest flare (peak x-ray flux is at $> 10^{-4} Wm^{-2}$). Each class can range from 1 to 10 and is represented by a number after the class letter (for example, A3.0). The number represents the magnitude of the flare: so a A3.0 flare will have a peak X-ray flux of 3.0×10^{-7}Wm^{-2} and a Bl.4 flare will have a peak X-ray flux of 1.4×10^{-6}Wm^{-2}.

The CSHKP 'standard' eruptive flare model (Carmichael 1964; Sturrock 1966; Hirayama 1974; Kopp and Pneuman 1976) (fig. 1.12) is the current model that

describes flares, but not all flare observations. In this model, a filament of cool, dense plasma is formed over the polarity inversion line (PIL). As the overlaying magnetic field expands, the filament rises and a current sheet is formed above the PIL and is stretched. When the current sheet becomes thin enough, reconnection can occur that provides kinetic energy to the filament and the filament erupts. However, filaments are not always required for flares: a non-filament flare is driven by photospheric motions along the PIL or flux emergence (both below the flaring region) (Aschwanden 2005).

The magnetic fields in the photospheric layer provide an important role in the creation of flares. In the impulsive phase of a flare, the magnetic field (in line of sight magnetograms) can change quickly and this change in not reversible (e.g. Sudol and Harvey 2005). This might be due to a change of direction by the magnetic field rather than a change in strength. Chen et al. (2007) also discovered rapid changes to the photospheric magnetic field in 40% of X-class flare cases, 17% of M-class flare cases and 10% C-class flare cases.

1.5.2 Coronal Mass Ejections (CMES)

CMEs are described as fast evolving and expanding magnetic structures that carry "frozen in" plasma into the heliosphere. They occur in the corona and are highly energetic events. The difference between CMEs and flares has been debated for a long time, but the consensus is that CMEs and flares are different manifestations of a magnetic instability (e.g. Goff et al. 2007). CMEs are thought to be powered by magnetic free energy rather than other sources of energy (such as kinetic, gravitational or thermal energy), as these sources of energy are not sufficient to power a CME (Forbes 2000). The typical CME structure is of a filament/prominence core with a dark cavity surrounded by a bright shell of material (fig. 1.13)

While models differ on the trigger and driving mechanisms of CMEs, most models describe at some point the requirement for a twisted flux rope and a vertical current sheet under the flux rope.

1.5.3 Coronal diagnostics

1.5.3.1 Formation of spectral lines

Spectral lines are formed when there is a change in energy of an electron within an atom. This change can result in either an emission line (when an electron falls to a lower energy level and emits a photon) or an absorption line (when a photon is absorbed by an electron and the electron rises to a higher energy level). In either case an intensity change will be detected (spike for emission, drop for absorption). Different atoms have different spectral lines due to having different energy levels and atomic configuration.

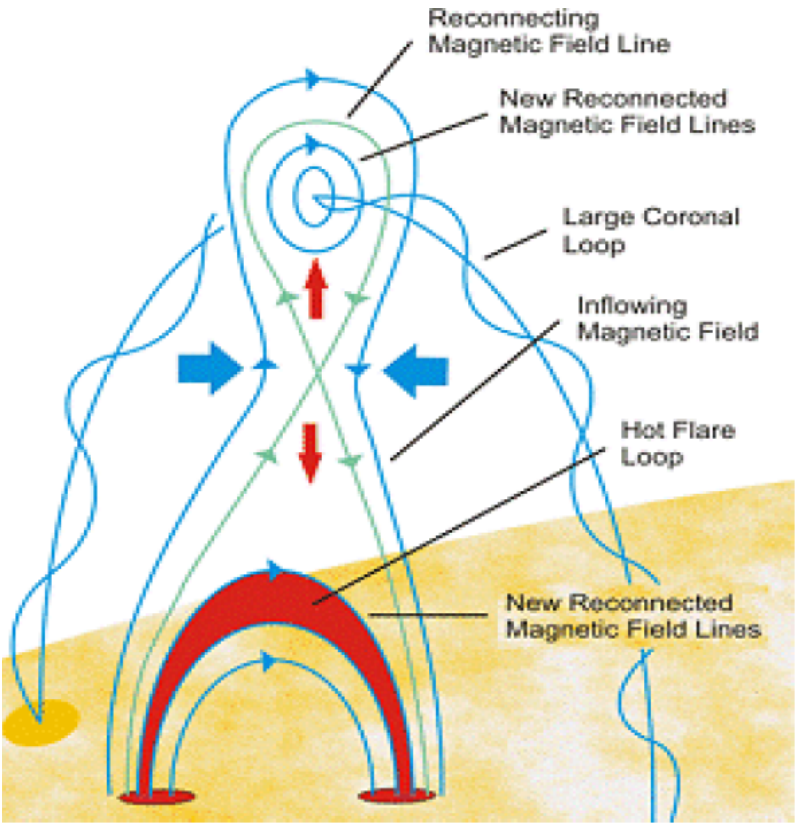

Figure 1.12: Standard picture of CSHKP flare model, from http://science.portalhispanos.com/wordpress/wp-content/uploads/2009/11/flare_model.gif.

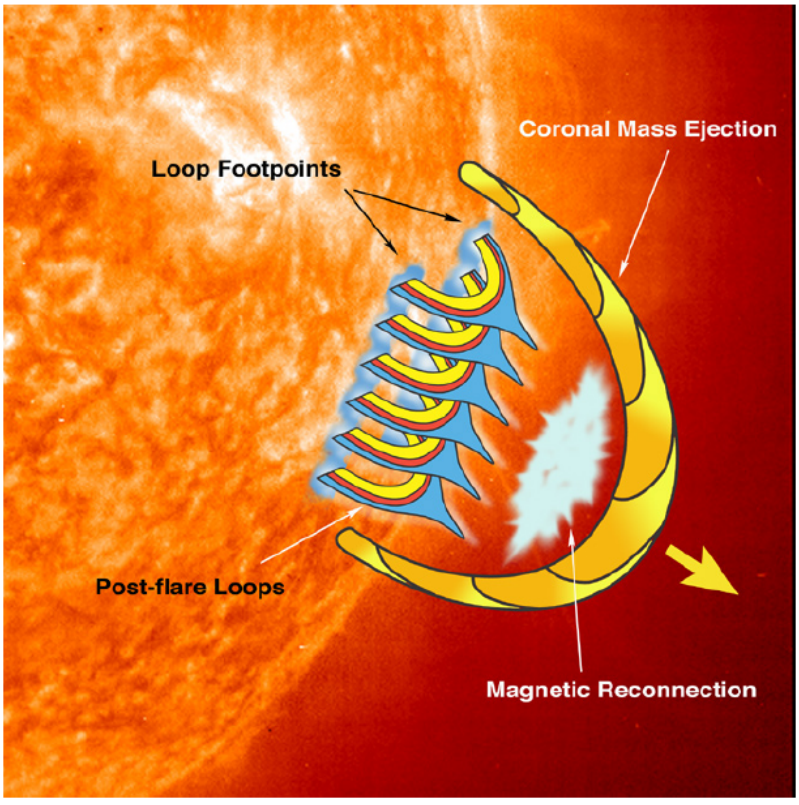

Figure 1.13: Cartoon of a Coronal Mass Ejection, from http://sprg.ssl.berkeley.edu/~tohban/nuggets/images/Gallagher_cartoon.jpg.

A spectral line will normally take on a Gaussian curve with the peak as the rest wavelength of that spectral line. This is due to various line broadening problems such as natural broadening (this follows the Heisenberg uncertainty principle), Doppler broadening (caused by the distribution of velocities of particles) and other types of broadening that are affected by pressure, resonance, an electric field and the Van der Waals forces on particles.

1.5.3.2 Measuring flows

Flows are defined as the motion of plasma in the solar corona along the line of sight. They can be detected by measuring the wavelength shift of a spectral line (called a Doppler shift). The Doppler shift in terms of wavelength is defined as:

$$\lambda = \lambda_0(1 - \frac{v}{c}) \tag{1.30}$$

where λ is the observed wavelength, λ_0 is the rest wavelength, v is the Doppler velocity and c is the speed of light in a vacuum. Rearranging for v:

$$v = c(\frac{\lambda - \lambda_0}{\lambda_0}) \tag{1.31}$$

this means that where $\lambda > \lambda_0$, the plasma is moving away from the observer and is redshifted and where $\lambda < \lambda_0$, the plasma is moving towards the observer and is blueshifted. Blueshifts are defined as upflows (in closed loops) or outflows ("open" loops) and redshifts are defined as downflows.

1.6 Aims of the Thesis

Understanding the role of new flux emerging into a pre-existing active region is important in understanding the physical processes (as shown earlier in chapter 1) that create the activity seen in the upper atmosphere. The research presented in this work combines EUV imaging, photospheric magnetic field measurements and EUV spectroscopy to study how two different emerging flux regions affect the pre-existing active regions they emerge into and the wider affect on the local atmosphere.

1.7 Outline of the Following Chapters

Chapter 2 describes the instruments and telescopes used in this work. In chapter 3, we present the results of our flux emergence study and compare the two emerging flux regions. In Chapter 4, we look ahead to future solar telescopes and how our results can be extended using the next generation of solar telescopes. We also consider the possibilities for future work on the role of flux emergence in the solar atmosphere.

Chapter 2

The Telescopes

In this chapter the telescopes and instruments used in this work are described.

2.1 SOlar and Heliospheric Observatory (SOHO)

SOHO was built in the early 1990s by a European consortium led by Matra Marconi Space (now Astrium) and launched on the 2nd December 1995. It was originally planned as a two-year mission, but is still in use to the current day. The spacecraft orbits at the Earth-Sun Ll point and follows a heliocentric orbit. The telescope studies the Sun in wavelengths from optical to ultraviolet and also uses magnetic data. There are twelve instruments on SOHO, however we will only discuss one: The Michelson Doppler Imager (MDI).

2.1.1 Michelson Doppler Imager (MDI)

MDI studies the velocity and magnetic fields in the photosphere to learn about the photosphere and to investigate the solar interior using helioseismology. MDI uses a 1024×1024 CCD camera and looks at the Sun at a wavelength of 6767.8 Å. A full-disk image of the Sun has a resolution of 4 arcseconds. However, a high-resolution field image of an 11 arc-minute square region of the Sun can provide a resolution of 1.25 arcseconds. MDI provides velocity and continuum data as well as magnetogram data. The magnetogram has an image cadence of 96 minutes. Table 2.1 describes the key parameters of the MDI instrument. Line-of-Sight magnetograms are made using Zeeman splitting and by measuring the Doppler shifts of the right and left circularly polarised light. The magnetic flux density is given by the difference between the Doppler shifts of both polarisations. Figure 2.1 shows the light path through the instrument and the primary optics. The green components are the telescope, the filter wheels and the Imaging Stabilisation System. The blue components are the filters and the re-imaging optics. The red components are the beam distribution system and the CCD camera.

Telescope Aperture	12.5cm
Focal plane Array	1024x1024 21 μm pixel
Resolution	4" (full disk) and 1.2 (high resolution)
FOV full disk	34 x 34 arcmin
FOV high resolution	10.5 x 10.5 arcmin
Spectral range	6767.8Å $\pm$ 190mÅ
Magnetic field noise	20G

Table 2.1: MDI instrument information from Scherrer et al. (1995).

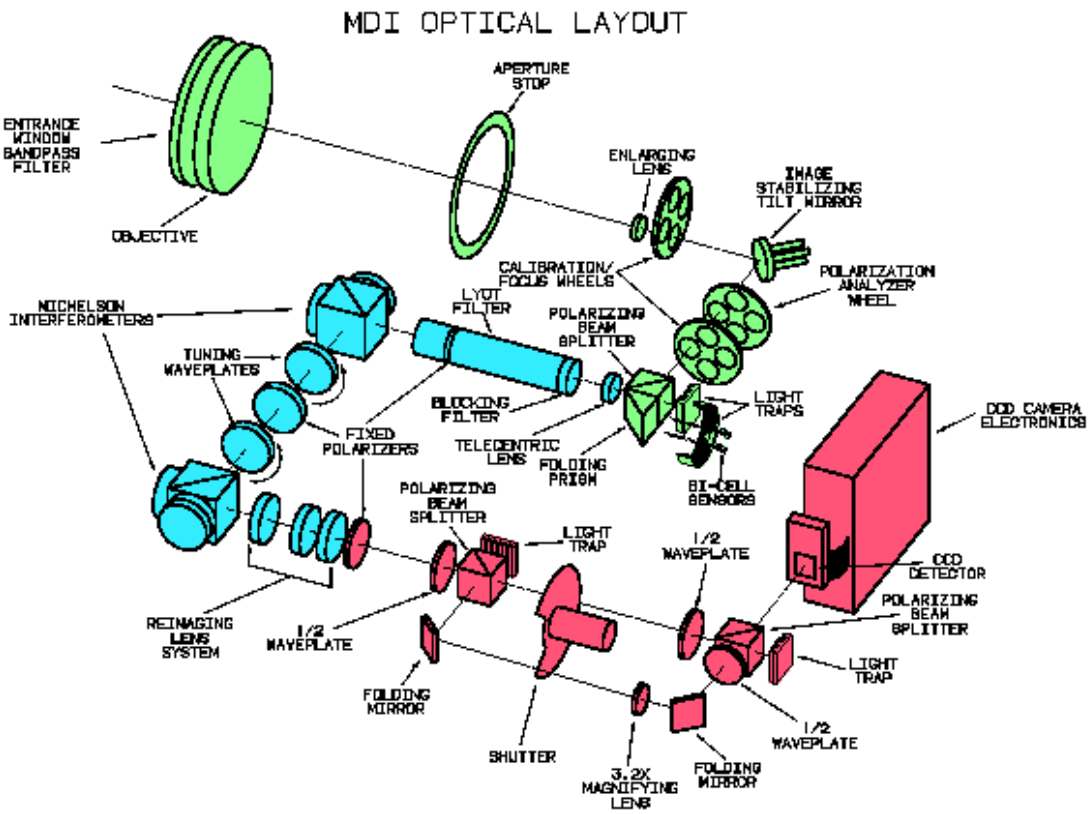

Figure 2.1: Image shows the components of the MDI instrument. Image from Scherrer et al. (1995).

2.2 Hinode (Sunrise), formerly Solar-B

Hinode is a JAXA solar mission with collaboration with the USA and UK. It was launched from Japan on the 22nd September 2006 (UTC time). The telescope is in a Solar-synchronous orbit with an initial orbit of 280 km perigee and an apogee of 686 km. The mission was originally planned as a three year mission, but is still being used successfully today. The telescope works at three wavelength ranges: Optical, extreme ultraviolet and X-ray and has three instruments:

2.2.1 Solar Optical Telescope (SOT)

SOT is a 0.5 metre Gregorian optical telescope with over a 44.4 square arcmin field of view and the angular resolution is approximately 0.2 arcseconds. The instruments associated with SOT are, a broadband filter imager (BFI) which images the photosphere and chromosphere, the narrowband filter imager, which is capable of producing magnetogram and Dopplergram images and the spectropolarimeter (SP) which makes very sensitive vector magnetograph maps of the photosphere. The Hinode telescope is shown in fig. 2.2.

2.2.2 X-ray telescope (XRT)

This telescope, like all current X-ray telescopes in Solar and Astrophysics, uses grazing incidence optics to image the corona's hottest areas (0.5 to 10 million K) with an arcsecond angular resolution and has a field of view of 34 arcminutes. XRT has one aluminium-Polyimide pre-filter and ten focal-plane filters ranging in thickness between 1600 Å for the thin aluminium-mesh filter to 2.5 mm for the white light filter.

2.2.3 Extreme-Ultraviolet Imaging Spectrometer (EIS)

This spectrometer obtains spatially resolved spectra in two wavelength bands: 170-212 Å and 246-292 Å with a spatial resolution of approximately 2 arseconds. The field of view is 560 $\times$ 512 square arcseconds. These wavebands are able to detect emission temperatures between 50,000 and 20 million K and EIS is used to study the upper transition region and corona. EIS is able to produce intensity, Doppler velocity and line width maps in the various wavebands. MSSL led the consortium that built EIS and continues to be the hub for EIS data. The EIS exposure times for coronal phenomena are: 10 seconds for active regions, 30 to 60 seconds for quiet Sun and 1 second for flares.

The EIS instrument design uses multilayer coatings on both the mirror and the grating. This allows the use of normal incidence instead of a grazing incidence design used by previous spectrometers. The CCDs are also thinned back-illuminated

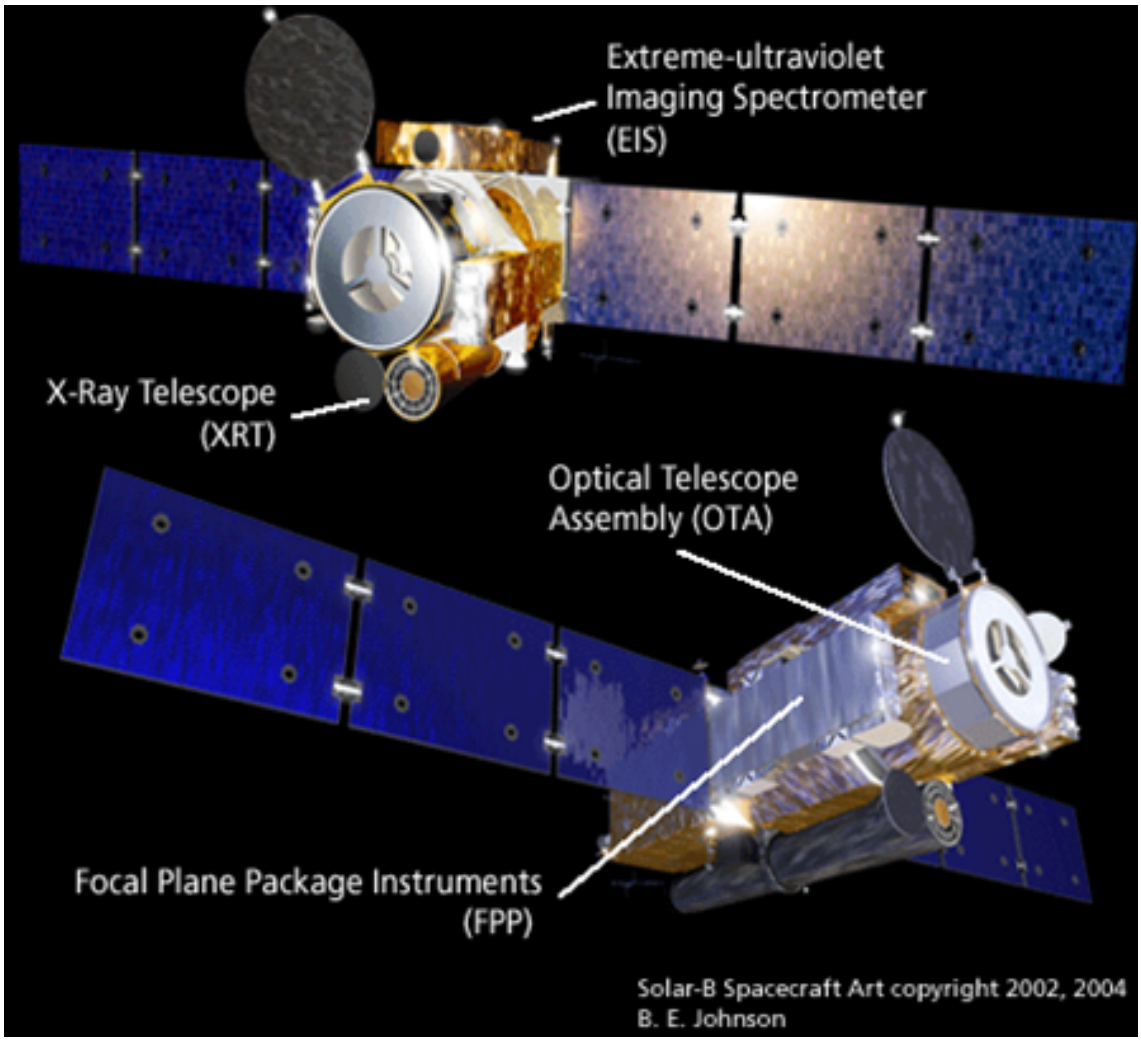

Figure 2.2: Image shows the Hinode telescope highlighting the different instruments on the telescope.

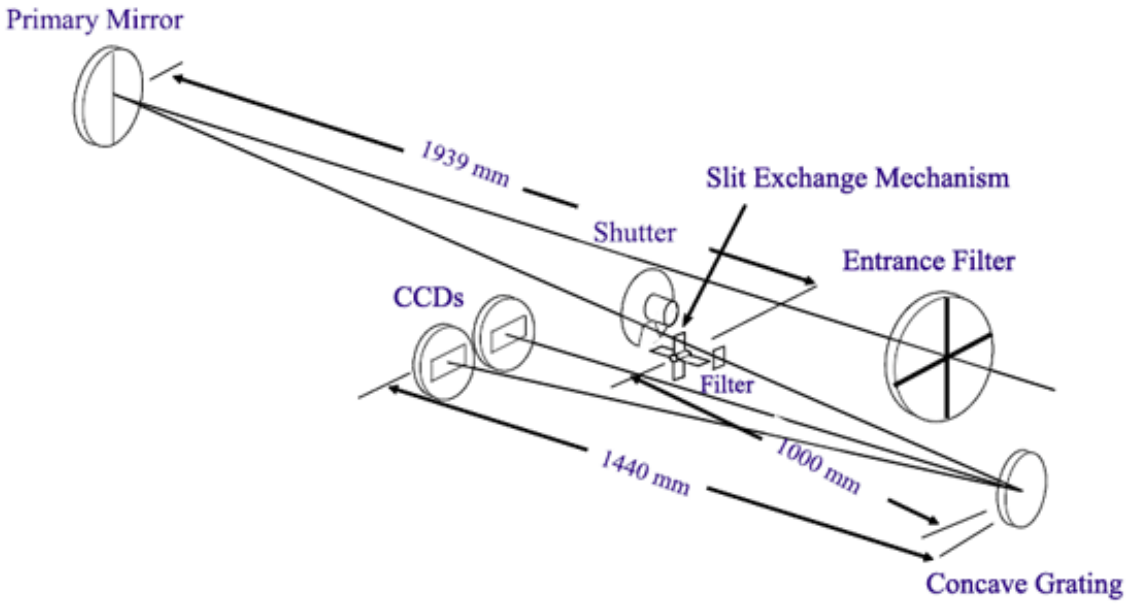

Figure 2.3: Image shows the optical layout of the EIS instrument. Image is from Culhane et al. (2007).

Wavelength bands	170 - 210 Å and 250 - 290 Å
Peak effective area	0.30 cm^2 and 0.11 cm^2
Spatial resolution	2 arcsec
Field of view	6 arcmin × 8.5 arcmin, offset center ± 15 arcmin E -W
Raster	1 arcsec in 0.7s
Slit/Slot widths (arcsec)	1, 2, 40 and 266
Spectral resolution	47 mÅ at 185 Å ;1 pixel = 22 mÅ
Velocity resolution	3 km s^{-1} for Doppler velocities; 20 km s^{-1} for line widths
Temperature coverage	Log T = 4.7, 5.6, 5.8, 5.9, 6.0 - 7.3 K

Table 2.2: EIS instrument information adapted from Culhane et al. (2007).

and this allows quantum efficiency (QE) values to be two or three times higher than microchannel plate systems. One disadvantage of this technique is that an individual multilayer has a very narrow passband.

The spectrometer works as follows: photons from the Sun enter through a 1500 Å Al filter (this stops the transmission of visible photons). The photons are focused by the primary mirror onto a slit and then incident on a torodial concave grating. The Mo/Si multilayer coatings are applied to matching halves of the mirror and grating. The diffracted photons are registered by the CCDs. The exposure times are controlled by a rotating shutter while a slit exchange mechanism can select four possible apertures - two spectral slits (1″and 2″) and two spectral image slots (40″and 266″). There is a second Al filter mounted behind the slit exchange mechanism to provide redundancy. EIS is a rastering spectrometer and rastering is provided by rotating the primary mirror. This is shown in fig. 2.3.

2.2.3.1 EIS observations

There are two modes of EIS observations that can be selected: Sit-and-stare and scanning. The sit-and-stare have the same field of view (FOV) as the slit/slot in the X direction and the primary mirror/spacecraft pointing is fixed on a specific target. Raster images can be produced by rastering either the slit or slot within the EIS scan range of 6 arcmin in X and 8.5 arcmin in Y. Table 2.2 describes the key parameters of the EIS instrument.

2.2.3.2 Instrument effects

When using EIS data there are a number of instrument effects that need to be taken into account:

1. Orbital Variation
2. Slit tilt
3. Detector offset
4. Line width variations
5. Grating tilt

The orbital variation effect results in a shift in the spectral line position as Hinode orbits the Earth and is caused by thermal changes across the instrument. This shift can cause velocity variations which are dependent on wavelength (35 km s^{-1} for Fe XII 195 Å and 24 km s^{-1} for Fe XV 284 Å). This effect can be corrected by using the housekeeping method outlined in Kamio et al. (2010). This method creates a spectrum drift model using an artificial neural network and the temperature distribution of the instrument and is particularly suitable for active region studies as a velocity reference is not required for the observing field.

The slit tilt effect is due to the slits not being perpendicular to the dispersion (X) axes of the CCDs. The 1″ slit tilt is 1.18×10^{-5} Å $pixel^{-1}$ and the 2″ slit tilt is 1.09×10^{-4} Å $pixel^{-1}$. The slit tilt effect can be corrected using the eis_wave_corr and eis_tilt_correction procedures in the EIS solarsoft tree.

The detector offsets are 16″ in the y-axis and 2″ in the x-axis between the short and long wavelength CCDs and can be addressed with the eis_ccd_offset procedure.

There is a line width variation between the 1″ and 2″ slits. The instrumental width is 0.054 Å and 0.057 Å for the short and long wavelength CCDs. The 2″ slit has an instrumental width of 0.061 Å and 0.064 Å .

The grating tilt between the grating and the CCD is less than 1 pixel between 186.88 Å and 195.12 Å and is important to correct for when deriving densities in a loop for example. We use EIS data in this work to study changes in Doppler velocity and line width as a result of emerging magnetic flux.

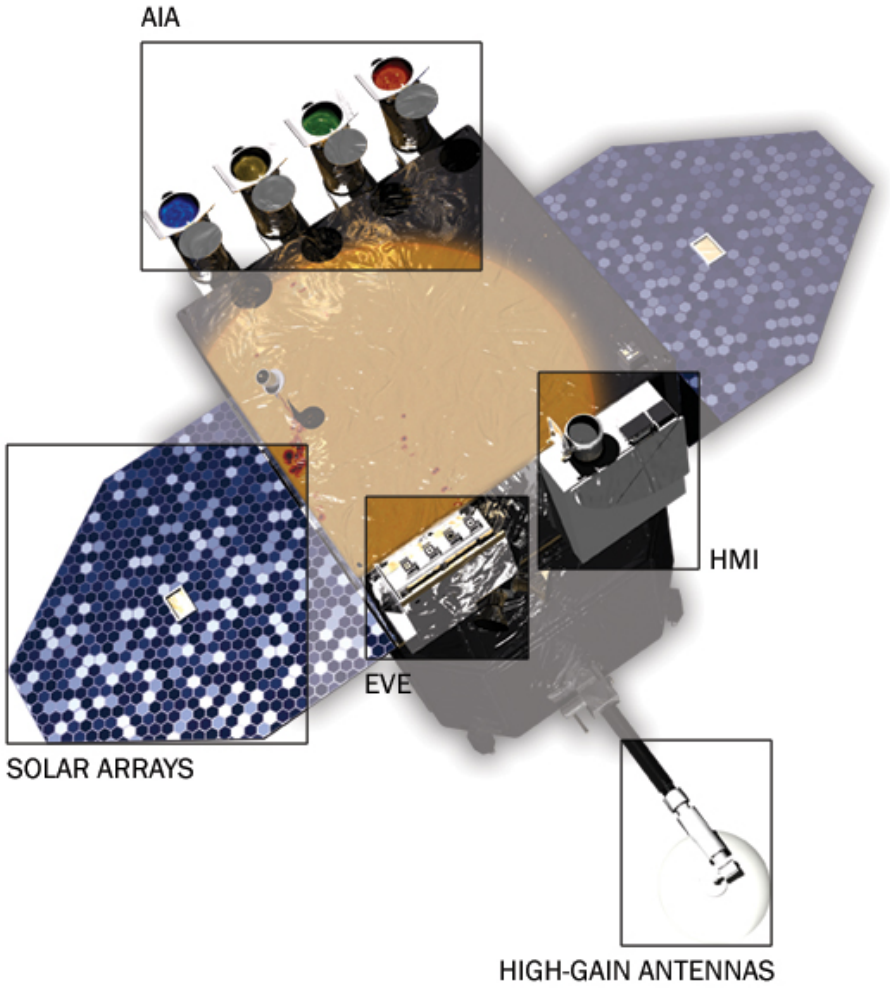

Figure 2.4: Image shows the Solar Dynamics Observatory and the three instruments.

2.3 Solar Dynamics Observatory

The Solar Dynamics Observatory (SDO) was launched in February 2010 from launch complex 41 at Cape Canaveral. The telescope is in a circular geosynchronous orbit at an altitude of 36,000 km. The instruments generate over one terabyte of data per day. There are three instruments on board SDO:

2.3.1 Extreme Ultraviolet Variability Experiment (EVE)

EVE measures the Sun's EUV irradiance and has better spectral resolution, accuracy and precision over previous instruments. EVE also has a lower time cadence compared to past instruments. The main aim of EVE is to further our understanding of the relationship between the variations in EUV and magnetic field changes. The time cadence is every 10 seconds per 100% cycle.

2.3.2 Helioseismic and Magnetic Imager (HMI)

HMI studies solar variability and characterises magnetic activity. The instrument also studies the physical processes inside the Sun and how they are related to the surface magnetic field. HMI produces continuum, Doppler velocity and line-of-sight and vector magnetogram images in two time cadences: 45 and 720 seconds and has a resolution of 1 arcsecond. The instrument observes the Sun at 6173 Å . HMI is the natural replacement to the MDI instrument on SOHO.

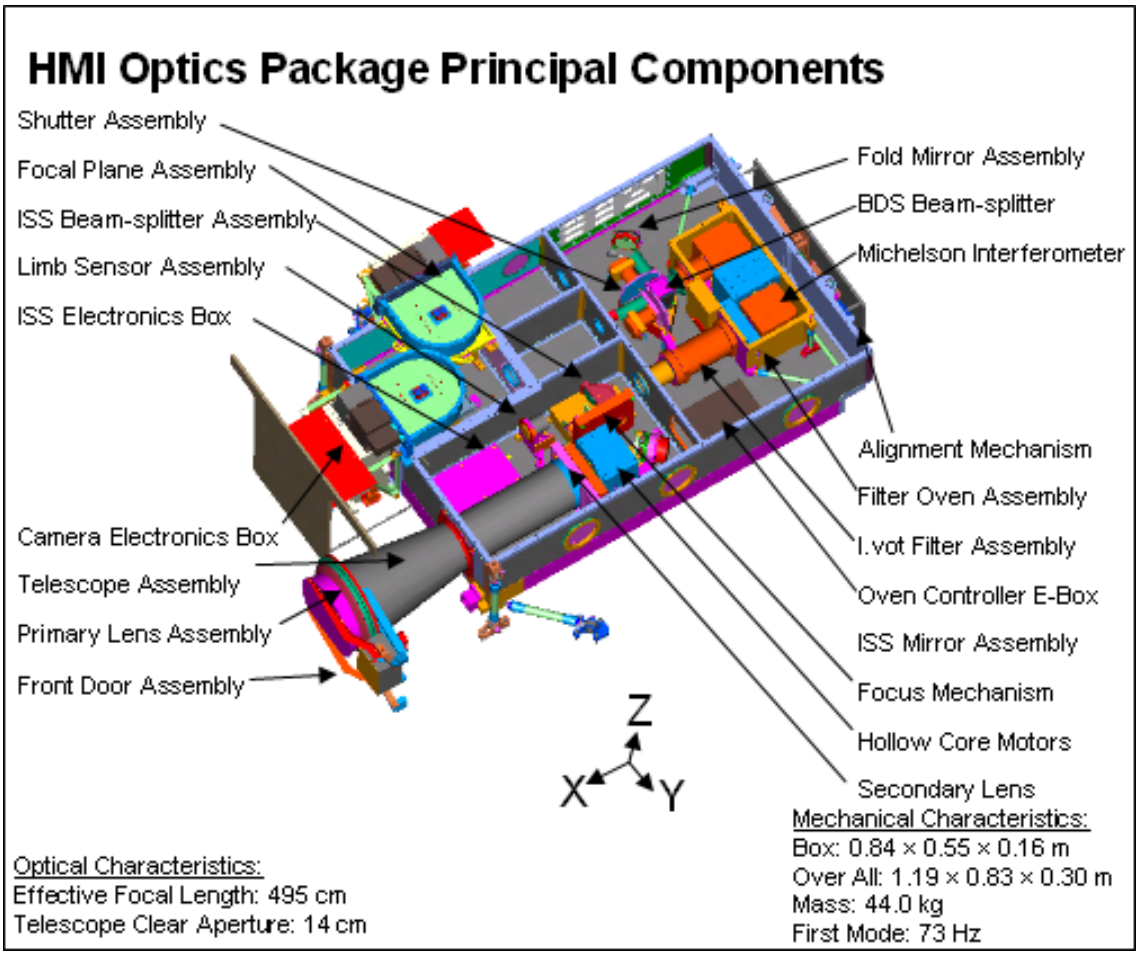

Figure 2.5: Image shows the layout of the HMI instrument.Image from hmi.stanford.edu.

The HMI instrument has three primary science goals:

1. Determining how and why the Sun varies.
2. Improving our understanding of how the Sun drives global change and space weather.
3. To determine how good predictions of space weather and global change can be and to test predictive techniques.

Our work contributes to the second point and relates to the subject of the origin

Central wavelength	6173.3 ± 0.1Å
Field of View	>2000 arcsec
Detector resolution	0.5 ± 0.01 arcsec per pixel
Field of view	6 arcmin × 8.5 arcmin, offset center ± 15 arcmin E -W
Camera image cadence	<4 seconds
LOS magnetogram	
Cadence	45 seconds
Precision	10 G
Dynamic range	± 4 kG

Table 2.3: HMI instrument specifications from hmi.standford.edu

and evolution of sunspots, active regions and complexes of activity and the emergence of magnetic flux and solar transient events.

In table 2.3, we give the specifications for the HMI instrument and the line-of-sight magnetic field measurements.

2.3.3 Atmospheric Imaging Assembly (AIA)

AIA produces full-disk images in ten wavelengths ranging between white light, ultraviolet and extreme ultraviolet at high spatial and temporal resolution. The wavelengths tell us about flaring regions, coronal active regions, the quiet corona, transition regions, the chromosphere and the photosphere. AIA detects plasma at temperatures between 5,000 K to 20 million K. The instrument can provide images every 12 seconds and a spatial resolution of 0.6 arcseconds. The AIA instrument is therefore able to study events on the Sun at high spatial and temporal resolution continuously.

The main science themes for AIA are:

1. How does the Sun's coronal structure affect energy storage, input and release?
2. Why is the corona hotter than the surface?
3. What is the source of radiation and energetic particles in the corona?
4. How do events in the corona affect space near the Earth?
5. What role do waves and oscillations play in the corona (Coronal Seismology)?

The work of this thesis contributes to the first point.

The instrument consists of four Cassegrain telescopes that are optimised for EUV measurements. Each telescope has a 20cm primary mirror and an active secondary mirror which is pointed in response to signals from a dedicated guide telescope (GT). The field of view of each telescope is 41 arcmin × 41 arcmin and typical exposure times are between 0.5 and 3 seconds. The instrument uses a mechanical shutter to change exposure time.

Mirror characteristics	
Primary diameter	20 cm
Focal length	4.125 m
Field of view	41 arcmin × 41 arcmin (along detector axes)
Pixel size (resolution)	0.6 arcsec (1.5 arcsec)
Cadence (all telescopes)	8 wavelengths in 10 to 12 seconds
Typical exposure times	0.5 to 3 seconds

Table 2.4: The main characteristics of the AIA instrument

Channel	Primary ion(s)	region of atmosphere	log(T)
4500 Å	continuum	photosphere	3.7
1700 Å	continuum	temperature min. & photosphere	3.7
304 Å	He II	chromosphere, transition regon	4.7
1600 Å	C IV + cont.	transition region, upper photosphere	5.0
171 Å	Fe IX	quiet corona, upper transition region	5.8
193 Å	Fe XII, XXIV	corona and hot flare plasma	6.2,7.3
211 Å	Fe XIV	active region corona	6.3
335 Å	Fe XVI	active region corona	6.4
94 Å	Fe XVIII	flaring corona	6.8
131 Å	Fe VIII, XXI	transition region, flaring corona	5.6,7.0

Table 2.5: The wavelength channels, primary ions, regions of atmosphere and temperatures observed by AIA

We show the main characteristics of the AIA instrument in table 2.4 and show the various AIA wavelengths, the primary ions, the regions of the atmosphere and the temperatures studied in table 2.5.

Like with EIS, AIA uses different multilayer coatings applied to each half of each telescope to get the desired central wavelength.

2.3.3.1 AIA data processing

In this work we use level 1.5 AIA data. We can download the level 1.0 AIA data from various places including JSOC (Joint Science Operations Center) and the VSO (Virtual Solar Observatory). The level 1.0 data processing involves:

1. Removal of over-scan rows and columns from the CCDs.
2. Removal of a dark image to account for digital offset of the camera, read noise and dark current.
3. Flat-field correction.
4. Correction of "bad" pixels and spikes that result from energetic particles interacting with the CCD or the instrument structure (that are then detected by the CCD).
5. Flipping the AIA image so that solar north is at the top of the array.

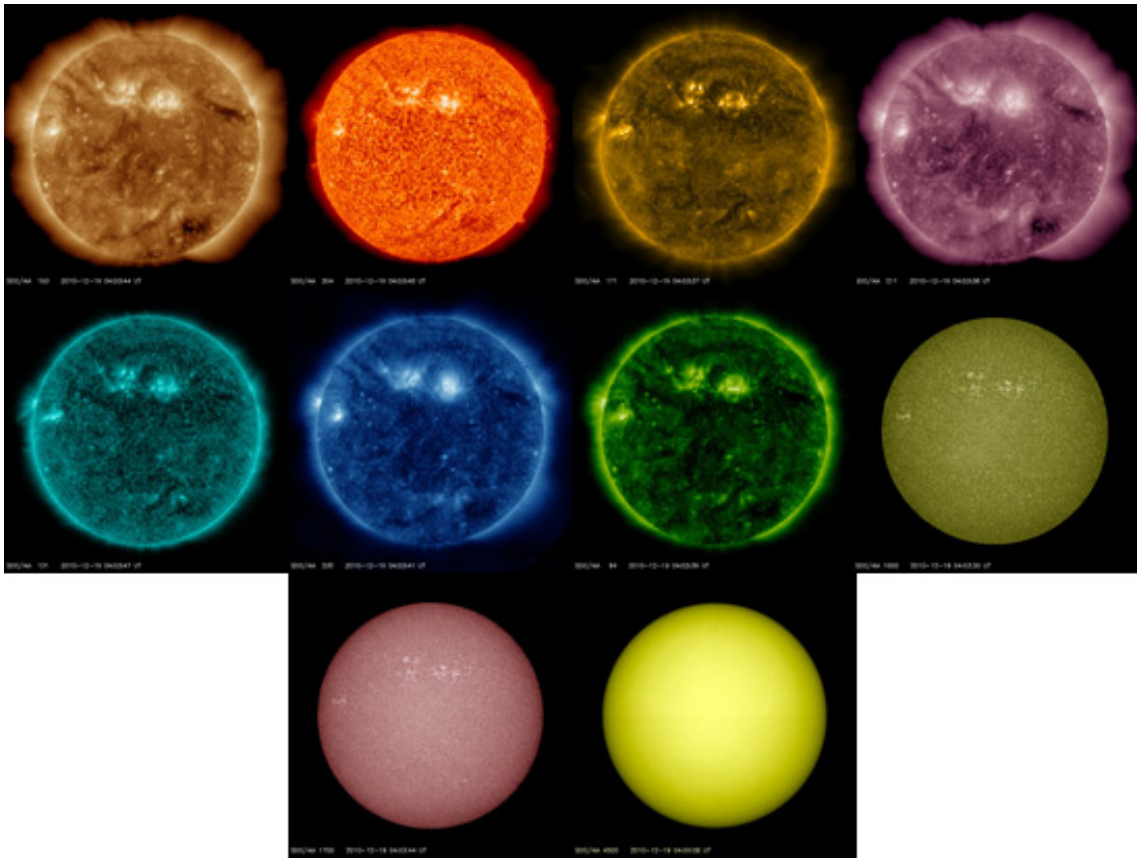

Figure 2.6: Image shows a full disk image of the Sun in each of the AIA wavelength channels.

We then use the solarsoft procedure aia_prep to process the data further to level 1.5. This processing accomplishes three corrections:

1. The AIA data are rotated so that solar North is at 0°. A small roll angle exists between the four telescopes and the spacecraft's star-tracker is used to place solar north at 0°.

2. Plate-scale calibration between the four telescopes. Each telescope has a slightly different focal length which changes the spatial resolution. An adjustment is made to set the image scale to 0.6 arcsec pixel^{-1}.

3. The bore-sight pointing. Before launch, the bore-sight pointing was measured to within 20 arcsec for each telescope. The bore-sights are coaligned by adjusting the secondary-mirror offsets

Chapter 3

The impact of flux emergence into a pre-existing active region

The aims of this thesis are:

1. To investigate the role of emerging flux in generating a response in the atmosphere.

2. To investigate how emerging flux regions with different average flux densities affect the atmosphere when interacting with a pre-existing active region.

3. To investigate any atmospheric response to the emergence of the serpentine field.

We will do this by looking at a large emerging flux region within active region NOAA AR10942 and a small emerging flux region within active region NOAA AR11236 and see how the atmospheric response differs.

In section 3.2, I contributed the analysis of the temporal evolution of the magnetic flux (figure 3.3). The rest of the figures and analysis comes from Harra et al. (2010) and Harra et al. (2012) which were both published in Solar Physics. While I didn't contribute to Harra et al. (2010), I have permission from the authors to use their results. The active region has a coalesced leading polarity with a dispersed following polarity. Section 3.3 is all my own work.

3.1 Introduction

In this study, we look at two emerging flux region complexes and see how emerging flux regions with different flux densities affect the pre-existing active region into which they emerge. One emerging flux region has an average flux density of 490 G and the other has an average flux density of 190 G (see table 3.1). The question we

Active region number	days studied	EFR average flux density (G)	Largest flare released after FE begins
10926	3 days	490	C1.2
11236	2 days	190	-

Table 3.1: Basic information about the two active regions we studied.

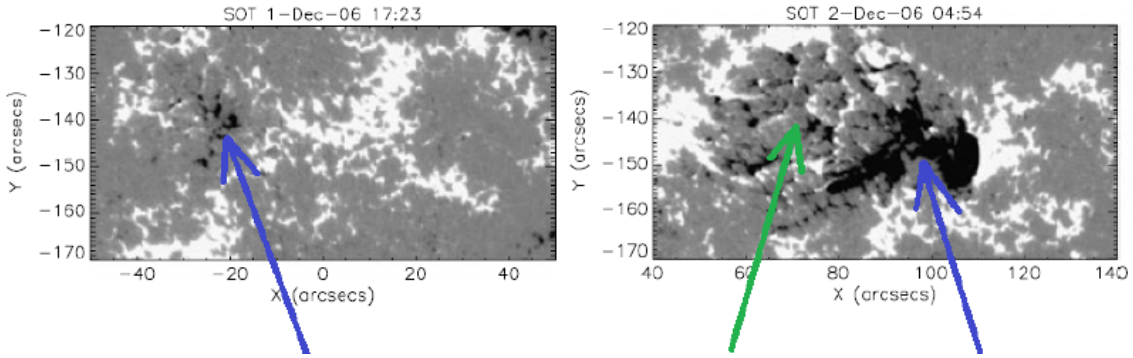

Figure 3.1: Left: Hinode SOT image of an emerging flux region as it begins to form (location of negative flux shown by the blue arrow). Right: Hinode SOT image of the same emerging flux region at a later stage of its evolution (location shown by the blue arrow). The green arrow highlights where the serpentine field forms.

will attempt to answer in this work is, what impact does flux emergence have on a pre-existing active region and the local atmosphere?

Magnetic flux emergence describes the formation of new flux at the solar surface and in the solar atmosphere (such as in fig. 3.1). Magnetic flux emergence can occur anywhere on the solar surface. In many cases, the magnetic flux emerges as a fragmented structure (e.g. Magara and Tsuneta 2008) called the serpentine field (first suggested by Strous et al. 1996). The serpentine field (for the rest of this study this will be referred to as "the serpentine") is seen observationally as small-scale positive and negative bipoles at the early stages of the emergence (fig. 3.1). Figure 1.8 illustrates flux emergence through the different stages. The serpentine field is described by two kinds of loops: Ω loops and U-loops. The Ω-loops are formed by resistive undulatory flux ropes and are able to rise from the convection zone into the photosphere. However, U-loops are not able to rise into the photosphere in the same way as the Ω-loops due to the weight of the plasma on the U-loops. So the only way that the U-loops can fully emerge into the photosphere is by small-scale magnetic reconnection along the serpentine via energy dissipation in electric currents (Pariat et al. 2004). After successive reconnection events, the serpentine field would assume a global Ω-loop configuration. The serpentine field is created by the interaction between the convective downflows and the emerging flux tube (Cheung et al. 2008). The serpentine field can form part of the global active region by successive reconnections occuring between the Ω-loops.

In the chromosphere, small-scale Hα brightenings called Ellerman bombs (EB)(Ellerman 1917) are thought to be an atmospheric response to successive ser-

pentine reconnections (Pariat et al. 2004). The Ellerman bombs have also been shown to heat the transition region (Schmieder et al. 2004). Other observational evidence of the emerging flux region interacting with the existing active regions is in the form of brightenings seen in other chromospheric lines such as He II, that are produced by magnetic reconnection (Guglielmino et al. 2008).

Another response to flux emergence in the chromosphere is the creation of jets formed by magnetic reconnection between the emerging flux region and the pre-existing magnetic structures. These jets have an inverted-Y shape, are several mega-meters in length and have velocities of up to 20 km s^{-1} (Shibata et al. 2007). These appear to be smaller versions of the X-ray jets seen in the corona (Shibata et al. 1992). The X-ray jets have lengths of up to 400 Mm and velocities of up to 300 km s^{-1} (Shibata et al. 1992). These jets are also seen in the extreme ultraviolet in active region/emerging flux region complexes (Gontikakis et al. 2009) with lengths up to 16 Mm and velocities up to 100 km s^{-1} and emerging flux region/polar coronal hole complexes (Kamio et al. 2007) with velocities of 30 km s^{-1}. Like the chromospheric jets, the jets in the corona also follow this inverted-Y shape (Moreno-Insertis et al. 2008). We discuss the creation of chromospheric jets by flux emergence in section 1.4.2.

There are also coronal responses to flux emergence, including the formation of coronal loops, outflows, flares and CMEs. New coronal loops are formed by magnetic reconnection between the magnetic fieldlines of the emerging flux and the pre-existing active region. It has recently been suggested that upflows are a response to magnetic reconnection occurring in the upper chromosphere and the reconnection is maintained by magnetic forces between reconnected loops (Su et al. 2012). As a consequence of the reconnection, particles are accelerated towards the chromosphere and heat the plasma in the chromosphere causing the plasma to rise from the chromosphere up into the corona. In the EIS velocity maps such as the one shown in fig. 3.2, we see the majority of the downflows in the core of the active region and the majority of the upflows at the edges of the active region which is consistent with previous work (e.g. Doschek et al. 2008;Tripathi et al. 2009). The location of the outflows (blue) and downflows (red) are shown in figure 3.2, right. Magnetic reconnection also plays a role in producing flares and coronal mass ejections.

3.2 Response of Active Region coronal dynamics to significant new flux emergence

This section describes the work done by Harra et al. 2010 and the follow-up work in Harra et al. (2012). The emerging flux region has an average flux density (measured at the end of the emergence phase) of 490 G and emerges into active region NOAA AR10926. In Harra et al. (2012), we studied how the flux emergence affects the

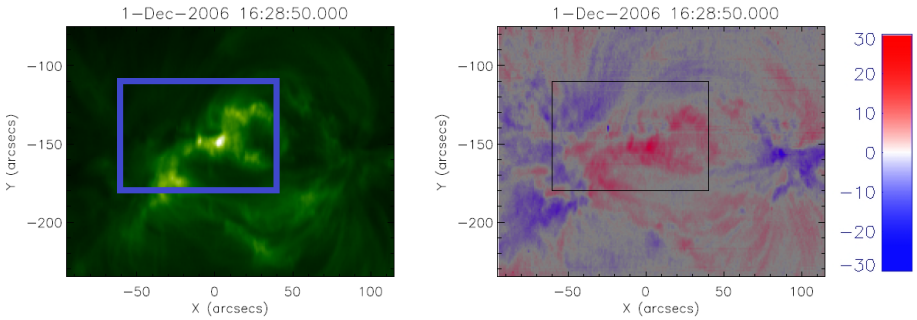

Figure 3.2: EIS intensity (left) and EIS velocity (right) maps of the active region before the new flux emerges. The majority of the upflows (blue) are at the edge of the active region and the majority of the downflows (red) are in between the major polarities of the active region (the active region core). The velocity range is ±30 km s^{-1}. The blue and black boxes show where the new flux will emerge. Images from Harra et al. (2010).

corona and compare the observations with numerical simulations.

3.2.1 Observations

The data used in Harra et al. (2010) and Harra et al. (2012) were taken from the Michelson Doppler Imaging (MDI) instrument on SOlar and Heliospheric Observatory (SOHO), the Solar Optical Telescope (SOT) and the Extreme Ultraviolet Imaging Spectrometer (EIS) on Hinode and the Transition Region And Coronal Explorer (TRACE) 171 Å and 1600 Å wavelength images.

The MDI magnetograms have a cadence of 96 minutes between 00:00 UT on 1 December 2006 to 00:00 UT on 4 December 2006. The SOT data used were Fe I(6302 Å) Stokes V images which were taken by the Narrowband Filter Imager (NFI) with a spatial resolution of 0.16″. The EIS spectral lines used were HeII (256.32 Å), FeXII (195.12 Å) and FeXV (284.16 Å) which cover the temperatures 50,000 K, 1MK and 2MK. The rasters used a 1″ slit and the image cadence varied between 135min and 267min depending on the field of view. The field of view varied between 256″ and 512″ in x and was 256″ in y and the exposure time for each raster is 30s. To create the EIS intensity, Doppler velocity and line width maps, we used a single-gaussian model to fit the data.

The TRACE data coverage started 8 hours after the flux emergence began, but continued after the emergence ends. The TRACE data have a spatial resolution of 1″ and a cadence of approximately three minutes.

3.2.2 Results

3.2.2.1 Description of the active region before flux emergence

The active region AR10926 rotated onto the solar disk in the southern hemisphere on 25 November 2006. Figure 3.3 shows the evolution of the emerging flux region

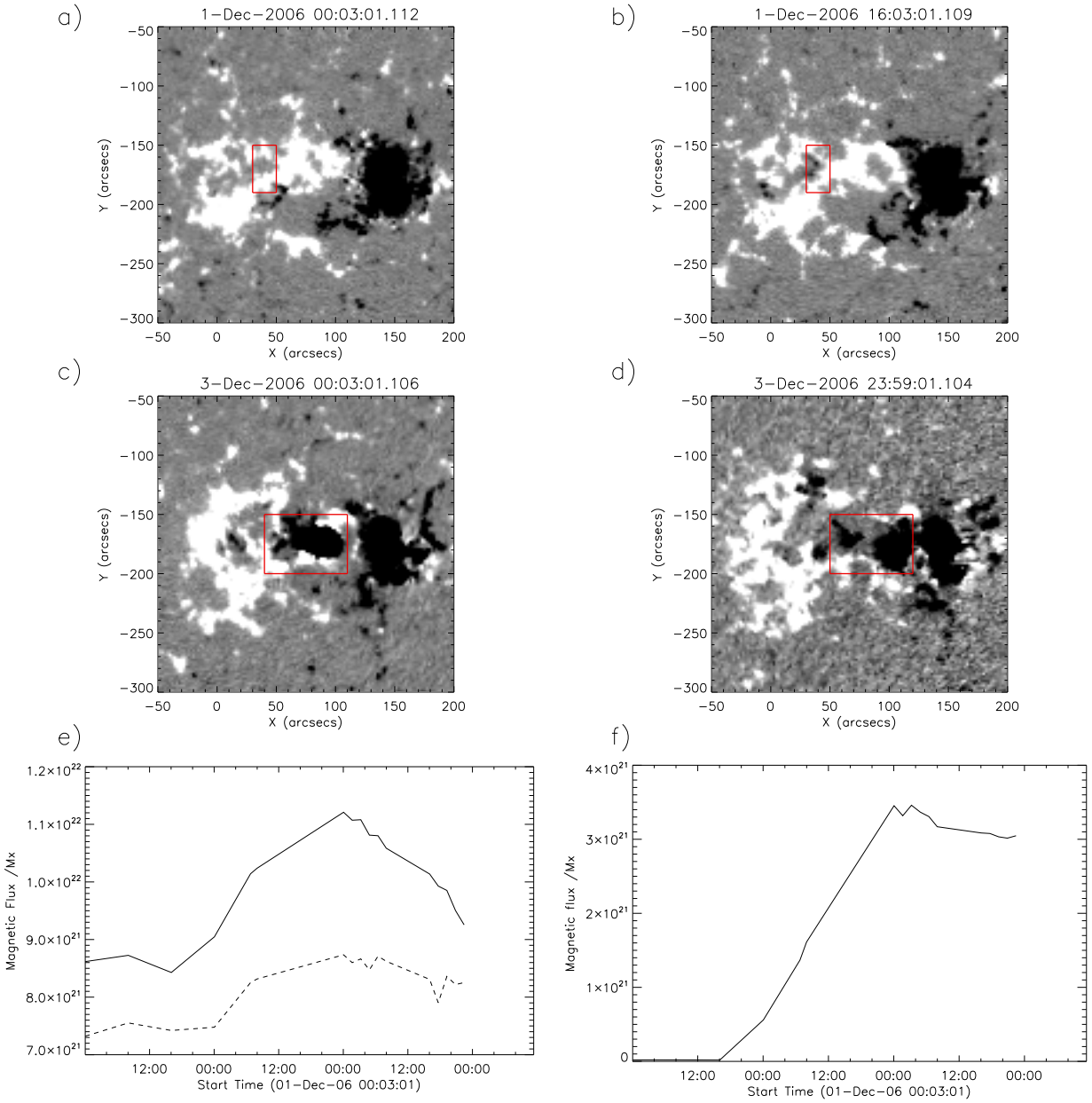

Figure 3.3: (a): Shows the active region before the flux emergence begins. (b) shows the active region and the newly emerged negative polarity (in the red box). (c) and (d) show the emergence and expansion of this new emerging flux region. (e) shows the flux evolution of the active region with the positive flux as a black dotted line and the negative flux as a solid black line. (f) shows the flux evolution of the negative polarity of the emerging flux region. We took a contour around the negative polarity of the flux emergence to make the flux evolution profile.

over three days and the flux evolution of the active region. The total active region flux starts to increase at 16:00 UT on 01 December 2006 and enters a decay phase at 00:00 UT on 03 December 2006 (fig. 3.3e). The flux emergence begins at approximately 16:00 on 01 December 2006 and ends at approximately 00:00 UT on 03 December 2006, the region then enters a decay phase at approximately 06:00 UT on 03 December 2006 (fig. 3.3f). The negative polarity of the active region is the leading polarity and the positive polarity the trailing. The new magnetic flux

emerges in the positive polarity of the active region.

3.2.3 Evolution of the Emerging Flux Region (EFR)

The flux emergence begins at approximately 16:00 UT on 1 December 2006 (fig. 3.3b). The red boxes in fig. 3.3a and b, show where the flux emerges. The red boxes in fig. 3.3c and d show the negative polarity of the flux emergence. The negative polarity of the emerging flux region expands (with an expansion velocity of approximately 1 km s^{-1}) towards the negative polarity of the active region (fig. 3.3c) and starts to coalesce with the active region negative polarity (fig. 3.3 d). The flux emergence phase lasts for 32 hours and then the decay phase begins (fig 3.3f). This rise in flux is clearly shown in the flux evolution of the active region (fig. 3.3e). The flux emerges as a serpentine structure (fig. 3.4,left column).

3.2.3.1 First evidence of chromospheric response to flux emergence

The He II intensity images from EIS show brightenings at the edges of the emerging flux region that persist until the final raster (fig. 3.4, right column). The He II images also show several small-scale loops within the serpentine region which are seen approximately one hour after the flux emergence has begun (the serpentine is highlighted by the blue arrows in figure 3.4, left-hand column). We also see He II brightenings at the edge of the emerging flux region (as shown by the black arrows in figure 3.4, right-hand column).

3.2.3.2 First evidence of coronal response to flux emergence

The TRACE 171 Å (0.16 - 2 MK) images show the formation of new coronal loops caused by the injection of new magnetic flux through the photosphere (fig. 3.5). The EIS Fe XV (2 MK) data show little emission at the early stage of the flux emergence, but show new loops at the same time as the TRACE data. These new loops occur approximately 9 - 12 hours after the flux emergence begins and lie over the emerging flux region (fig. 3.6). At this time however, no small-scale coronal brightenings are seen.

The EIS Fe XII data show weak emission at the early stages of the flux emergence, but with no small-scale enhancements in the intensity near the pre-existing positive polarity (fig. 3.7,left column). However, an enhancement is seen in the Doppler velocity (fig. 3.7,right column, 3rd image) (enhancements of 50 km s^{-1}) and the line width (fig. 3.7,middle column, 3rd image) that was not seen 3 hours before. So there appears to be a release of energy in the corona at the early stages of the flux emergence as shown by the Doppler velocity and line width enhancements which could be related to coronal jets. Approximately five hours after the flux emergence, the loops seen in the Fe XII images are forming along the serpentine region and

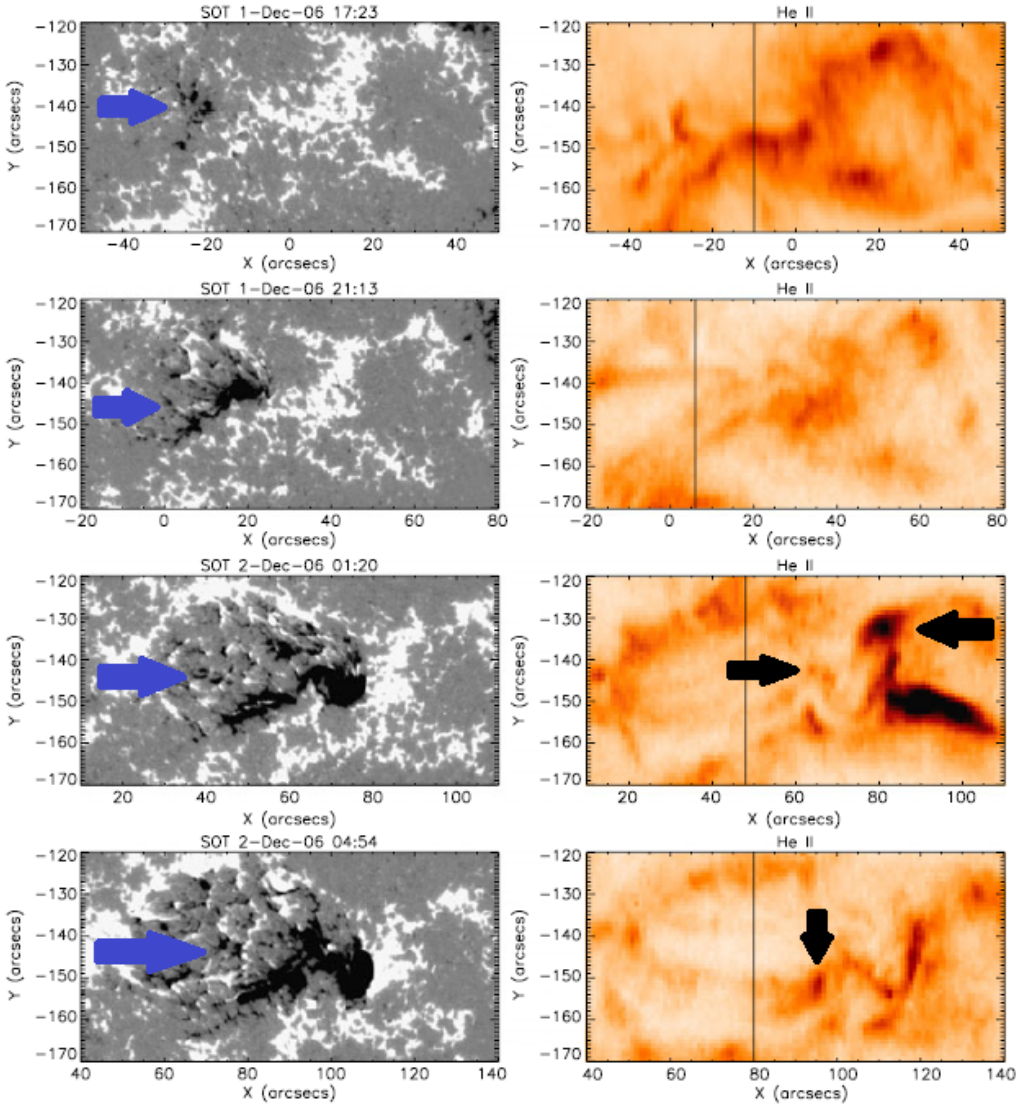

Figure 3.4: Shows the SOT images at different stages of the flux emergence (on the left) and the EIS He II intensity reverse colour images (right column). The vertical line shows the location of the raster at the time of the SOT data. The blue arrows highlight the serpentine and the black arrows highlight the brightenings in He II.

downflows are seen in the same area as these loops. We see new enhancements in line width and Doppler velocities in the Fe XII images. This suggests a release of energy produced by magnetic reconnection between the emerging flux region and the pre-existing active region.

The enhanced outflows seen in EIS on the west side of the emerging flux region are consistent with magnetic reconnection that is seen in the simulations in Harra et al. (2012). The outflows seen on the east side of the emerging flux region are thought to be caused by an increase in pressure caused by multiple parallel fieldlines compressing each other. In figure 3.8, we show a cartoon illustrating the location of the activity observed relative to the magnetic field. Previous work has described the photospheric downflows (Shimizu et al. 2008) and chromospheric brightenings (e.g. Li et al. 2007) and this cartoon adds a description of the coronal response

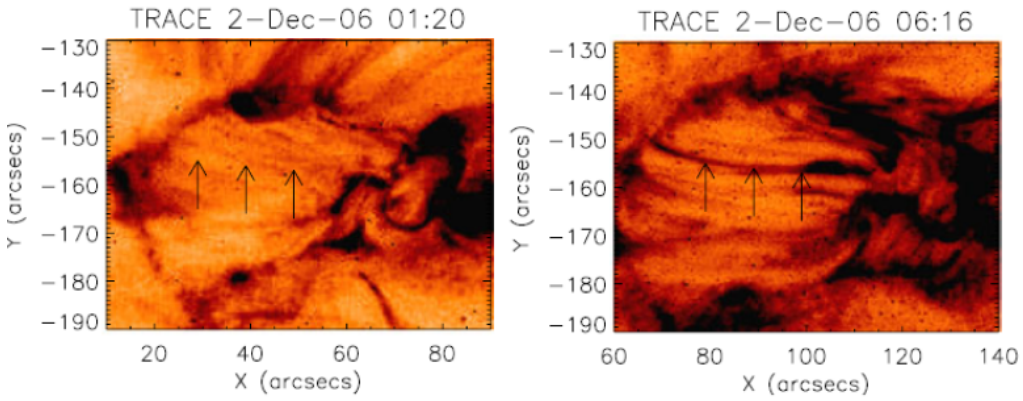

Figure 3.5: TRACE images before and after the flux emergence has begun. The arrows show the location of the serpentine.

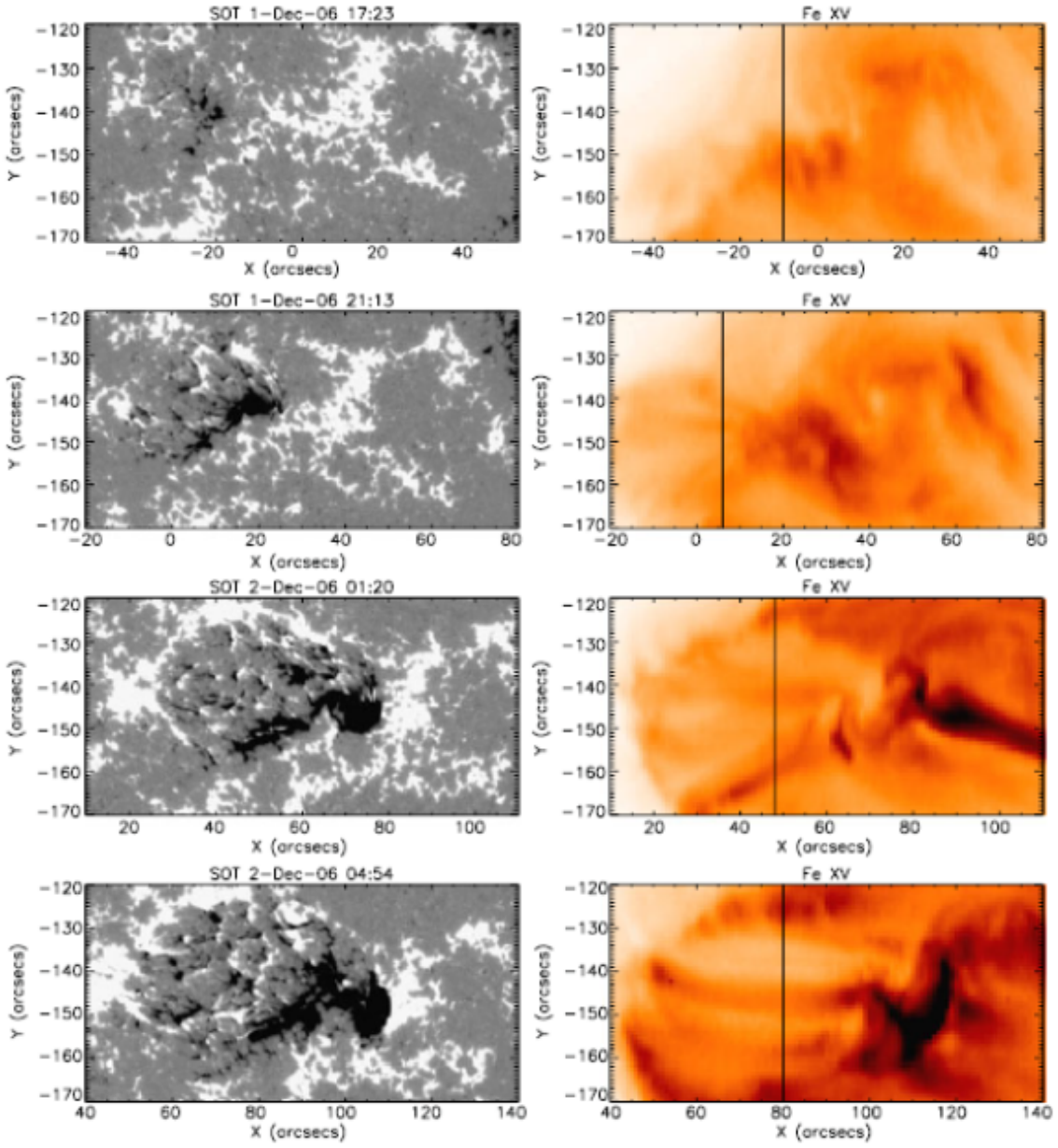

Figure 3.6: EIS Fe XV data at the same time as the SOT data. The black line in the Fe XV data shows the location of the EIS raster at the time of the SOT data.

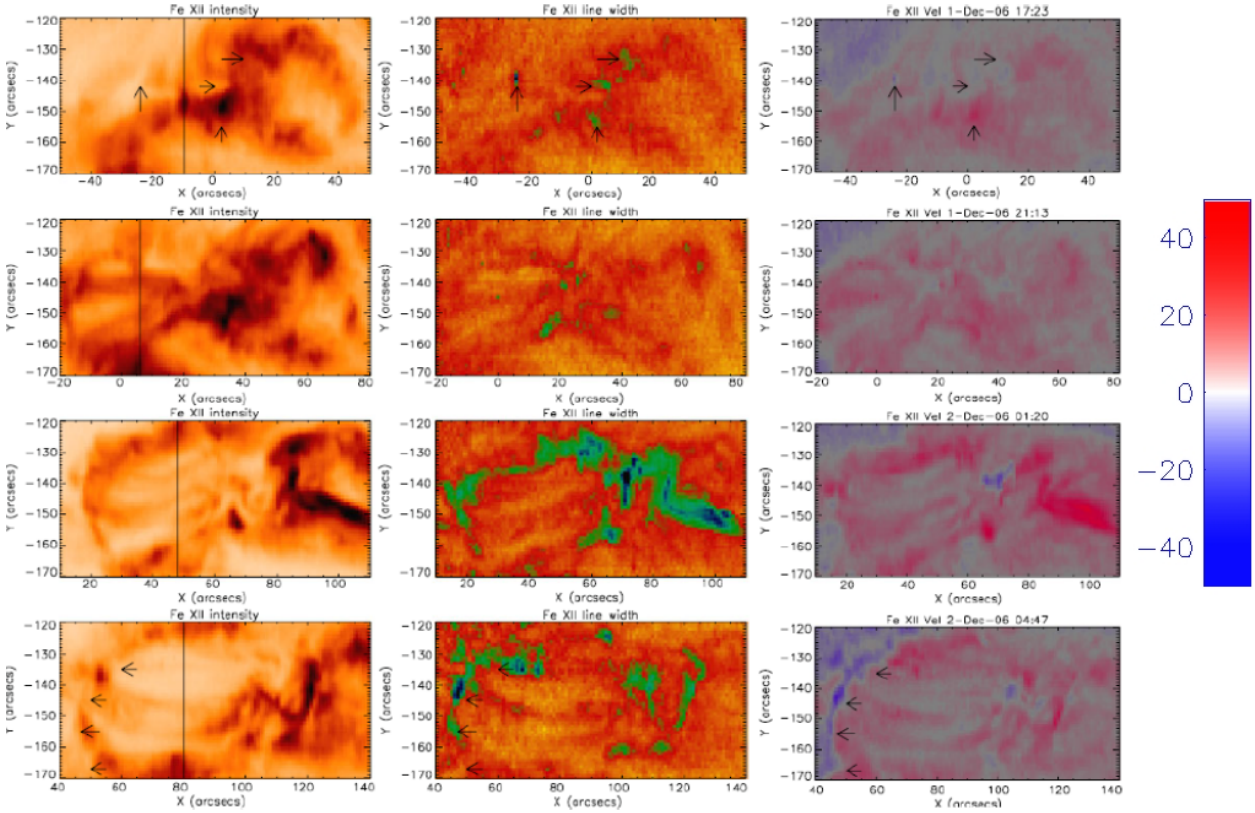

Figure 3.7: Shows the Fe XII intensity (left) and the Fe XII line widths (middle) The black line in the Fe XII data shows the location of the EIS raster. The black arrows in the top images show the location of the line width enhancements. The black arrows in the bottom images show the blue- shifted edge seen in the EIS velocity maps. Right column: Shows the evolution of the flows from the Fe XII Doppler velocity between ± 50 km s^{-1}. The black line in the Fe XII data shows the location of the EIS raster. The black arrows in the top images show the location of the line width enhancements. The black arrows in the bottom images show the blue-shifted edge seen in the EIS velocity map at 04:47 on 2 December 2006 (right column, 4th image).

to emerging magnetic flux from our observations. This cartoon shows that upflows (which are either formed by chromospheric ablation along new loops, compression or outflows along "open" fieldlines) are located at the edge of the flux emergence. These persistent upflows could be related to the outflows that may contribute to the slow solar wind (Sakao et al. 2007; Hara et al. 2008).
We have found the coronal response to this emerging flux region to be:

1. Formation of new loops along the serpentine region is seen 5 hours after the flux emergence.

2. Small scale outflow enhancements (50 km s^{-1}) on the west side of the flux emergence are seen between 5 and 8 hours after the flux emergence begins. The west of the emergence is the favourable site for magnetic reconnection. The closed loops of the flux emergence reconnect with the open-like loops of the pre-existing active region in a process called "interchange reconnection"

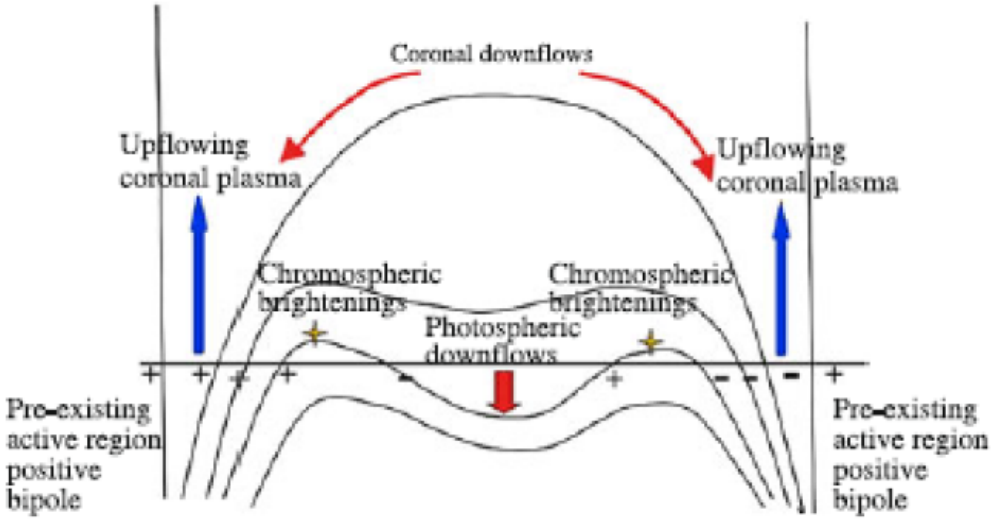

Figure 3.8: Shows the location of the flows and brightenings in an emerging flux region. This cartoon is from Harra et al. 2010.

(e.g. Del Zanna et al. (2011)).

3. Persistent outflow enhancements (50 km s^{-1}) on the east side of the flux emergence are seen between 8 and 12 hours after the flux emergence begins. The east is side of the flux emergence is the favourable site for magnetic field compression.

4. Several small flares (including a C1.2 flare) that start approximately 8 hours after the flux emergence begins.

3.3 Atmospheric response of Active Region to small new flux emergence

This section investigates the atmospheric response to the emergence of new magnetic flux into NOAA active region 11236. In this case, the emerging flux has a relatively low flux density (in comparison to the study presented in section 3.2). The new flux that emerges into active region 11236 has an average flux density of 190 G and the average flux density of the pre-existing active region is 323 G. The flux density measurements were made at the end of the emergence phase to determine the peak value (fig. 3.9c, blue vertical line).

3.3.1 Observations

Active region 11236 is a northern hemisphere region and rotates towards the western limb during the time of this study (between 23 June 2011 to 25 June 2011). The active region has a negative leading polarity which contained a sunspot and a positive

trailing polarity which was fragmented. We used data from the Atmospheric Imaging Assembly (AIA) and Helioseismic and Magnetic Imager (HMI) instruments on the Solar Dynamics Observatory and the EIS instrument on Hinode. The 193 Å , 1600 Å and 304 Å AIA wavelength channels were used at a 12 second cadence, 24 second cadence and 60 second cadence respectively and the 45 second cadence line-of-sight HMI magnetograms were used. The AIA data have a pixel size of 0.6″ and the HMI magnetograms have a pixel size of 0.5″. All datasets were calibrated and co-aligned using the *aia_prep* procedure in Solarsoft. The EIS data have an image time cadence of 5 minutes. The data coverage was 35 minutes per hour and the exposure time for each raster was 9 seconds. There is a gap of 8 hours between 23 June 2011 at 23:00 UT and 24 June 2011 at 07:00 UT when EIS is not pointing at this active region. This EIS study uses a sparse raster with a 2″ slit and 4″ step size. The EIS data were calibrated using *eis_prep* and co-aligned with AIA by comparing features in the EIS 195Å intensity map and AIA 193Å data. We created the EIS intensity and Doppler velocity maps by fitting a single Gaussian curve to the data.

3.3.2 Results

3.3.2.1 Description of the active region before flux emergence

The active region is in decay and loses about 14% of its flux (flux starts at 1.29 $\times 10^{23}$ Mx and falls to 1.11 $\times 10^{23}$ Mx) over the two days we study it (fig. 3.9b). We measured the active region flux by summing within a red contour in figure 3.9a. We see a difference between the amount of positive and negative flux. This is a line-of-sight issue called "area foreshortening" and this occurs when an active region is near the limb (in this case the western limb). The active region had already been on the disk for approximately nine days and produced several flares (C-class and below). It first appears on the far-side of the Sun on 5 June 2011 (as seen by STEREO-B). The yellow vertical line in figure 3.9 represents the start time of the flux emergence and the blue vertical line represents the end of the flux emergence. The flux emergence begins at 09:00 UT on 23 June 2011 in the photosphere and lasts for 15 hours (fig. 3.9c). We measured the negative magnetic flux of the emerging flux region by summing within a contour defined by the blue box in figure 3.9a. As the positive flux of the emergence region is embedded within the positive flux from the pre-existing active region, we only look at the negative flux in the flux emergence region in figure 3.9c. Figure 3.10 shows different stages of the flux emergence:a, before the flux emergence, b, at the start of the flux emergence, c, during the flux emergence and d, at the end of the flux emergence. We use a minimum magnetic field strength of 25 G to remove the quiet Sun magnetic field from our findings. Close et al. (2003) suggest that the quiet Sun magnetic field strength is 20 G. The flux emergence phase starts 09:00 UT on 23 June 2011 and ends at 01:00 UT on 24 June 2011. We also

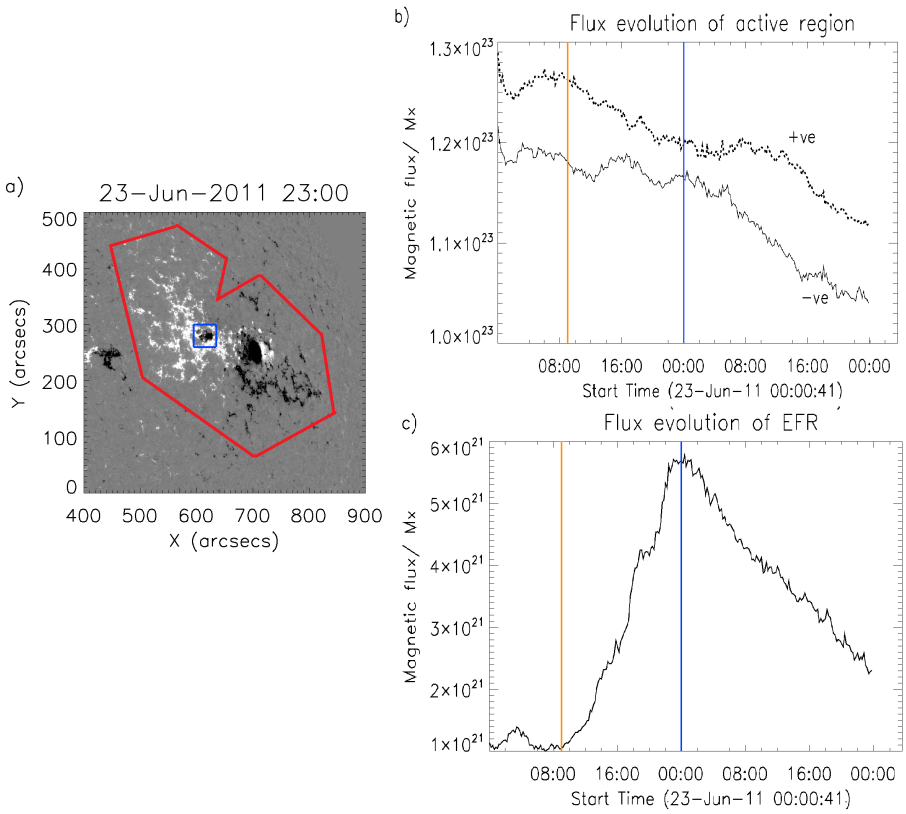

Figure 3.9: (a) Shows the area used to extract the flux evolution curves for the emerging flux region (blue) and the active region (red). We used a minimum magnetic field strength of ±25 G. (b) Shows the flux evolution of the active region, the dashed line is the positive flux and the solid line is the negative flux. (c) Shows the flux evolution of the negative flux in the emerging flux region. The orange and blue lines in both flux evolution plots represent the start of the flux emergence and the peak flux of the emerging flux region respectively.

see a small emergence that lasts for 4 hours between 01:00 UT and 03:00 UT on 23 June 2011. This then decays over the next two hours before disappearing from the magnetograms (fig. 3.9c). We use a box to measure the flux evolution to cover all the unsigned negative flux in the emerging flux region. The magnetic flux densities were measured by extracting a contour region around the negative polarities of the active regions and the emerging flux regions. We also rebinned the HMI data to match the resolution of the MDI data (section 3.2). This was to make our results consistent and independent of spatial resolution. If we had not done this, the flux density in the second example would be higher as HMI has the ability to resolve and average smaller features, where MDI (in section 3.2) cannot measure these smaller features accurately.

3.3.2.2 Atmospheric response to flux emergence

In this section we look at how flux emergence is related to the events seen in the atmosphere on 23 June 2011. We use the 1600 Å channel, the 304 Å channel and

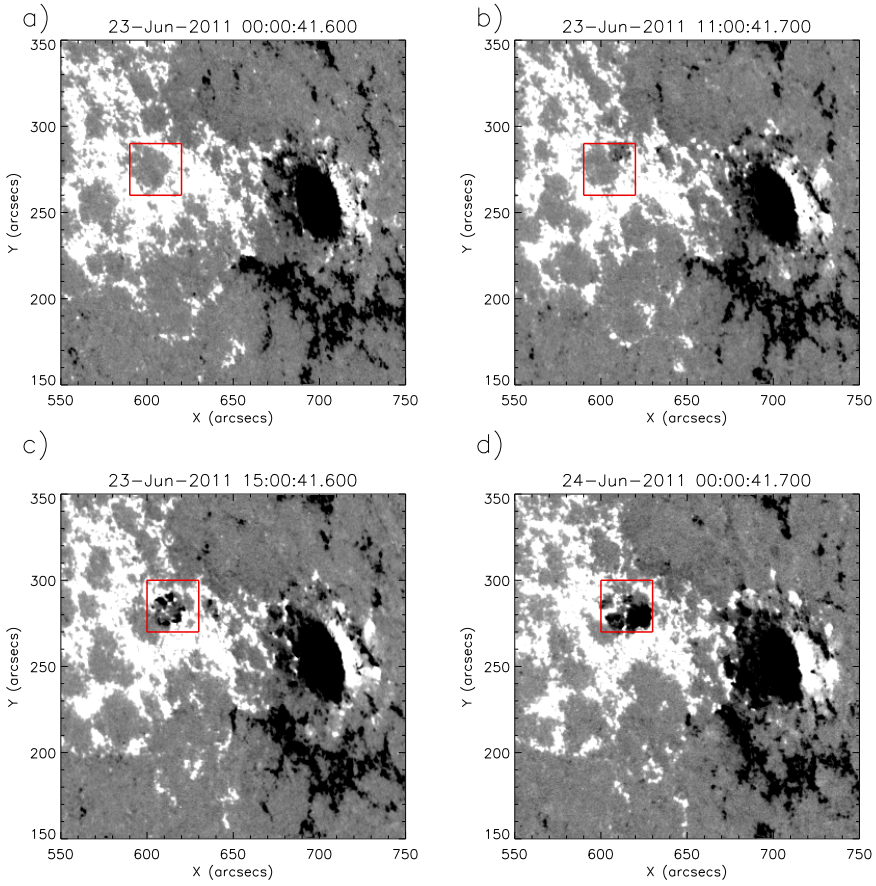

Figure 3.10: The HMI magnetogram images show the changes seen in the active region before (a) and at different stages of the flux emergence (b, c and d). The red box shows where the new negative flux emerges.

the 193 Å channel from the AIA instrument to look for local intensity enhancements (brightenings) in the upper photosphere (5000 K), upper chromosphere (50,000 K) and the 1.25 MK corona and compare these brightenings to changes in the magnetic field. Brightenings are thought to be associated with magnetic reconnection (e.g. Guglielmino et al. 2010). We also use 304 Å and 193 Å to look for EUV jets and where they are located with respect to the emerging flux region. We use 193 Å to look for any atmospheric response to the magnetic flux emergence away from the emerging flux region and we use EIS Fe XII intensity and Doppler velocity maps to look for any upflow or downflow enhancements near the location of the flux emergence. If magnetic reconnection does drive the emergence of the serpentine field into the atmosphere, we should see some evidence for this in the form of brightenings, jets, new loops and upflow/downflow enhancements.

3.3.2.2.1 The early stages of the flux emergence

In this section, we look at the early stages of the flux emergence and how the atmosphere responds to the newly injected magnetic flux. We define the early stages

of the flux emergence to be when the serpentine field is emerging.

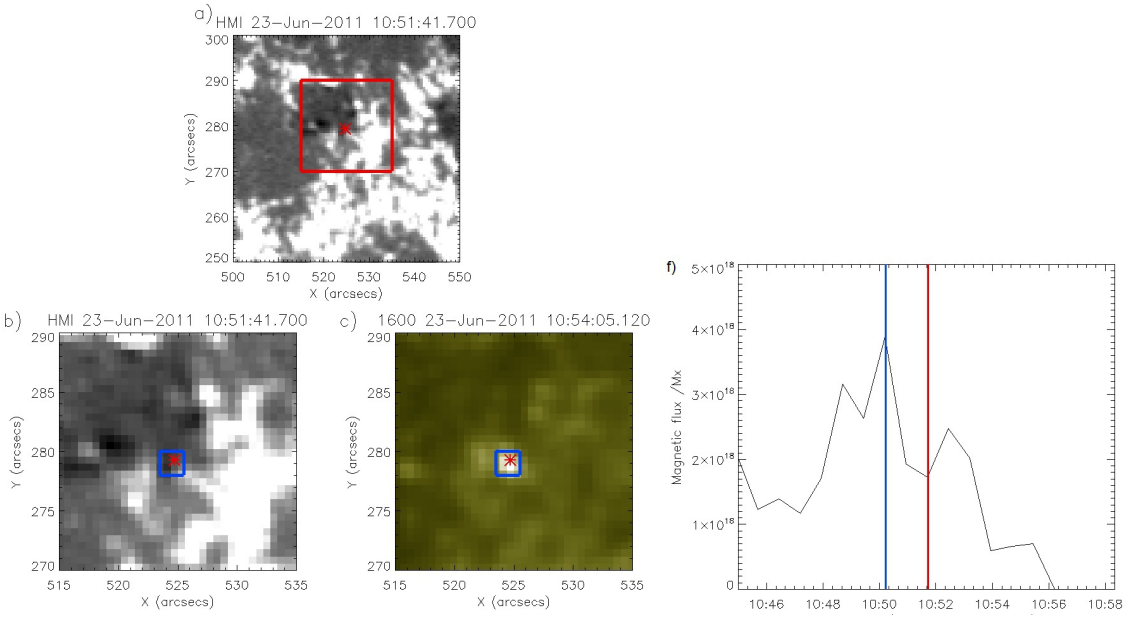

Figure 3.11: Images from HMI (a,b) and the 1600 Å channel (c) on AIA when the brightening occurs in the 1600 Å channel. The red star represents the location of the brightening in the 1600 Å channel. The red box in (a) shows the field of view of (b) and (c). The blue box shows the extraction region for the flux cancellation measurement. The flux evolution profile for the negative polarity (d) was measured from the blue box in a,b and c. The blue vertical line shows the start of the flux cancellation and the red vertical line shows the end of the flux cancellation.

The first brightening we see in the 1600 Å (5000 K) occurs at 10:54 UT on 23 June 2011 (fig. 3.11c). We attribute this brightening to a flux cancellation event occuring on the Sun as observed by HMI. At this location we see a small area of negative magnetic flux between two positive polarities (fig. 3.11b). We measure the magnetic flux (associated with the negative polarity) around the brightening location and we measure a flux decrease of 2.2×10^{18} Mx between 10:51.41 UT and 10:53.11 UT on 23 June 2011. This is a similar to the amount of magnetic flux cancellation found in sunspot moats by Bellot Rubio and Beck (2005) who saw brightenings in the chromosphere and corona as a response to this magnetic flux cancellation. The brightening lasts for approximately 3 minutes and has a maximum area of 760,000 km^2.

The first brightening seen in 1600 Å was six times brighter than the background. We therefore define the minimum intensity of a brightening to be six times the brightness of the background and we can use this intensity level to define contours to measure the area of the brightenings in 1600 Å 304 Å and 193 Å . Brightenings occur at the edge of the magnetic flux emergence and also where the serpentine field forms in the magnetic flux emergence . One example of brightenings at the edge of the magnetic flux emergence is at 13:51 UT (fig. 3.12a). We see this brightening in 1600 Å (upper photosphere), in 304 Å (upper chromosphere) and 193 Å (corona at

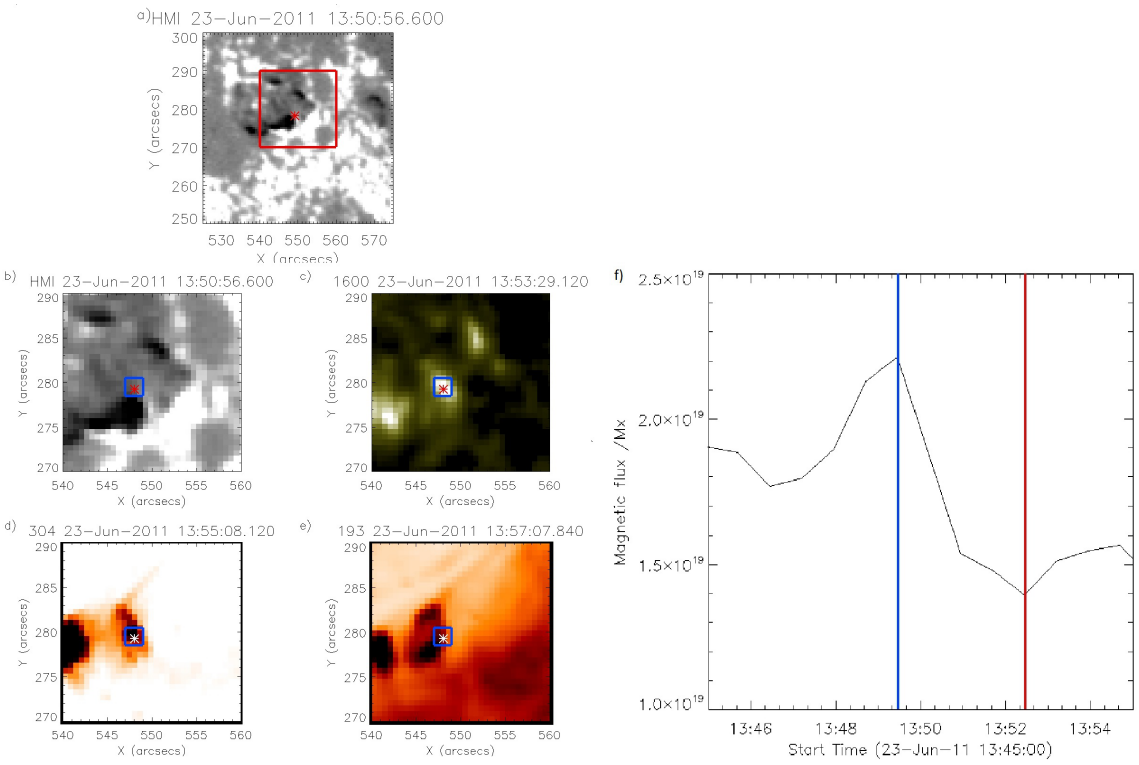

Figure 3.12: Images from HMI (a,b) and in 1600 Å (c) , 304Å (d) and 193 Å (e) channels when a brightening occurs at the edge of the magnetic flux emergence region. The 193 Å and 304 Å images are shown in a reverse colour table. The red (white in d and e) star represents the location of the brightening in the 1600 Å channel. The red box in image (a) shows the field of view of images (b) to (e). The blue box shows the extraction region for the magnetic flux cancellation measurement. The flux evolution profile of the negative polarity (f) was measured from the blue box in b, c, d and e. The blue vertical line shows the start of the flux cancellation and the red vertical line shows the end of the flux cancellation.

1.25 MK). We see this brightening at 13:53 UT (fig. 3.12c), 13:55 UT (fig. 3.12d) and 13:57 UT (fig. 3.12e) respectively. This brightening is associated with magnetic flux cancellation between the major negative polarity and the positive polarity of a small emerging bipole that occurs at 13:49 (fig. 3.12b). The magnetic flux (associated with the positive polarity) around the brightening location decreases by 8.2×10^{18} Mx between 13:49.28 UT and 13:52.27 UT on 23 June 2011. The brightening in 1600 Å lasts for 4 minutes and has an area of 1.1 million km^2, the brightening in 304 Å lasts for approximately 4 minutes and has an area of 1.7 million km^2, while the brightening seen in 193 Å lasts for approximately 3 minutes and is 1.9 million km^2 in area. These brightenings are much larger than the brightening seen in figure 3.11.

The first chromospheric jets are seen in the AIA 304 Å wavelength approximately five hours after the flux emergence begins (fig. 3.13). The chromospheric jet velocities range between 20 and 30 km s^{-1} and the lengths range between 5 Mm and 10 Mm for the period of time jets are seen (approximately 7 hours). We measured the jet velocity and length by measuring the propagation of the plasma. We see the

chromospheric jets over the serpentine field.

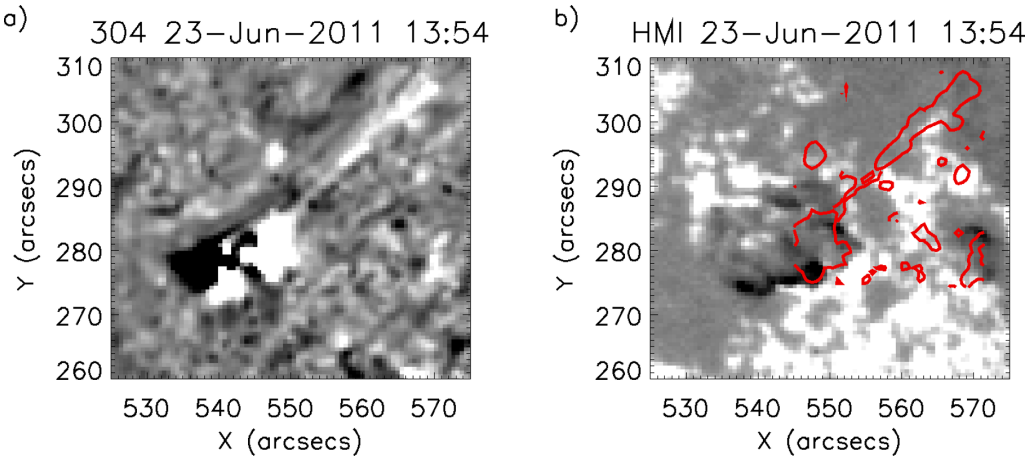

Figure 3.13: The first jet seen in the chromosphere (304 Å) five hours after the flux emergence begins. Left: A base difference AIA intensity map of the jet between 13:48 and 13:54 on 23 June 2011. Right: The closest HMI image to when the jet is released. The red contours show location of the jet seen in 304 Å difference image. This jet lasts for approximately six minutes.

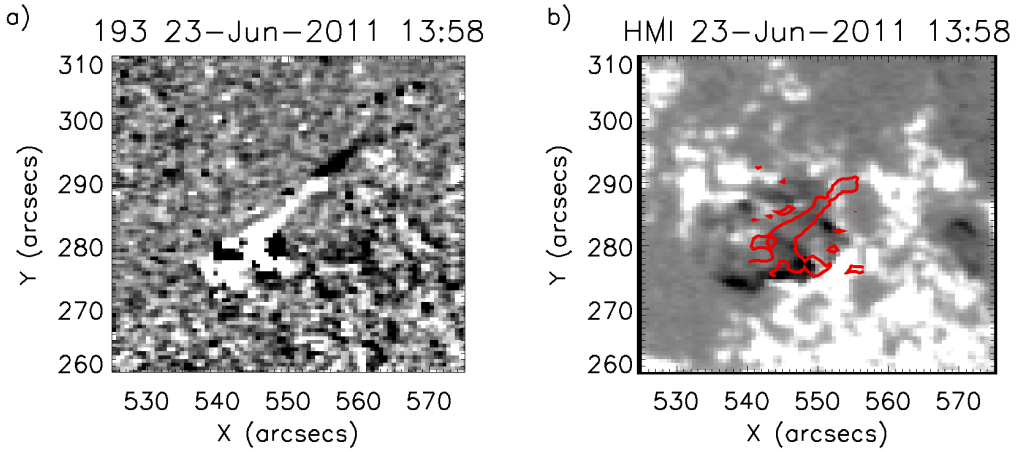

Figure 3.14: Example of a jet seen over the serpentine field in 193 Å (b). The red contours show the jet seen in the AIA 193 Å difference image (a).

The first coronal (in 193 Å wavelength) jets are seen approximately five minutes after the first chromospheric jets. There are no coronal jets seen over this region before the flux emergence and they are only seen approximately 5 hours after the flux emergence has begun. At the early stages of the formation (for example, figure 3.14a), these jets have a velocity of approximately 50-60 km s^{-1} with lengths between approximately 10 Mm and 13 Mm . They are spatially located over the region of magnetic flux emergence with the footpoints appearing to be in the serpentine field rather than at the major polarities of the emerging flux region. The coronal jets are seen several minutes after the chromospheric jets and are seen at the same location.

We also see a connection between the location of the brightenings and the location of one of the jet's footpoints. We show a brightening in the 1600 Å channel that is

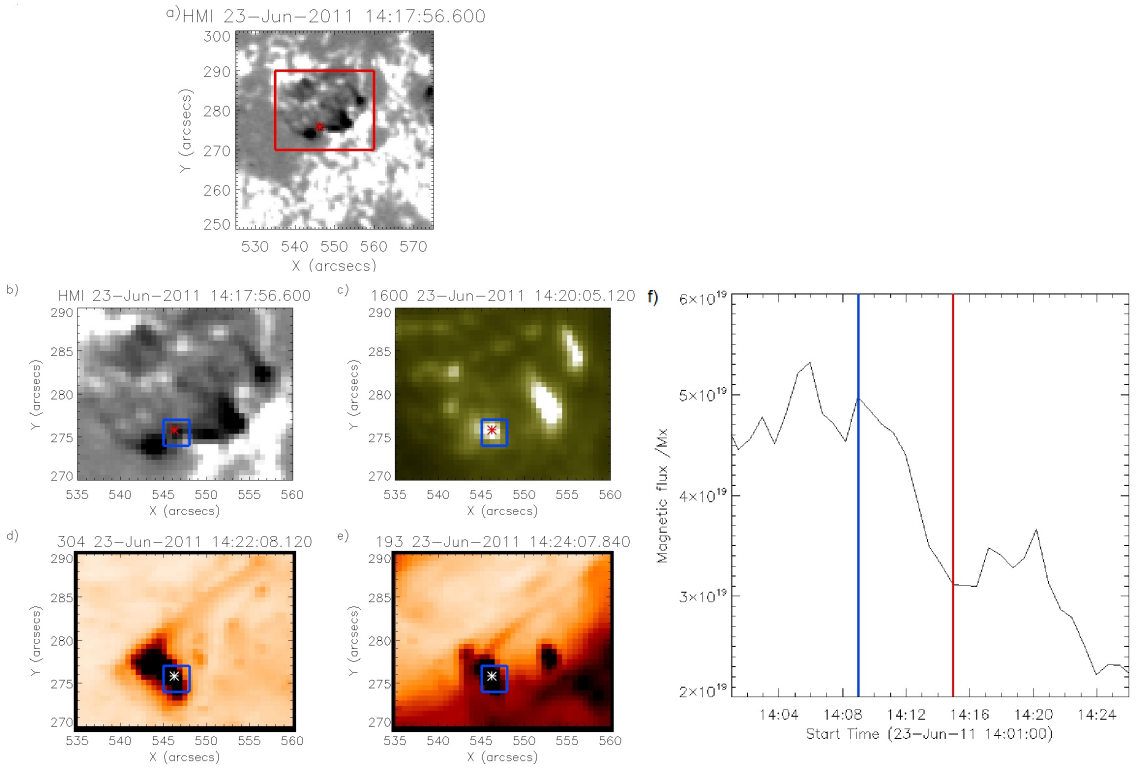

Figure 3.15: Images from HMI (a,b) and in 1600 Å (c), 304Å (d) and 193 Å (e) channels when a brightening occurs at the same time chromospheric and coronal jets are formed over the serpentine at approximately 14:15. The 193 Å and 304 Å images are shown in a reverse colour table. The red (white in d and e) star represents the location of the brightening in the 1600 Å channel. The red box in image (a) shows the field of view of images (b) to (e). The blue box shows the extraction region for the flux cancellation measurement. The flux evolution profile for the positive polarity (f) was measured from the blue box in b, c, d and e. The blue vertical line shows the start of the flux cancellation and the red vertical line shows the end of the flux cancellation.

connected to jets seen in the 304 Å and 193 Å channel. The first example connects brightenings to jets over the serpentine at 14:18 UT in HMI (fig. 3.15a), in 1600 Å at 14:20 UT (fig. 3.15c), in 304 Å at 14:22 UT (fig. 3.15d) and in 193 Å at 14:26 UT (fig. 3.15e). The brightening is associated with flux cancellation between a very small bipole and a larger negative polarity (fig. 3.15b). The magnetic flux (associated with the positive polarity) around the brightening location decreases by 1.9×10^{19} Mx between 14:17.56 UT and 14:20.05 UT on 23 June. The brightening lasts for 8 minutes and has an area of 1.6 million km^2. The jets in 304 Å and 193 Å last for approximately 5 minutes and are 7.9 Mm and 6.1 Mm in length respectively. This 1600 Å brightening is larger than the 1600 Å brightening seen at approximately 13:50.

We also see brightenings in the serpentine field at a later phase of the serpentine's emergence. We show two examples of these brightenings: one that reaches the upper chromosphere, but not the corona and the second that reaches the corona. The first serpentine example occurs at 16:24 UT in HMI (fig. 3.16a) and is detected in 1600 Å

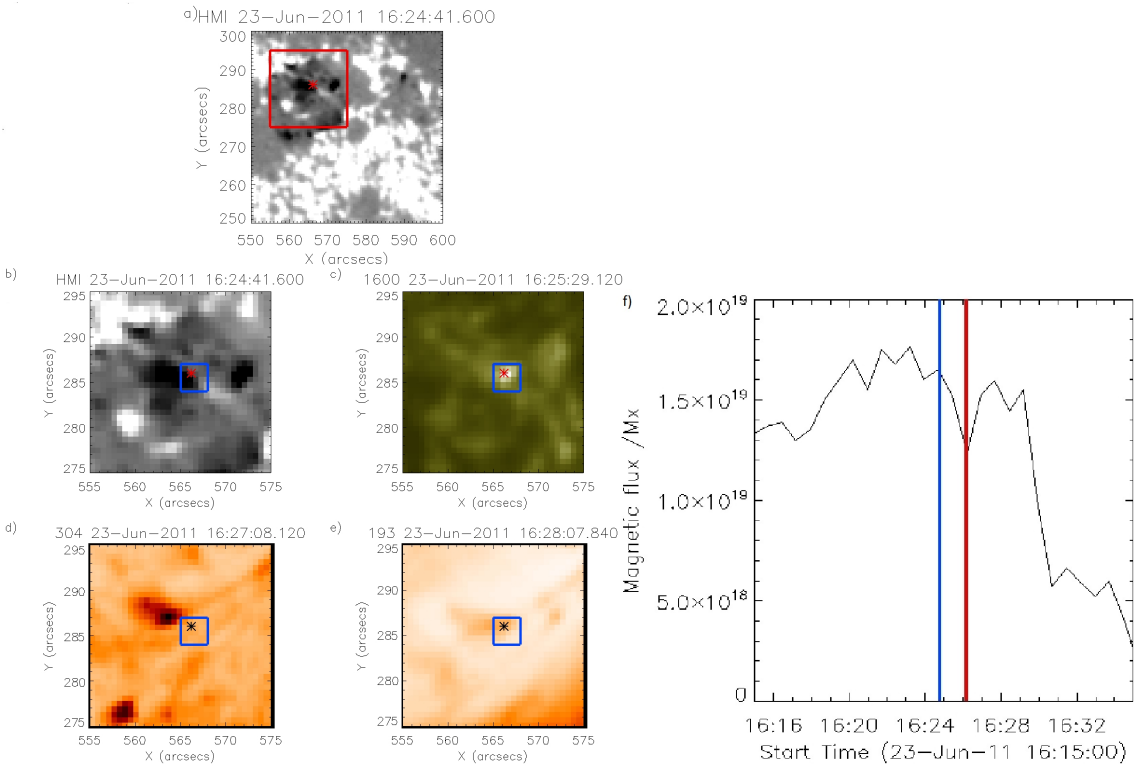

Figure 3.16: shows images from HMI (a,b) and in 1600 Å (c), 304Å (d) and 193 Å (e) channels when a brightening occurs in the serpentine field at approximately 16:25. The 193 Å and 304 Å images are shown in a reverse colour table. The red (black in d and e) star represents the location of the brightening in the 1600 Å channel. The red box in image (a) shows the field of view of images (b) to (e). We do not see a brightening in the 193 Å channel. The blue box shows the extraction region for the flux cancellation measurement. The flux evolution profile for the positive polarity (f) was measured from the blue box in b, c, d and e. The blue vertical line shows the start of the flux cancellation and the red vertical line shows the end of the flux cancellation.

at 16:25 UT (fig. 3.16c), in 304 Å at 16:27 UT (fig. 3.16d) and we see no brightening in the 193 Å channel (fig. 3.16e). This brightening is attributed to magnetic flux cancellation occuring between a very small positive polarity sandwiched between two larger negative polarities (fig. 3.16b). The magnetic flux (associated with the positive polarity) around the brightening location decreases by 4.2×10^{18} Mx between 16:24.46 and 16:26.14 on 23 June. The brightening in 1600 Å lasts for 5 minutes and is 1.1 million km^2 in area, while the brightening in 304 Å lasts for 4 minutes and is 1.1 million km^2 in area. These brightenings are smaller than majority of the brightenings at earlier stages of the flux emergence. There is another, larger event that occurs 6 minutes later. This is associated with a brightening that reaches the corona.

The second serpentine example occurs at 16:46 in HMI (fig. 3.17a) and is detected in 1600 Å at 16:48 (fig. 3.17d), in 304 Å at 16:52 UT (fig. 3.17e) and in 193 Å at 16:53 UT (fig. 3.17f). This brightening is attributed to magnetic flux cancellation occuring between a very small amount of negative flux moving towards

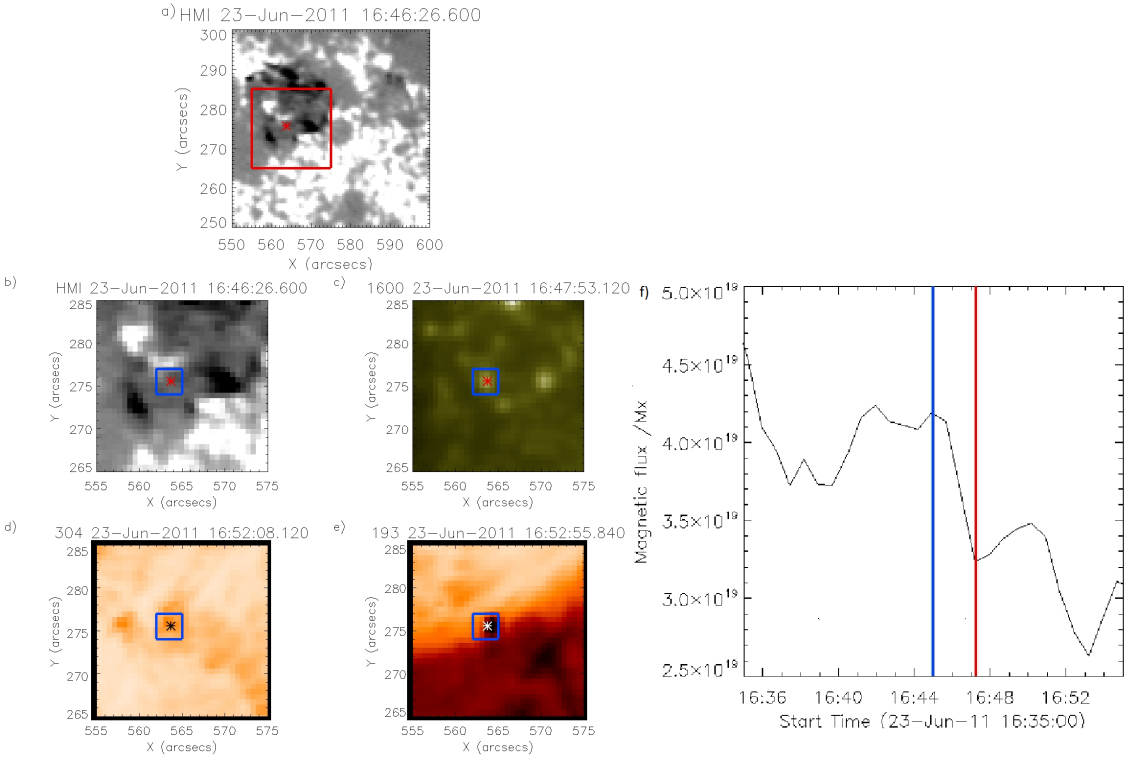

Figure 3.17: shows images from HMI (a,b) and in 1600 Å (c), 304Å (d) and 193 Å (e) channels when a brightening occurs in the serpentine field at approximately 16:45. The 193 Å and 304 Å images are shown in a reverse colour table. The red (black in d and white in e) star represents the location of the brightening in the 1600 Å channel. The red box in image (a) shows the field of view of images (b) to (e). The blue box shows the extraction region for the flux cancellation measurement. The flux evolution profile for the negative polarity (f) was measured from the blue box in b, c, d and e. The blue vertical line shows the start of the flux cancellation and the red vertical line shows the end of the flux cancellation.

the positive polarity above and then disappearing (fig. 3.17b). The magnetic flux (associated with the negative polarity) around the brightening location decreases by 9.1×10^{18} Mx between 16:44.58 UT and 16:47.15 UT on 23 June. The brightening lasts for 2 minutes in all three wavelengths and has an area of 1.3 million km^2 for all three wavelengths. This is larger than the brightenings seen in figure 3.16 and may explain why this event reaches the corona and the brightenings in figure 3.17.

3.3.2.2.2 The evolution of the flux emergence after 17:00 on 23 June 2011

In this section, we look at the later stages of the magnetic flux emergence and how the atmosphere responds as the emerging flux region develops. We define the later stages of the flux emergence to be after the serpentine field is no longer observed (this occurs between 16:45 UT and 17:10 UT on 23 June 2011) to the end of the emergence.

At this stage of the jet formation, the footpoints of the jets appear to be over the

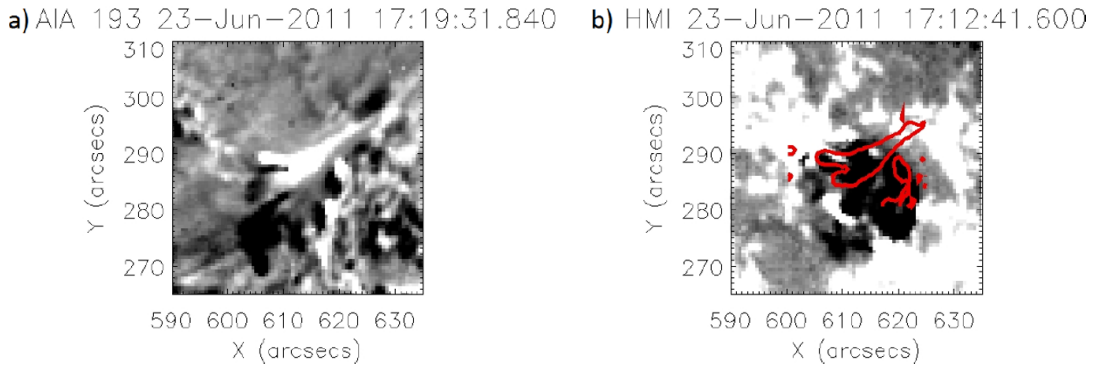

Figure 3.18: Shows an example of a jet seen over the main flux emergence field (b). The red contours show the jets seen in the AIA 193 Å difference image (a).

major polarities of the flux emergence (for example, figure 3.18b). The length and velocity of the jets at the later stages of the flux emergence increase to approximately 16 Mm and approximately 70 km s^{-1}.

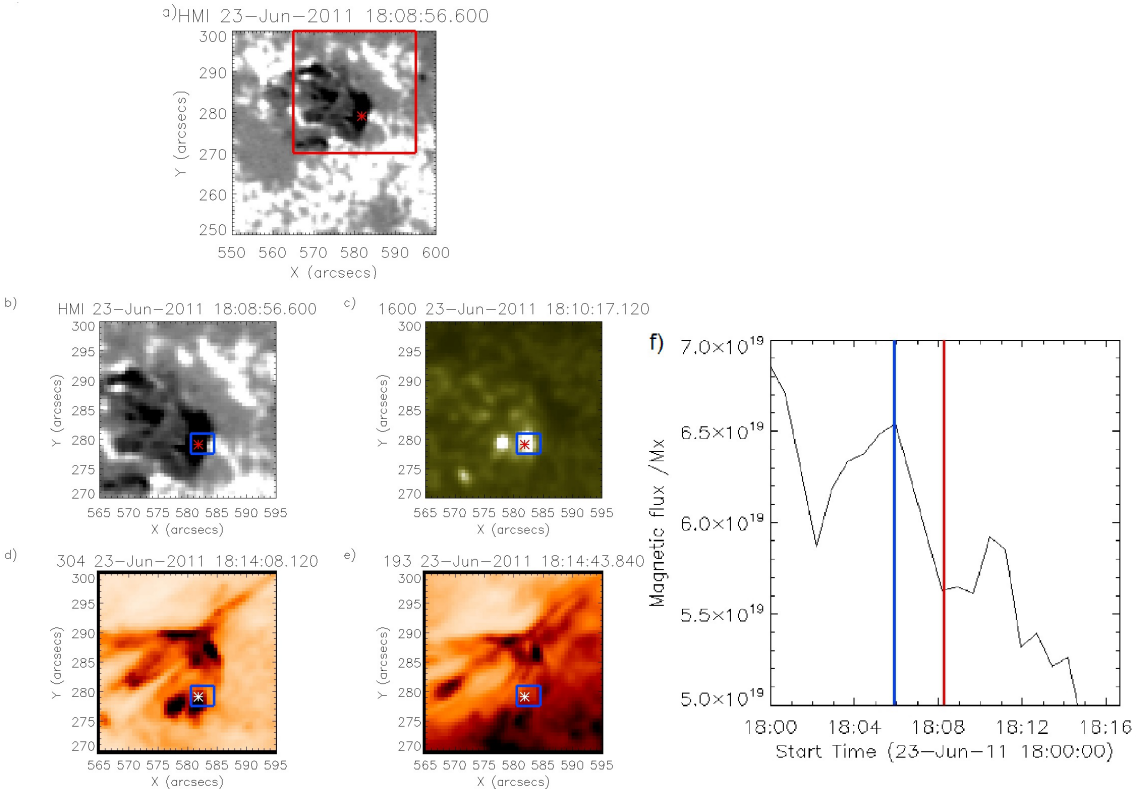

Figure 3.19: shows images from HMI (a,b) and in 1600 Å (c) , 304Å (d) and 193 Å (e) channels when a brightening occurs at the same time chromospheric and coronal jets are formed over the large-scale EFR field at approximately 18:15. The red (white in d and e) star represents the location of the brightening in the 1600 Å channel. The red box in image (a) shows the field of view of images (b) to (e). The 193 Å and 304 Å images are shown with a reverse colour table. The blue box shows the extraction region for the flux cancellation measurement. The flux evolution profile for the positive polarity (f) was measured from the blue box in b, c, d and e. The blue vertical line shows the start of the flux cancellation and the red vertical line shows the end of the flux cancellation.

The next example connects brightenings to jets over the larger EFR field at 18:08 UT in HMI (fig. 3.19a), in 1600 Å at 18:10 UT (fig. 3.19c), in 304 Å at 18:14 UT (fig. 3.19d) and in 193 Å at 18:15 UT (fig. 3.19e). The brightening is associated with magnetic flux cancellation between the major negative polarity of the flux emergence and the pre-existing positive polarity of the active region (fig. 3.19b). The unsigned magnetic flux (associated with the positive polarity) around the brightening location decreases by 9.9×10^{18} Mx between 18:05.54 UT and 18:08.16 UT on 23 June. The brightening seen in 1600 Å lasts for 6 minutes and has an area of 1.9 million km^2. The jets seen in 304 Å and 193 Å last for approximately 7 - 10 minutes and are 10.0 Mm and 9.2 Mm in length respectively. This is the largest brightening we see during the flux emergence.

3.3.2.2.3 How does the atmosphere respond to the flux emergence change?

Up until now, we have concentrated on the atmospheric response to new flux as it interacts with the positive polarity of the pre-existing active region to the south of the emerging flux region. But do we see any atmospheric response to the north of the emerging flux region, and if so, how far away does the emerging flux region's influence extend?

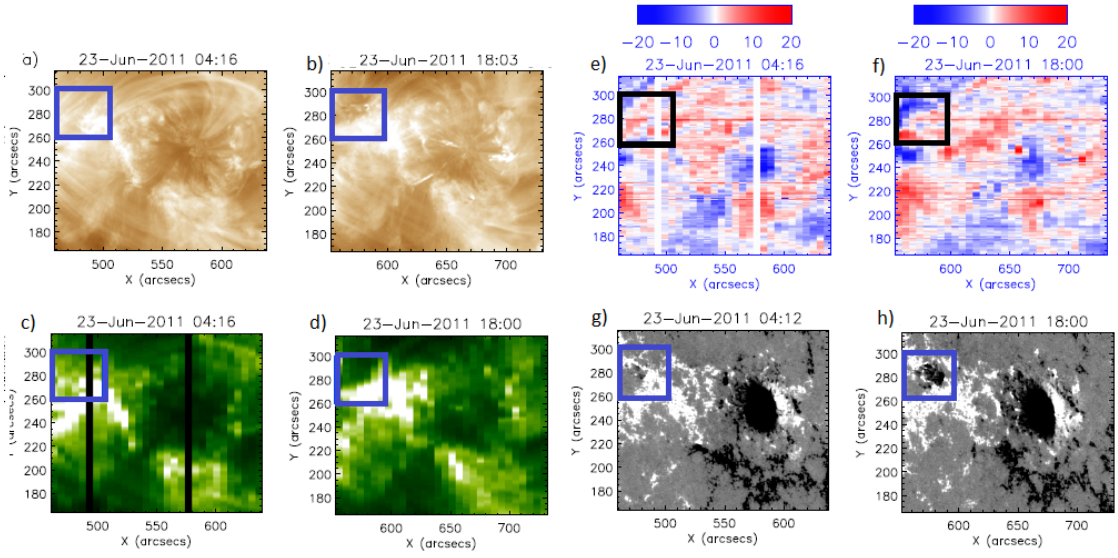

Figure 3.20: (a) & (b): Shows AIA 193 Å intensity maps before (5 hours) and after (9 hours) the flux emergence begins. (c) & (d): Shows EIS Fe XII intensity maps before (5 hours) and after (9 hours) the flux emergence begins. (e) & (f): Shows EIS Fe XII Doppler velocity maps before (5 hours) and after (9 hours) the flux emergence begins. The Doppler velocity range is between ±20 km s^{-1}. (g) & (h): Shows two HMI magnetogram maps before (5 hours) and after (9 hours) the flux emergence begins. The minimum magnetic field strength is ±25 G. The blue boxes (black for the Doppler velocity maps) show where the new flux region will emerge.

In the EIS velocity maps, we see blueshift enhancements after the magnetic flux

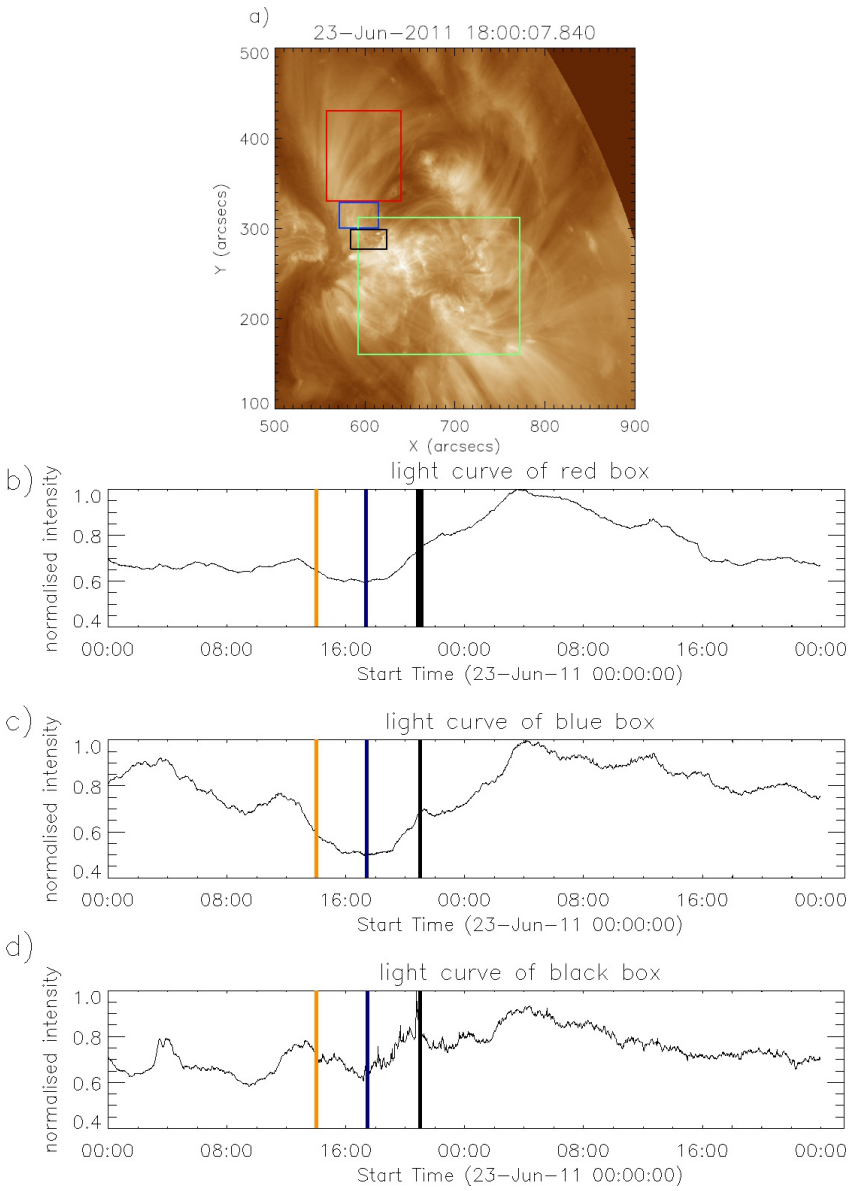

Figure 3.21: (a):Shows an AIA 193 Å image with the lightcurve extraction regions overlaid. We measure the intensity evolution in the loops to the north (red and blue box) and around the emerging flux region (black box). The light green box shows the EIS field of view.(b),(c) and (d): lightcurves for the red, dark blue and black regions shown in (a). The orange line shows the start time of the first jets seen at approximately 14:00 UT, the blue line shows the start of the intensity rise seen after the start of the jets and the black line shows the end time for jets. This rise is determined as a continual increase in intensity over a extended period of time. The light curves for the dark blue and black boxes cover the north-eastern part of the EIS field of view.

emergence begins (fig. 3.20e), and we also see an intensity enhancement in the EIS intensity maps after the magnetic flux emergence begins (fig. 3.20d). These enhancements were not seen before the magnetic flux emergence (fig. 3.20a and c). The blueshifts are located where positive and negative flux meet at the north part of the emerging flux region (fig. 3.20h) and where there are intensity enhancements in the EIS 195 Å intensity data (fig. 3.20d). We relate these blueshift enhancements

to new upflows being created through magnetic reconnection of new flux with the pre-existing active region (the interaction between the negative flux of the emerging flux region and the positive flux of the pre-existing active region). We compared the velocities of the blue (black) box in figure 3.20e (before the magnetic flux emergence) and the velocities of the blue (black) box in figure 3.20g (during the magnetic flux emergence) and we find that the velocities in figure 3.20f had an average upflow velocity enhancement of 10 $\pm$4 km s^{-1} when compared with the velocities in figure 3.20c.

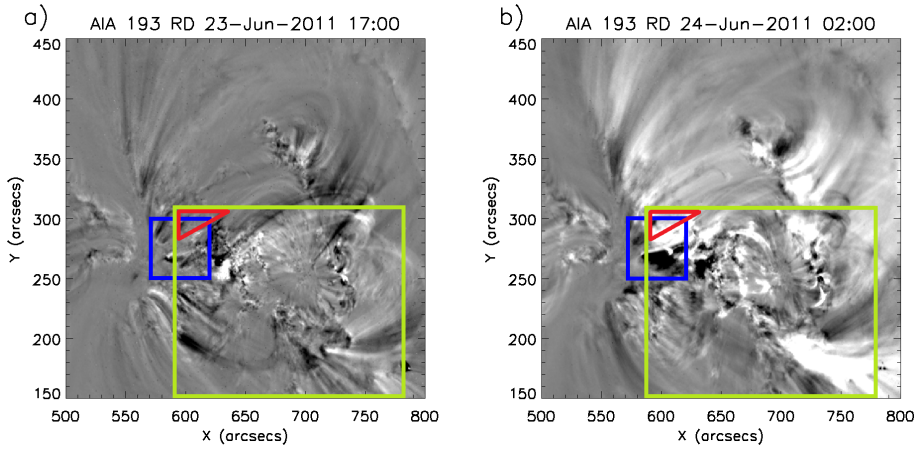

Figure 3.22: Shows running difference images before the rise in intensity (a) and at the peak of the intensity rise (b). We can clearly see an enhancement in intensity to the north of the emerging flux region (highlighted by the blue box). The green box represents the field of view of EIS and the red triangle represents the area where we see the upflow enhancements.

In fig. 3.21a, we extracted lightcurves for three of the boxes shown. The four boxes cover: the emerging flux region (black), the coronal loops north of the emerging flux region (dark blue), the coronal loops north of the blue box (red) and the EIS field-of-view (green box). These regions are used to try and understand the extent of the emerging flux region's effect on loops that are far away from the emerging flux region. In the intensity plots of these regions (fig. 3.21b to d), the start of the jets in the emerging flux region is represented by an orange line. We see a rise in intensity that starts approximately 3 hours after the jets begin (as shown by the blue line) and ends just after the jets end (as shown by the black line). We attribute this intensity rise to mean that new plasma has appeared in our extraction region. Therefore, we expect this rise in intensity to be associated with new loops forming over our extraction regions (as seen in fig. 3.22). The light blue box shows the location of the emerging flux region at 18:00 UT on 23 June 2011. It can be seen that the enhanced blueshifts are located in the northern part of the emerging flux region (as shown by the red triangle in figure 3.22) which is associated with the lower legs of the large-scale loops. This suggests that the cause of the blueshifts is chromospheric evaporation.

3.3.2.2.4 The end of the flux emergence phase

The flux emergence phase ends at approximately 01:00 on 24 June 2011. After this time, the emerging flux region enters a decay phase that lasts a further 23 hours. So can we see the atmospheric response to the end of the emergence?

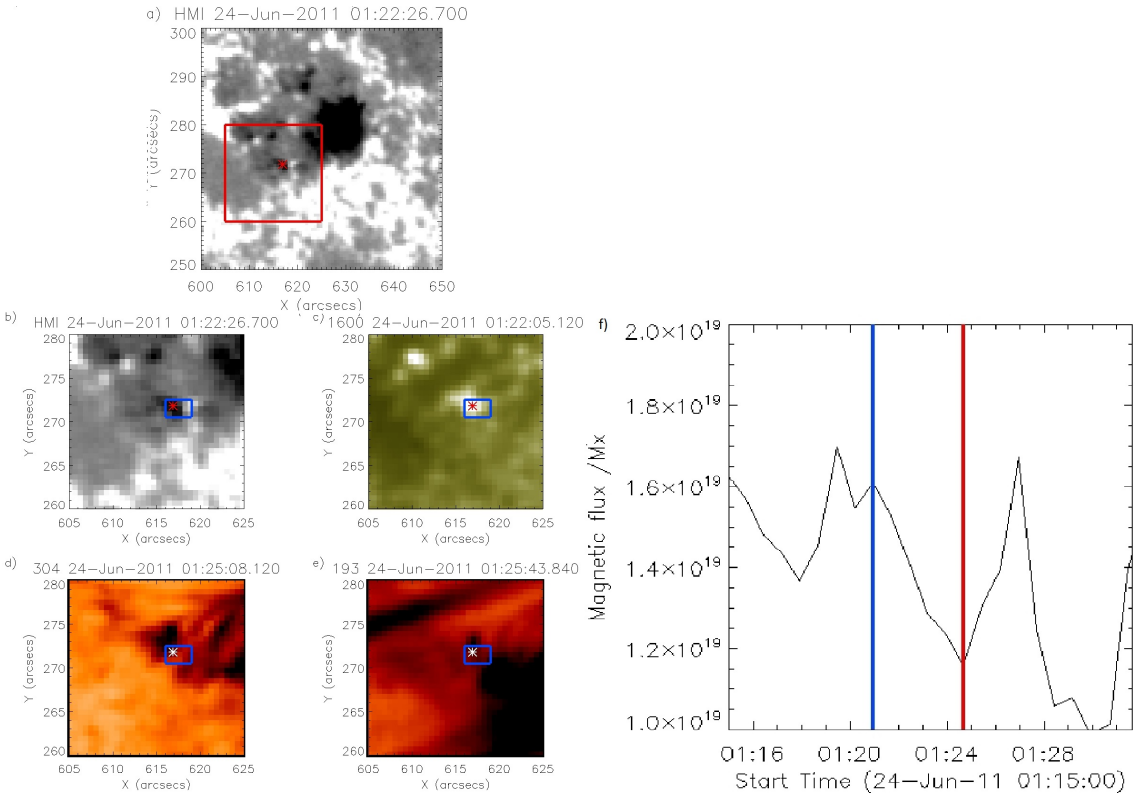

Figure 3.23: shows images from HMI (a,b) and in 1600 Å (c) , 304Å (d) and 193 Å (e) channels when a brightening occurs at the end of the flux emergence at approximately 01:15 on 24 June 2011. The 193 Å and 304 Å images are shown in a reverse colour table. The red (black in d and white in e) star represents the location of the brightening in the 1600 Å channel. The red box in image (a) shows the field of view of images (b) to (e). The blue box shows the extraction region for the flux cancellation measurement. The flux evolution profile for the positive polarity (f) was measured from the blue box in b, c, d and e. The blue vertical line shows the start of the flux cancellation and the red vertical line shows the end of the flux cancellation.

The final brightening we see is at 01:18 UT on 24 June 2011 in HMI (fig. 3.23a), in 1600 Å at 01:21 UT (fig. 3.23c), in 304 Å at 01:25 UT (fig. 3.23d) and in 193 Å at 01:26 UT (fig. 3.23e). The brightening is associated with magnetic flux cancellation between a small negative polarity and the pre-existing positive polarity of the active region (fig. 3.23b). The magnetic flux (associated with the positive polarity) around the brightening location decreases by 4.5×10^{18} Mx between 01:20.57 UT and 01:24.40 UT on 24 June 2011. The brightening lasts for approximately 3 minutes all three wavelengths and has an area of 310,000 km^2. The brightenings in 304 Å and 193 Å appear to be 1 - 2″ above the location of the 1600 Å brightening, which could be a height effect. This brightening is much

smaller than any of the brightenings seen before.

3.3.3 Timeline of flux emergence events in the second example

We note below the key events that happen when flux emergence occurs on 23 June 2011:

1. The flux emergence starts at 09:00 UT on 23 June 2011 (figure 3.9).
2. The serpentine field is first seen between 10:30 UT and 11:00 UT on 23 June 2011 (figure 3.10c).
3. First brightenings seen in 1600 Å at 10:50 UT on 23 June 2011. These are seen at the edge of the flux emergence (where the flux emergence interacts with the pre-existing active region) and have an area of approximately 750,000 km^2 (figure 3.11).
4. First brightenings seen in 304 Å and 193 Å at approximately 12:30 on 23 June 2011. These are seen in the serpentine field and have an area between 1.0 and 1.1 $\times 10^6$ km^2 (example of serpentine brightening in figure 3.12).
5. First jets seen at approximately 13:55 UT (chromosphere) and 14:00 UT (corona) on 23 June 2011 in the serpentine field. After this time, the majority of the brightenings have an area between 1.1 and 1.9 $\times 10^6$ km^2. We see brightenings at the edge of the flux emergence and where the serpentine field is located (figure 3.15).
6. Between 17:00 UT on 23 June 2011 and 00:00 UT on 24 June 2011, new loops are formed to the north of the flux emergence (up to 100″ from the flux emergence)(figure 3.21).
7. Upflow enhancements up to 10 km s^{-1} seen where negative polarity of emerging flux region interacts with the positive polarity of active region which lies to the north of the flux emergence (figure 3.20).
8. End of jets seen at approximately 22:00 UT on 23 June 2011.
9. End of flux emergence seen at 01:00 UT on 24 June 2011 (end of emergence phase in figure 3.9c).
10. End of brightenings in all three wavelengths at approximately 01:15 on 24 June 2011. The brightenings are located at the edge of the magnetic flux emergence and the majority of the brightenings have an area below 500,000 km^2 (figure 3.23).

3.3.4 Interpretation

3.3.4.1 The early stages of the flux emergence

We think that the first brightenings we see (fig. 3.11) are as a result of reconnection occurring between two small bipoles near the edge of the flux emergence. This area is a favourable site for magnetic reconnection because we see positive and negative polarities interacting with each other and a decrease in flux where the polarities are interacting. As a result of magnetic reconnection, we see one of the new bipoles disappearing and a brightening occurring above this location (as shown in figure 3.11 d). We attribute the disappearance of this new bipole to magnetic flux cancellation. In previous studies, brightenings in the atmosphere are one of many observational pieces of evidence for magnetic reconnection (e.g. Guglielmino et al. 2010). Magnetic flux cancellation is also another indicator of magnetic reconnection. If reconnection occurs in the lower parts of the atmosphere, one loop could have a small enough radius of curvature that magnetic tension can pull the loop under the photosphere (van Ballegooijen and Martens 1989). In magnetograms, we see this as magnetic flux cancellation.

The coronal jets seen appear to agree with what has been seen in previous work on jets in the solar atmosphere (Heyvaerts & Priest 1977; Shibata 1992). Figure 3.24 describes the formation of the jets seen along the serpentine field. Magnetic reconnection occurs between the negative polarity of the serpentine field and the positive polarity of the active region (fig.3.24a). This is the favourable site for magnetic reconnection as we have oppositely directed (anti-parallel) fieldlines. Magnetic reconnection occurs at this location and a jet is released (fig. 3.24b). Current reconnection models suggest that magnetic reconnection creates a small magnetic loop and a larger open-like fieldline that now has its footpoint in the positive field of the emerging flux region. In our case, the new foopoint location is associated with the positive polarity of the serpentine field (fig. 3.24c). In figure 3.15, we see that the brightening is associated with the jet where magnetic reconnection is favourable within the serpentine field.

In the serpentine brightenings (fig. 3.16 and 3.17), the magnetic reconnection could follow the cartoon in figure 3.25 which is based on the model in Pariat et al. (2004). In the model of Pariat et al. (2004), brightenings in the wings of the Hα line (called Ellerman bombs) are located over flux cancellation sites. The magnetic flux cancellation sites are favourable locations for magnetic reconnection and successive reconnection events can build up longer magnetic field lines in the serpentine field. As magnetic reconnection continues, some of the plasma drains from the Ω-loops into the U-loops and the remaining magnetic flux is able to rise through the atmosphere (as shown in fig. 3.25).

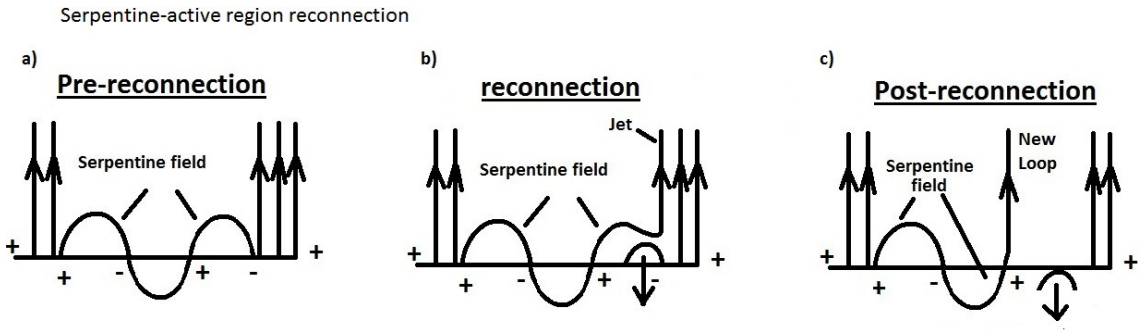

Figure 3.24: Cartoon showing the magnetic field layout of the active region and the serpentine field. (a) cartoon shows the magnetic configuration before reconnection occurs highlighting the serpentine field and the pre-existing field. (b) cartoon shows where the reconnection occurs to form the jet and the smaller reconnection loop. (c) shows the new magnetic configuration after reconnection. This cartoon describes where and how the jets seen in fig 3.14,(a) and (b) were created.

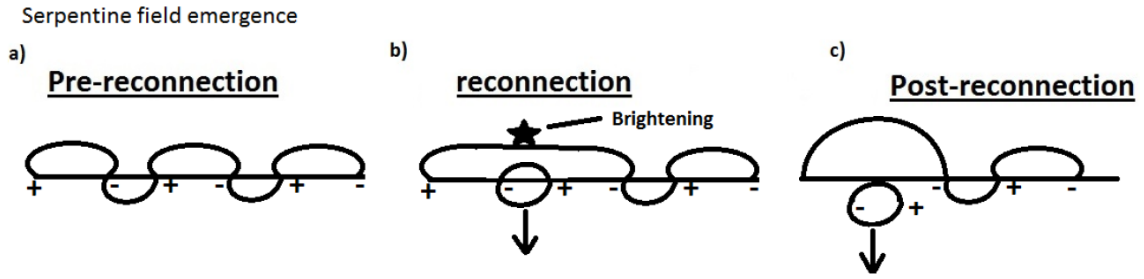

Figure 3.25: Cartoon showing reconnection within the serpentine field. This cartoon is based on the model of Pariat et al. (2004).

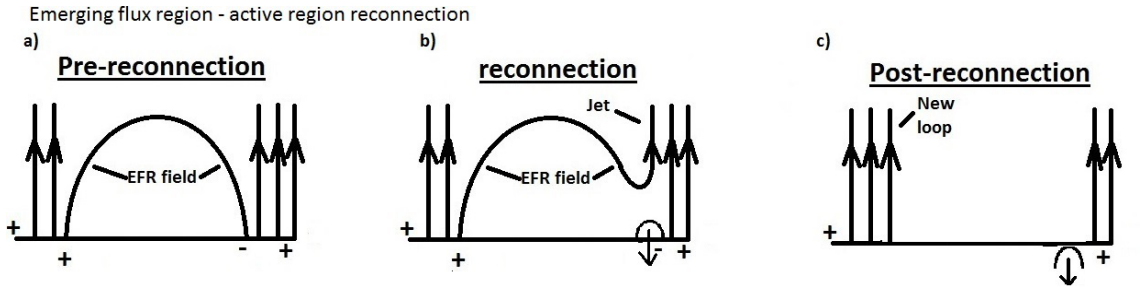

Figure 3.26: Cartoon showing the magnetic field layout of the active region and the emerging flux region. This includes the global emerging flux region loop in (b) and the new loops highlighted on the left-hand side of (c). The cartoon describes how the jets seen in fig. 3.18, (a) & (b) were created. The cartoon also describes how the intensity enhancements seen in the light curves in fig. 3.21 are connected to the emergence of the new flux and how we can attribute these intensity enhancements to new loops being formed away from the emerging flux region.

3.3.4.2 The evolution of the flux emergence after 17:00 UT on 23 June

At later stages (fig. 3.26) of the magnetic flux emergence (approximately 8 hours after the magnetic flux emergence begins), the serpentine field has disappeared following successive reconnections (this explains why we continue to see jets forming over the serpentine field), leaving two major polarities of the emerging flux region.

The coronal loops now form between these two polarities, but the negative polarity of the flux emergence is still interacting with the positive polarity of the active region (fig. 3.26a). So magnetic reconnection continues to take place between the negative polarity of the emerging flux region and the positive polarity of the active region (which is connected to a negative spot to the west). The pre-existing magnetic field lines are relatively larger compared to the fieldlines associated with the emerging flux. As before, a smaller new loop is formed at the reconnection site. However, the new larger loop that forms is now over the major positive polarity of the emerging flux region and so the jets are formed along this loop (fig. 3.26b). We see brightenings near the jet footpoint which is the favourable site for magnetic reconnection (fig. 3.19). Following successive reconnections between the negative polarity of the emerging flux region and the positive polarity of the pre-existing active region, new loops start to build up on the north side of the emerging flux region (fig. 3.26c) as we see in the observations (fig. 3.21). This process is described by interchange reconnection (Del Zanna et al. 2011).

3.3.4.3 The end of the flux emergence

In the final brightening (fig. 3.23), both bipoles are small and are connected by small, closed loops. This scenario does not follow the previous cartoons, but magnetic reconnection is still possible between the two bipoles.

3.4 Discussion - comparison between both emerging flux regions

The average flux density of the emerging flux region in the first active region (section 3.2) is 490 G and peak flux for the emerging flux region occurs at the same time. The average flux density of the emerging flux region in the second active region (section 3.3) at the time of peak flux (in the EFR) is 190 G. When we study the evolution of the 10926 EFR (first example), we see that it plays a significant role in increasing the amount of flux in the active region, so finding a flux density that is higher than that of the active region is not surprising. On the other hand, the active region AR11236 (second example) continues to decay, despite the injection of new flux.

In the first example, the flux emergence has 3.4 $\times 10^{21}$ Mx of unsigned flux and lasts for 32 hours, while in the second example, the flux emergence has 4.7 $\times 10^{21}$ Mx of unsigned flux (however HMI can resolve objects 3 times better than MDI could). and only lasts for 15 hours. So the magnetic flux emergence rate is faster in the second example than in the first example. It also appears that the emerging flux region in the first example covers a wider area than the emerging flux region in the second example.

The chromospheric brightenings in the first example appear 80 minutes after the magnetic flux emergence begins. While in the second example, the chromospheric brightenings appear 200 minutes after the magnetic flux emergence begins.

In the corona, the upflows that have been attributed to reconnection by the simulations (Harra et al. 2012) for the first example appear between 5 and 8 hours after the magnetic flux emergence begins and are seen at the western edge of the active region. The outflows seen on the eastern side are thought to be caused by an increase in the pressure gradient (Murray et al. 2010). In the second example, we first see jets 5 hours after the flux emergence begins and they are seen in the emerging serpentine field. The first jets seen at the edge of the EFR in the second example occur 8 hours after the magnetic flux emergence begins. We agree with Su et al. (2012) that the jets found are the result of magnetic reconnection and that these jets do appear in the upper chromosphere and then in the corona (as we see jets being formed in the 304 Å data before the 193 Å data).

It does appear that emerging flux regions with different average flux densities have an effect on active regions. The effect however does depend on average flux density: the emerging flux region in the first example is able to create persistent outflows up to 50 km s^{-1} while the emerging flux region in the second example is only able to form small upflow enhancements, small-scale jets and new loops. The timing and location of the jets suggests that the jets help facilitate the emergence of the serpentine field from the photosphere in the atmosphere. We have seen for the first time, coronal jets originating in the serpentine field.

During the lifetime of the EFR in the first example there are several flares, including a Cl.2 flare, 8 hours after the flux emergence begins. There is no evidence that the second example EFR produces flares of this magnitude.

There are currently no simulations that cover the serpentine field and the upper atmosphere together. So we cannot currently compare our observations of the second active region with any simulations. The simulations used in the first example did not look at the serpentine field, so cannot detect the coronal jets in the serpentine. However, coronal jets driven by magnetic reconnection, were found at the western edge of the emerging flux region (this was the favourable side for magnetic reconnection). The simulations by Cheung et al. (2008) and Pariat et al. (2004) include the serpentine field, but only extend as far as the lower chromosphere. Chromospheric brightenings and chromospheric jets are seen in the simulations at sites within the serpentine field where magnetic reconnection is favourable, which is what we see in the AIA 304 Å data.

3.5 Conclusion

We have studied how flux emergence affects an active region. We looked at an emerging flux region with a high flux density studied by Harra et al. (2010) and Harra et al. (2012) and then compared the results to a emerging flux region that has a lower flux density. We found that it is possible that coronal jets can form over the serpentine field at the early stages of flux emergence. This has not been seen before and this is possibly due to the lack of high temporal and spatial resolution. However, we do see coronal enhancements in the line width and velocity maps from EIS in the first example. In our second example, the flux emergence still has an effect on loops that are in the vicinity of the flux emergence and is able to create small-scale jets. At the later stages of the flux emergence, the footpoint of the jets shift towards the edges of the emerging flux region. However, unlike in Harra et al. (2010), the second emerging flux region produces smaller blueshift enhancements. We have found that flux emergence can create new upflows and new large coronal loops regardless of size. We have also found (in the second example) that reconnection-driven jets can form over the serpentine field.

We have also looked at EUV brightenings associated with the flux emergence. The brightenings start approximately two hours after the flux emergence begins and ends at the same time as the flux emergence ends. This suggests that successive reconnections are required before brightenings can occur at the higher layers of the atmosphere. When we see the jets and the brightenings at the same time, they occur in the same part of the flux emergence which is in agreement with our cartoons shown in the previous section. However, the majority of non-jet related brightenings do not follow our previous cartoons. Instead, they appear to follow the picture painted by serpentine field models (e.g. Pariat et al. 2004 or Cheung et al. 2008) and shown in fig. 3.25.

Chapter 4

Future work

We know now that an emerging flux region can have an effect on the corona regardless of size. But will two emerging flux regions of a similar size give a similar result? With the higher temporal and spatial resolution of the Solar Dynamics Observatory, can we see more jets in the serpentine field and will they have similar velocities and sizes to those seen in this study? With future solar telescopes like Solar-C that will probe all the way from the photosphere to the corona, we should also expect to find the height where the reconnection is taking place to form the jets and the new loops. We will also be able to see how the energetics of the jets change with height, and be able to study the evolution of the serpentine field and the role magnetic reconnection plays in pulling the serpentine field through the photosphere.

We would also like to investigate how the atmosphere responds to the emergence of a new active region into the quiet Sun. We would like to know if outflows are formed and how they are formed. We would expect to see outflows form, but at a later time compared to the outflows seen in 3.2 as we are reliant on the active region to build up enough large-scale loops to reconnect with other active regions (for example, Harra et al. 2008). An active region in quiet Sun with outflows would also allow us to probe the role of QSLs in producing outflows. We would also like to know how far into the emergence do outflows start to be detected and are they at a constant frequency after they begin. A constant frequency would tell us that we may be seeing waves and not flows. However, an irregular frequency would tell us that these "outflows" are flowing plasma and not waves. We would also like to investigate how outflows evolve when active regions survive a number of rotations. This would give us a greater understanding of the role of emerging flux in producing the phenomena we see in the atmosphere.

Bibliography

H. Alfvén. On the Effect of a Vertical Magnetic Field in a Conducting Atmosphere. *Arkiv for Astronomi*, 29:1–6, 1943.

M. J. Aschwanden. *Physics of the Solar Corona. An Introduction with Problems and Solutions (2nd edition)*. December 2005.

G. Aulanier, E. Pariat, P. Démoulin, and C. R. DeVore. Slip-Running Reconnection in Quasi-Separatrix Layers. *Solar Phys.*, 238:347–376, November 2006. doi: 10.1007/s11207-006-0230-2.

D. Baker, L. van Driel-Gesztelyi, C. H. Mandrini, P. Démoulin, and M. J. Murray. Magnetic Reconnection along Quasi-separatrix Layers as a Driver of Ubiquitous Active Region Outflows. *Astrophys. J.*, 705:926–935, November 2009. doi: 10.1088/0004-637X/705/1/926.

S. Basu, W. J. Chaplin, Y. Elsworth, R. New, and A. M. Serenelli. Fresh Insights on the Structure of the Solar Core. *Astrophys. J.*, 699:1403–1417, July 2009. doi: 10.1088/0004-637X/699/2/1403.

L. R. Bellot Rubio and C. Beck. Magnetic Flux Cancellation in the Moat of Sunspots: Results from Simultaneous Vector Spectropolarimetry in the Visible and the Infrared. *Astrophys. J. Lett*, 626:L125–L128, June 2005. doi: 10.1086/431648.

A. O. Benz. Flare Observations. *Living Reviews in Solar Physics*, 5:1, February 2008. doi: 10.12942/lrsp-2008-1.

P. N. Bernasconi, D. M. Rust, M. K. Georgoulis, and B. J. Labonte. Moving Dipolar Features in an Emerging Flux Region. *Solar Phys.*, 209:119–139, September 2002. doi: 10.1023/A:1020943816174.

H. A. Bethe and C. L. Critchfield. The formation of deuterons by proton combination. *Phys. Rev.*, 54:248–254, Aug 1938. doi: 10.1103/PhysRev.54.248. URL http://link.aps.org/doi/10.1103/PhysRev.54.248.

G. E. Brueckner and J.-D. F. Bartoe. Observations of high-energy jets in the corona above the quiet sun, the heating of the corona, and the acceleration of the solar wind. *Astrophys. J.*, 272:329–348, September 1983. doi: 10.1086/161297.

H. Carmichael. A Process for Flares. *NASA Special Publication*, 50:451, 1964.

R. C. Carrington. On two cases of Solar Spots in High Latitudes, and on the Surface Currents indicated by the Observations. *Mon. Not. Roy. Astron. Soc.*, 20:254, April 1860.

J. Chen, S. Bao, and H. Zhang. Helicity Patterns of the Active Regions Connected by Transequatorial Loops. *Solar Phys.*, 242:65–85, May 2007. doi: 10.1007/s11207-007-0284-9.

M. C. M. Cheung, M. Schüssler, T. D. Tarbell, and A. M. Title. Solar Surface Emerging Flux Regions: A Comparative Study of Radiative MHD Modeling and Hinode SOT Observations. *Astrophys. J.*, 687:1373–1387, November 2008. doi: 10.1086/591245.

F. Chiuderi-Drago, N. Mein, and M. Pick. Unstable chromospheric dark features and type-III bursts association. *Solar Phys.*, 103:235–247, February 1986. doi: 10.1007/BF00147827.

J. W. Cirtain, L. Golub, L. Lundquist, A. van Ballegooijen, A. Savcheva, M. Shimojo, E. DeLuca, S. Tsuneta, T. Sakao, K. Reeves, M. Weber, R. Kano, N. Narukage, and K. Shibasaki. Evidence for Alfvén Waves in Solar X-ray Jets. *Science*, 318:1580–, December 2007. doi: 10.1126/science.1147050.

R. M. Close, C. E. Parnell, D. H. Mackay, and E. R. Priest. Statistical Flux Tube Properties of 3D Magnetic Carpet Fields. *Solar Phys.*, 212:251–275, February 2003. doi: 10.1023/A:1022961913168.

L. Culhane, L. K. Harra, D. Baker, L. van Driel-Gesztelyi, J. Sun, G. A. Doschek, D. H. Brooks, L. L. Lundquist, S. Kamio, P. R. Young, and V. H. Hansteen. Hinode EUV Study of Jets in the Sun's South Polar Corona. *Pub. Astron. Soc. Japan*, 59:751, November 2007.

I. de Moortel. Longitudinal Waves in Coronal Loops. *Space Sci. Rev.*, 149:65–81, December 2009. doi: 10.1007/s11214-009-9526-5.

B. de Pontieu, S. McIntosh, V. H. Hansteen, M. Carlsson, C. J. Schrijver, T. D. Tarbell, A. M. Title, R. A. Shine, Y. Suematsu, S. Tsuneta, Y. Katsukawa, K. Ichimoto, T. Shimizu, and S. Nagata. A Tale of Two Spicules: The Impact of Spicules on the Magnetic Chromosphere. *Pub. Astron. Soc. Japan*, 59:655, November 2007.

B. De Pontieu, S. W. McIntosh, V. H. Hansteen, and C. J. Schrijver. Observing the Roots of Solar Coronal Heating in the Chromosphere. *Astrophys. J. Lett*, 701: L1–L6, August 2009. doi: 10.1088/0004-637X/701/1/L1.

G. Del Zanna. Flows in active region loops observed by Hinode EIS. *Astron. Astrophys.*, 481:L49–L52, April 2008. doi: 10.1051/0004-6361:20079087.

G. Del Zanna, G. Aulanier, K.-L. Klein, and T. Török. A single picture for solar coronal outflows and radio noise storms. *Astron. Astrophys.*, 526:A137, February 2011. doi: 10.1051/0004-6361/201015231.

G. A. Doschek, H. P. Warren, J. T. Mariska, K. Muglach, J. L. Culhane, H. Hara, and T. Watanabe. Flows and Nonthermal Velocities in Solar Active Regions Observed with the EUV Imaging Spectrometer on Hinode: A Tracer of Active Region Sources of Heliospheric Magnetic Fields? *Astrophys. J.*, 686:1362–1371, October 2008. doi: 10.1086/591724.

G. A. Doschek, E. Landi, H. P. Warren, and L. K. Harra. Bright Points and Jets in Polar Coronal Holes Observed by the Extreme-Ultraviolet Imaging Spectrometer on Hinode. *Astrophys. J.*, 710:1806–1824, February 2010. doi: 10.1088/0004-637X/710/2/1806.

F. Ellerman. Solar Hydrogen "bombs". *Astrophys. J.*, 46:298, November 1917. doi: 10.1086/142366.

G. H. Fisher, Y. Fan, and R. F. Howard. Comparisons between theory and observation of active region tilts. *Astrophys. J.*, 438:463–471, January 1995. doi: 10.1086/175090.

T. G. Forbes. Solar and stellar flares. In *Astronomy, physics and chemistry of H^+_3*, volume 358 of *Royal Society of London Philosophical Transactions Series A*, pages 711–727, February 2000. doi: 10.1098/rsta.2000.0554.

V. Gaizauskas. Preflare activity. *Solar Phys.*, 121:135–152, March 1989. doi: 10.1007/BF00161692.

V. Gaizauskas. The birth and evolution of solar active regions. *Advances in Space Research*, 13:5–14, September 1993. doi: 10.1016/0273-1177(93)90450-P.

R. A. García, S. Turck-Chièze, S. J. Jiménez-Reyes, J. Ballot, P. L. Pallé, A. Eff-Darwich, S. Mathur, and J. Provost. Tracking Solar Gravity Modes: The Dynamics of the Solar Core. *Science*, 316:1591–, June 2007. doi: 10.1126/science.1140598.

C. P. Goff, L. van Driel-Gesztelyi, P. Démoulin, J. L. Culhane, S. A. Matthews, L. K. Harra, C. H. Mandrini, K. L. Klein, and H. Kurokawa. A Multiple Flare Scenario where the Classic Long-Duration Flare Was Not the Source of a CME. *Solar Phys.*, 240:283–299, February 2007. doi: 10.1007/s11207-007-0260-4.

L. Golub and J. M. Pasachoff. *The Solar Corona*. September 1997.

C. Gontikakis, V. Archontis, and K. Tsinganos. Observations and 3D MHD simulations of a solar active region jet. *Astron. Astrophys.*, 506:L45–L48, November 2009. doi: 10.1051/0004-6361/200913026.

S. L. Guglielmino, F. Zuccarello, P. Romano, and L. R. Bellot Rubio. Hinode Observations of Chromospheric Brightenings in the Ca II H Line during Small-Scale Flux Emergence Events. *Astrophys. J. Lett*, 688:L111–L114, December 2008. doi: 10.1086/595657.

S. L. Guglielmino, L. R. Bellot Rubio, F. Zuccarello, G. Aulanier, S. Vargas Domínguez, and S. Kamio. Multiwavelength Observations of Small-scale Reconnection Events Triggered by Magnetic Flux Emergence in the Solar Atmosphere. *Astrophys. J.*, 724:1083–1098, December 2010. doi: 10.1088/0004-637X/724/2/1083.

G. E. Hale and S. B. Nicholson. The Law of Sun-Spot Polarity. *Astrophys. J.*, 62:270, November 1925. doi: 10.1086/142933.

G. E. Hale, F. Ellerman, S. B. Nicholson, and A. H. Joy. The Magnetic Polarity of Sun-Spots. *Astrophys. J.*, 49:153, April 1919. doi: 10.1086/142452.

H. Hara, T. Watanabe, L. K. Harra, J. L. Culhane, P. R. Young, J. T. Mariska, and G. A. Doschek. Coronal Plasma Motions near Footpoints of Active Region Loops Revealed from Spectroscopic Observations with Hinode EIS. *Astrophys. J. Lett*, 678:L67–L71, May 2008. doi: 10.1086/588252.

L. K. Harra and K. O. Mason. *Space Science*. Imperial College Press, January 2004.

L. K. Harra, T. Sakao, C. H. Mandrini, H. Hara, S. Imada, P. R. Young, L. van Driel-Gesztelyi, and D. Baker. Erratum: "Outflows at the Edges of Active Regions: Contribution to Solar Wind Formation?" (¡A href="/abs/2008ApJ...676L.147H"¿ApJ, 676, L147 [2008]¡/A¿). *Astrophys. J. Lett*, 677:L159–L159, April 2008. doi: 10.1086/588288.

L. K. Harra, T. Magara, H. Hara, S. Tsuneta, T. J. Okamoto, and A. J. Wallace. Response of the Solar Atmosphere to the Emergence of 'Serpentine' Magnetic Field. *Solar Phys.*, 263:105–119, May 2010. doi: 10.1007/s11207-010-9548-x.

L. K. Harra, V. Archontis, E. Pedram, A. W. Hood, D. L. Shelton, and L. van Driel-Gesztelyi. The Creation of Outflowing Plasma in the Corona at Emerging Flux Regions: Comparing Observations and Simulations. *Solar Phys.*, 278:47–71, May 2012. doi: 10.1007/s11207-011-9855-x.

J. Heyvaerts, E. R. Priest, and D. M. Rust. An emerging flux model for the solar flare phenomenon. *Astrophys. J.*, 216:123–137, August 1977. doi: 10.1086/155453.

T. Hirayama. Theoretical Model of Flares and Prominences. I: Evaporating Flare Model. *Solar Phys.*, 34:323–338, February 1974. doi: 10.1007/BF00153671.

S. Kamio, H. Hara, T. Watanabe, K. Matsuzaki, K. Shibata, L. Culhane, and H. P. Warren. Velocity Structure of Jets in a Coronal Hole. *Pub. Astron. Soc. Japan*, 59:757, November 2007.

S. Kamio, H. Hara, T. Watanabe, T. Fredvik, and V. H. Hansteen. Modeling of EIS Spectrum Drift from Instrumental Temperatures. *Solar Phys.*, 266:209–223, September 2010. doi: 10.1007/s11207-010-9603-7.

J. A. Klimchuk. On Solving the Coronal Heating Problem. *Solar Phys.*, 234:41–77, March 2006. doi: 10.1007/s11207-006-0055-z.

R. A. Kopp and G. W. Pneuman. Magnetic reconnection in the corona and the loop prominence phenomenon. *Solar Phys.*, 50:85–98, October 1976. doi: 10.1007/BF00206193.

A. G. Kosovichev. Photospheric and Subphotospheric Dynamics of Emerging Magnetic Flux. *Space Sci. Rev.*, 144:175–195, April 2009. doi: 10.1007/s11214-009-9487-8.

H. Kurokawa. High-resolution observations of H-alpha flare regions. *Space Sci. Rev.*, 51:49–84, October 1989. doi: 10.1007/BF00226268.

H. Kurokawa, G. Kawai, R. Kitai, Y. Funakoshi, Y. Nakai, S. Tsuneta, T. Kosugi, S. Enome, L. W. Acton, and Y. Ogawara. Detailed comparison between H-alpha and YOHKOH soft X-ray images of a confined two-ribbon flare. *Pub. Astron. Soc. Japan*, 44:L129–L133, October 1992.

B. Lites, H. Socas-Navarro, M. Kubo, T. Berger, Z. Frank, R. A. Shine, T. D. Tarbell, A. M. Title, K. Ichimoto, Y. Katsukawa, S. Tsuneta, Y. Suematsu, and T. Shimizu. Hinode Observations of Horizontal Quiet Sun Magnetic Flux and the "Hidden Turbulent Magnetic Flux". *Pub. Astron. Soc. Japan*, 59:571, November 2007.

W. Liu, T. E. Berger, A. M. Title, and T. D. Tarbell. An Intriguing Chromospheric Jet Observed by Hinode: Fine Structure Kinematics and Evidence of Unwinding Twists. *Astrophys. J. Lett*, 707:L37–L41, December 2009. doi: 10.1088/0004-637X/707/1/L37.

M. C. López Fuentes, P. Démoulin, C. H. Mandrini, A. A. Pevtsov, and L. van Driel-Gesztelyi. Magnetic twist and writhe of active regions. On the origin of deformed flux tubes. *Astron. Astrophys.*, 397:305–318, January 2003. doi: 10.1051/0004-6361:20021487.

T. Magara and S. Tsuneta. Hinode's Observational Result on the Saturation of Magnetic Helicity Injected into the Solar Atmosphere and Its Relation to the Occurrence of a Solar Flare. *Pub. Astron. Soc. Japan*, 60:1181–, October 2008.

C. H. Mandrini, P. Démoulin, and J. A. Klimchuk. Magnetic Field and Plasma Scaling Laws: Their Implications for Coronal Heating Models. *Astrophys. J.*, 530:999–1015, February 2000. doi: 10.1086/308398.

E. Marsch, H. Tian, J. Sun, W. Curdt, and T. Wiegelmann. Plasma Flows Guided by Strong Magnetic Fields in the Solar Corona. *Astrophys. J.*, 685:1262–1269, October 2008. doi: 10.1086/591038.

M. J. Martínez González and L. R. Bellot Rubio. Emergence of Small-scale Magnetic Loops Through the Quiet Solar Atmosphere. *Astrophys. J.*, 700:1391–1403, August 2009. doi: 10.1088/0004-637X/700/2/1391.

T. Miyagoshi and T. Yokoyama. Magnetohydrodynamic Numerical Simulations of Solar X-Ray Jets Based on the Magnetic Reconnection Model That Includes Chromospheric Evaporation. *Astrophys. J. Lett*, 593:L133–L136, August 2003. doi: 10.1086/378215.

R. L. Moore, A. C. Sterling, J. W. Cirtain, and D. A. Falconer. Solar X-ray Jets, Type-II Spicules, Granule-size Emerging Bipoles, and the Genesis of the Heliosphere. *Astrophys. J. Lett*, 731:L18, April 2011. doi: 10.1088/2041-8205/731/1/L18.

F. Moreno-Insertis and K. Galsgaard. Plasma Jets and Eruptions in Solar Coronal Holes: A Three-dimensional Flux Emergence Experiment. *Astrophys. J.*, 771:20, July 2013. doi: 10.1088/0004-637X/771/1/20.

F. Moreno-Insertis, K. Galsgaard, and I. Ugarte-Urra. Jets in Coronal Holes: Hinode Observations and Three-dimensional Computer Modeling. *Astrophys. J. Lett*, 673:L211–L214, February 2008. doi: 10.1086/527560.

R. J. Morton. Chromospheric jets around the edges of sunspots. *Astron. Astrophys.*, 543:A6, July 2012. doi: 10.1051/0004-6361/201219137.

R. J. Morton, A. K. Srivastava, and R. Erdélyi. Observations of quasi-periodic phenomena associated with a large blowout solar jet. *Astron. Astrophys.*, 542:A70, June 2012. doi: 10.1051/0004-6361/201117218.

M. J. Murray, D. Baker, L. van Driel-Gesztelyi, and J. Sun. Outflows at the Edges of an Active Region in a Coronal Hole: A Signature of Active Region Expansion? *Solar Phys.*, 261:253–269, February 2010. doi: 10.1007/s11207-009-9484-9.

T. J. Okamoto, S. Tsuneta, T. E. Berger, K. Ichimoto, Y. Katsukawa, B. W. Lites, S. Nagata, K. Shibata, T. Shimizu, R. A. Shine, Y. Suematsu, T. D. Tarbell, and A. M. Title. Coronal Transverse Magnetohydrodynamic Waves in a Solar Prominence. *Science*, 318:1577–, December 2007. doi: 10.1126/science.1145447.

K. Otsuji, K. Shibata, R. Kitai, S. Ueno, S. Nagata, T. Matsumoto, T. Nakamura, H. Watanabe, S. Tsuneta, Y. Suematsu, K. Ichimoto, T. Shimizu, Y. Katsukawa, T. D. Tarbell, B. Lites, R. A. Shine, and Title Alan M. Small-Scale Magnetic-Flux Emergence Observed with Hinode Solar Optical Telescope. *Pub. Astron. Soc. Japan*, 59:649, November 2007.

E. Pariat, G. Aulanier, B. Schmieder, M. K. Georgoulis, D. M. Rust, and P. N. Bernasconi. Resistive Emergence of Undulatory Flux Tubes. *Astrophys. J.*, 614: 1099–1112, October 2004. doi: 10.1086/423891.

E. N. Parker. Sweet's Mechanism for Merging Magnetic Fields in Conducting Fluids. *J. Geophys. Res.*, 62:509–520, December 1957. doi: 10.1029/JZ062i004p00509.

E. N. Parker. The Solar-Flare Phenomenon and the Theory of Reconnection and Annihiliation of Magnetic Fields. *Astrophys. J. Space Sci.*, 8:177, July 1963. doi: 10.1086/190087.

E. N. Parker. The Dynamical State of the Interstellar Gas and Field. *Astrophys. J.*, 145:811, September 1966. doi: 10.1086/148828.

E. N. Parker. Depth of origin of solar active regions. *Astrophys. J.*, 280:423–427, May 1984. doi: 10.1086/162008.

S. Patsourakos and J. A. Klimchuk. Nonthermal Spectral Line Broadening and the Nanoflare Model. *Astrophys. J.*, 647:1452–1465, August 2006. doi: 10.1086/505517.

H. E. Petschek. Magnetic Field Annihilation. *NASA Special Publication*, 50:425, 1964.

E. R. Priest and T. G. Forbes. Steady magnetic reconnection in three dimensions. *Solar Phys.*, 119:211–214, March 1989. doi: 10.1007/BF00146222.

Fabio Reale. Coronal loops: Observations and modeling of confined plasma. *Living Reviews in Solar Physics*, 7(5), 2010. doi: 10.12942/lrsp-2010-5. URL http://www.livingreviews.org/lrsp-2010-5.

T. Sakao, R. Kano, N. Narukage, J. Kotoku, T. Bando, E. E. DeLuca, L. L. Lundquist, S. Tsuneta, L. K. Harra, Y. Katsukawa, M. Kubo, H. Hara, K. Matsuzaki, M. Shimojo, J. A. Bookbinder, L. Golub, K. E. Korreck, Y. Su, K. Shibasaki, T. Shimizu, and I. Nakatani. Continuous Plasma Outflows from

the Edge of a Solar Active Region as a Possible Source of Solar Wind. *Science*, 318:1585–, December 2007. doi: 10.1126/science.1147292.

P. H. Scherrer, R. S. Bogart, R. I. Bush, J. T. Hoeksema, A. G. Kosovichev, J. Schou, W. Rosenberg, L. Springer, T. D. Tarbell, A. Title, C. J. Wolfson, I. Zayer, and MDI Engineering Team. The Solar Oscillations Investigation - Michelson Doppler Imager. *Solar Phys.*, 162:129–188, December 1995. doi: 10.1007/BF00733429.

K. Schindler and G. Hornig. *Magnetic Reconnection*. November 2000. doi: 10.1888/0333750888/2224.

B. Schmieder, D. M. Rust, M. K. Georgoulis, P. Démoulin, and P. N. Bernasconi. Emerging Flux and the Heating of Coronal Loops. *Astrophys. J.*, 601:530–545, January 2004. doi: 10.1086/380199.

C. J. Schrijver and G. L. Siscoe. *Heliophysics: Plasma Physics of the Local Cosmos*. Cambridge University Press, July 2009.

C. J. Schrijver, A. M. Title, K. L. Harvey, N. R. Sheeley, Y.-M. Wang, G. H. J. van den Oord, R. A. Shine, T. D. Tarbell, and N. E. Hurlburt. Large-scale coronal heating by the small-scale magnetic field of the Sun. *Nature*, 394:152–154, July 1998. doi: 10.1038/28108.

N. R. Sheeley, Jr. Temporal variations of loop structures in the solar atmosphere. *Solar Phys.*, 66:79–87, May 1980. doi: 10.1007/BF00150520.

K. Shibata, Y. Ishido, L. W. Acton, K. T. Strong, T. Hirayama, Y. Uchida, A. H. McAllister, R. Matsumoto, S. Tsuneta, T. Shimizu, H. Hara, T. Sakurai, K. Ichimoto, Y. Nishino, and Y. Ogawara. Observations of X-ray jets with the YOHKOH Soft X-ray Telescope. *Pub. Astron. Soc. Japan*, 44:L173–L179, October 1992.

K. Shibata, T. Nakamura, T. Matsumoto, K. Otsuji, T. J. Okamoto, N. Nishizuka, T. Kawate, H. Watanabe, S. Nagata, S. UeNo, R. Kitai, S. Nozawa, S. Tsuneta, Y. Suematsu, K. Ichimoto, T. Shimizu, Y. Katsukawa, T. D. Tarbell, T. E. Berger, B. W. Lites, R. A. Shine, and A. M. Title. Chromospheric Anemone Jets as Evidence of Ubiquitous Reconnection. *Science*, 318:1591–, December 2007. doi: 10.1126/science.1146708.

M. Shimojo, S. Hashimoto, K. Shibata, T. Hirayama, H. S. Hudson, and L. W. Acton. Statistical Study of Solar X-Ray Jets Observed with the YOHKOH Soft X-Ray Telescope. *Pub. Astron. Soc. Japan*, 48:123–136, February 1996.

H. C. Spruit, A. M. Title, and A. A. van Ballegooijen. Is there a weak mixed polarity background field? Theoretical arguments. *Solar Phys.*, 110:115–128, March 1987. doi: 10.1007/BF00148207.

L. H. Strous, G. Scharmer, T. D. Tarbell, A. M. Title, and C. Zwaan. Phenomena in an emerging active region. I. Horizontal dynamics. *Astron. Astrophys.*, 306: 947, February 1996.

P. A. Sturrock. Model of the High-Energy Phase of Solar Flares. *Nature*, 211: 695–697, August 1966. doi: 10.1038/211695a0.

J. T. Su, Y. Liu, Y. D. Shen, S. Liu, and X. J. Mao. Observation of High-speed Outflows in Coronal Loops Associated with Photospheric Magnetic Field Evolution. *Astrophys. J.*, 760:82, November 2012. doi: 10.1088/0004-637X/760/1/82.

J. J. Sudol and J. W. Harvey. Longitudinal Magnetic Field Changes Accompanying Solar Flares. *Astrophys. J.*, 635:647–658, December 2005. doi: 10.1086/497361.

P. A. Sweet. The topology of force-free magnetic fields. *The Observatory*, 78:30–32, February 1958.

A. M. Title and C. J. Schrijver. The Sun's Magnetic Carpet. In R. A. Donahue and J. A. Bookbinder, editors, *Cool Stars, Stellar Systems, and the Sun*, volume 154 of *Astronomical Society of the Pacific Conference Series*, page 345, 1998.

S. Tomczyk, G. L. Card, T. Darnell, D. F. Elmore, R. Lull, P. G. Nelson, K. V. Streander, J. Burkepile, R. Casini, and P. G. Judge. An Instrument to Measure Coronal Emission Line Polarization. *Solar Phys.*, 247:411–428, February 2008. doi: 10.1007/s11207-007-9103-6.

D. Tripathi, H. E. Mason, B. N. Dwivedi, G. del Zanna, and P. R. Young. Active Region Loops: Hinode/Extreme-Ultraviolet Imaging Spectrometer Observations. *Astrophys. J.*, 694:1256–1265, April 2009. doi: 10.1088/0004-637X/694/2/1256.

A. A. van Ballegooijen and P. C. H. Martens. Formation and eruption of solar prominences. *Astrophys. J.*, 343:971–984, August 1989. doi: 10.1086/167766.

L. van Driel-Gesztelyi and J. L. Culhane. Magnetic Flux Emergence, Activity, Eruptions and Magnetic Clouds: Following Magnetic Field from the Sun to the Heliosphere. *Space Sci. Rev.*, 144:351–381, April 2009. doi: 10.1007/s11214-008-9461-x.

L. van Driel-Gesztelyi, J.-M. Malherbe, and P. Démoulin. Emergence of a U-loop - sub-photospheric link between solar active regions. *Astron. Astrophys.*, 364: 845–852, December 2000.

Y.-M. Wang, N. R. Sheeley, Jr., D. G. Socker, R. A. Howard, G. E. Brueckner, D. J. Michels, D. Moses, O. C. St. Cyr, A. Llebaria, and J.-P. Delaboudinière. Observations of Correlated White-Light and Extreme-Ultraviolet Jets from Polar Coronal Holes. *Astrophys. J.*, 508:899–907, December 1998. doi: 10.1086/306450.

Y.-M. Wang, E. Robbrecht, and K. Muglach. The Evolution of Dark Canopies Around Active Regions. *Astrophys. J.*, 733:20, May 2011. doi: 10.1088/0004-637X/733/1/20.

A. R. Winebarger and H. P. Warren. Cooling Active Region Loops Observed with SXT and TRACE. *Astrophys. J.*, 626:543–550, June 2005. doi: 10.1086/429817.

Z. Xu, A. Lagg, and S. K. Solanki. Magnetic structures of an emerging flux region in the solar photosphere and chromosphere. *Astron. Astrophys.*, 520:A77, September 2010. doi: 10.1051/0004-6361/200913227.

T. Yokoyama and K. Shibata. Magnetic reconnection as the origin of X-ray jets and Hα surges on the Sun. *Nature*, 375:42–44, May 1995. doi: 10.1038/375042a0.

C. Zwaan. The emergence of magnetic flux. *Solar Phys.*, 100:397–414, October 1985. doi: 10.1007/BF00158438.

C. Zwaan. The evolution of sunspots. In J. H. Thomas and N. O. Weiss, editors, *NATO ASIC Proc. 375: Sunspots. Theory and Observations*, pages 75–100, 1992.

"We all change when you think about it. We're all different all through our lives. And that's okay, that's good. You've got to keeping moving. As long as you remember all the people that you used to be. I will not forget one line of this, not one day. I swear." - The Doctor, Time of the Doctor, 2013